

# Carnegie Mellon University

## CARNEGIE INSTITUTE OF TECHNOLOGY

### THESIS

SUBMITTED IN PARTIAL FULFILLMENT OF THE REQUIREMENTS

FOR THE DEGREE OF Doctor of Philosophy

TITLE Templated Growth of Magnetic Recording Media

---

PRESENTED BY Vignesh Sundar

ACCEPTED BY THE DEPARTMENT OF

Materials Science and Engineering

David E. Laughlin 05/04/15  
ADVISOR, MAJOR PROFESSOR DATE

Jimmy Zhu 05/04/15  
ADVISOR, MAJOR PROFESSOR DATE

Gregory S. Rohrer 05/12/15  
DEPARTMENT HEAD DATE

APPROVED BY THE COLLEGE COUNCIL

Vijayakumar Bhagavatula 06/05/15  
DEAN DATE

# **Templated Growth of Magnetic Recording Media**

Submitted in partial fulfillment of the requirements for

the degree of

Doctor of Philosophy

in

Materials Science and Engineering

Vignesh Sundar

B.Tech., Materials Science and Technology, Indian Institute of Technology (BHU)

M.Tech., Materials Science and Technology, Indian Institute of Technology (BHU)

M.S., Materials Science and Engineering, Carnegie Mellon University

Carnegie Mellon University  
Pittsburgh, PA

April, 2015



# Acknowledgments

**This research was sponsored by Hitachi Global Storage Technologies and Seagate Technology through the Data Storage Systems Center (DSSC) at Carnegie Mellon University. I wish at the outset to thank the sponsors for the financial support.**

The five years I have spent in Pittsburgh have been so much fun, largely thanks to the amazing friends and colleagues I have had the pleasure of meeting here. Professionally and personally, this has been quite an enriching experience. My advisors, Prof. Jian-Gang Zhu and Prof. David Laughlin have been such a source of inspiration throughout; I thank them for giving me the opportunity to learn from them and hope that I can do them proud in the days to come. For the training, the late-night TEM sessions and all her wisdom, I am grateful to Prof. Jingxi Zhu, who is definitely one of the nicest people I have ever met. Likewise, I am also thankful to Dr. Matthew Moneck who got me started with research, and has been a source of support all through the last five years.

I take this opportunity to thank my committee members: Dr. Bruce Terris, whose insightful suggestions during the various DSSC reviews were very helpful in prodding us in the right direction, Prof. Michael Bockstaller, for his valuable comments and questions right from my RPE, and Prof. Vincent Sokalski, who amazingly has gone from being a fellow PhD student to a thesis committee member in these last five years!

I wish to thank a few other students I have had the pleasure of collaborating with: Zhengkun Dai, who is so good at instrumentation, Bing Zhou and Yang Liu, the two masters students who are amazing with their hard work and enthusiasm. These guys have been an absolute pleasure to work with and I wish them the best of luck with their PhDs and beyond.

I would like to thank all the staff members here at CMU: Chris Bowman, Carsen Kline, James Rosvanis, Norman Gottron for their assistance in the cleanroom and all the target changes, Tom Nuhfer, Jason Wolf, Andrew Gamble and Adam Wise, for their training and technical expertise in the various characterization facilities. Their work behind the scenes is so important for the success of any research project here.

Thanks also to my awesome friends: AB, Saketh, Vishnu, Tumul, Priyanka, Steph, Andre, Karina, Erica, June, David Gildemeister, Mina, Sudarshan, David Bromberg, En Yang, Li Hai, Xiaoyu, Hoan, Isen Ozalp, Ankita, Vara, Arvind, Charan and Dhishan for all the amazing memories in the last four years.

I also wish to thank my parents, Sundar and Meenakshi, for so much love and support all through my life, my little sister Rajashree whom I miss so much, my grandparents for all the wonderful childhood memories, and finally my wife, Madhumitha. I first met her in kindergarten and am so glad that she agreed to marry me when I asked her 24 years later. She left her blooming career back in India to come here so that we can share our lives together and I hope that these last two years year since our wedding has been the happiest time of her life too.

# Abstract

Current and potential next-generation magnetic recording technologies are based on the writing and reading of bits on a magnetic thin film with a granular microstructure, with grains of the magnetic material surrounded by an amorphous segregant. In order to realize the highest achievable data storage capabilities, there is a need for better control of the magnetic media microstructure, particularly in terms of minimizing grain size and grain boundary thickness distributions.

In this work, a guided magnetic media growth is attempted by creating a pre-fabricated template with a specific material and morphology. The template is designed in such a way that, when magnetic media consisting of the magnetic alloy and segregant are sputtered, the sites on the template result in a controlled two-phase growth of magnetic media.

The template is fabricated using self-assembling block copolymers, which can be used to fabricate nanostructures with a regular hexagonal lattice of spheres of one block in the other's matrix. These are then used as etch-masks to fabricate the template. In this thesis, we describe the approach used to fabricate these templates and demonstrate the two-phase growth of magnetic recording media. In such an approach, the magnetic grain size is defined by the uniform pitch of the block copolymer pattern, resulting in a uniform microstructure with much better grain size distribution than can be obtained with conventional un-templated media growth.

The templated growth technique is also a suitable additive technique for the fabrication of Bit Patterned Media, another potential next-generation technology wherein the magnetic bits are isolated patterned islands. Combining nanoimprint lithography with templated growth, we can generate a long range spatially ordered array of magnetic islands with no etching of the magnetic material.

# Table of Contents

<b>Acknowledgments .....</b>	<b>iii</b>
<b>Abstract.....</b>	<b>v</b>
<b>Table of Contents .....</b>	<b>vii</b>
<b>List of Figures and Illustrations .....</b>	<b>x</b>
<b>List of Tables.....</b>	<b>xvi</b>
<b>CHAPTER 1 Introduction and Background .....</b>	<b>1</b>
1.1. Concept of Current Magnetic Recording Technology .....	2
1.2. Signal and Noise in Magnetic Recording .....	3
1.3. Materials and Microstructural Considerations in Current PMR .....	4
a. Intrinsic Material Aspects .....	4
b. Microstructural Aspects .....	6
1.4. Media Trilemma.....	11
1.5. Heat-Assisted Magnetic Recording (HAMR).....	11
1.6. Bit Patterned Media (BPM) .....	13
1.7. Problem Statement .....	17
1.8. Thesis Outline .....	17
<b>CHAPTER 2 Hypothesis and Approach .....</b>	<b>19</b>
2.1. Hypothesis.....	19
2.2. Approach.....	19
<b>CHAPTER 3 Characterization Techniques .....</b>	<b>24</b>
3.1. Scanning Electron Microscopy (SEM) .....	24
3.2. Transmission Electron Microscopy (TEM) .....	26
3.3. X-Ray Diffraction (XRD).....	27

3.4.	Alternating Gradient Field Magnetometer (AGM).....	30
3.5.	Magneto-Optic Kerr Effect (MOKE).....	31
<b>CHAPTER 4</b>	<b>Background on Block Copolymers.....</b>	<b>35</b>
4.1.	Introduction.....	35
4.2.	BCP Thermodynamics: Flory-Huggins Theory.....	36
4.3.	BCP Morphologies.....	38
4.4.	BCP Thin Films .....	41
4.5.	Choice of Block Copolymer .....	41
4.6.	Manipulating Feature Sizes in BCP Patterns .....	42
4.7.	Summary .....	45
<b>CHAPTER 5</b>	<b>Nanofabrication Techniques.....</b>	<b>46</b>
5.1.	Introduction.....	46
5.2.	Sputtering the Template Layer and Film Stack .....	46
5.3.	Spin Coating of BCP Film .....	49
5.4.	Annealing of BCP Film .....	50
5.5.	Reactive Ion Etching (RIE).....	59
5.6.	Ion-Milling.....	62
5.7.	Summary .....	66
<b>CHAPTER 6</b>	<b>Template Layer Development for PMR Media.....</b>	<b>67</b>
6.1.	Introduction.....	67
6.2.	Remarks on the CoPt-SiO <sub>2</sub> Sputtering Process.....	67
6.3.	CoCrPt Thin Film as Template Layer.....	68
	a. Setting up the Film Stack.....	68
	b. Block Copolymer Fabrication and Pattern Transfer .....	72
	c. Media Deposition Results and Discussion.....	74
6.4.	Ru Thin Film as Template Layer .....	76
	a. Template Fabrication Details.....	76
	b. Media Deposition Results and Discussion.....	76

6.5. Pt Thin Film as Template Layer .....	80
a. Advantage of using Pt.....	80
b. Sheet-Film Test of Modified Approach.....	81
c. Modified Process Flow .....	83
d. Media Deposition Results and Discussion.....	86
6.6. Conclusions.....	96
<b>CHAPTER 7 Bit Patterned Media using Templated Growth.....</b>	<b>98</b>
7.1. Introduction.....	98
7.2. Experimental Details.....	98
7.3. Results and Discussion .....	100
7.4. Conclusions.....	112
<b>CHAPTER 8 HAMR Media using Templated Growth .....</b>	<b>114</b>
8.1. Introduction.....	114
8.2. Results and Discussion .....	114
8.3. Conclusions.....	123
<b>CHAPTER 9 Alternate Ideas for Templated Growth .....</b>	<b>124</b>
9.1. Introduction.....	124
9.2. Patterning Trenches into a ‘Segregant’ Film .....	124
9.3. High Aspect Ratio Posts as Templates .....	133
9.4. Conclusions.....	144
<b>CHAPTER 10 Conclusions and Suggestions for Future Work.....</b>	<b>145</b>
10.1. Summary .....	145
10.2. Suggestions for Future Work .....	148
a. Perpendicular Magnetic Recording Media .....	148
b. Bit Patterned Media .....	149
c. Heat Assisted Magnetic Recording Media (HAMR).....	150
d. Exploring Different Material Combinations and Nanostructures .....	150
<b>References.....</b>	<b>152</b>

## List of Figures and Illustrations

Figure 1-1: Evolution of areal density over the last 50 years[3].....	2
Figure 1-2: (a) Schematic of tracks and bits in PMR media[7] (b) TEM micrograph of PMR media with schematic of bits .....	3
Figure 1-3: Crystal structure of CoCrPt alloys .....	5
Figure 1-4: Exchange coupling energy density vs segregant layer thickness for different oxide segregants[16] .....	8
Figure 1-5: TEM micrographs of commercial PMR media from 2008 and 2010 (Courtesy: Prof. Jimmy Zhu).....	8
Figure 1-6: (a) Plot showing dependence of data stability on anisotropy energy (b) Energy barrier for switching vs grain size .....	10
Figure 1-7: Schematic of coercivity and temperature for HAMR recording[4] .....	12
Figure 1-8: L1 <sub>0</sub> crystal structure of FePt.....	13
Figure 1-9: Schematic illustrating typical process-flows for additive and subtractive approaches for bit patterned media fabrication.....	15
Figure 2-1: Bright-Field cross-section TEM image of commercial PMR media (Courtesy: Dr. Soyoung Park).....	20
Figure 2-2: Process-flow for templated growth .....	22
Figure 2-3: SEM image of the BCP pattern and histogram showing pitch distribution .....	23
Figure 3-1: Schematic and examples of TEM sample preparation using FIB liftout .....	25
Figure 3-2: (a) Schematic of the XRD experiment (b) Depiction of X-Ray beam with respect to lattice planes of the sample .....	28
Figure 3-3: Schematic of an Alternating Gradient Field Magnetometer .....	30

Figure 3-4: (a) Schematic of the MOKE setup (b) Picture of the MOKE setup.....	32
Figure 3-5: (a) Calibration curve showing current applied to magnet vs magnetic field generated (b) comparing magnetic hysteresis loops measured from MOKE and AGM for a perpendicular magnetic thin film .....	34
Figure 4-1: Molecular formulae of commonly used BCPs PS-PDMS and PS-PMMA .....	36
Figure 4-2: Schematic of the ordering in BCPs[70] .....	38
Figure 4-3: BCP morphologies (a) structural diagram[71], [72] (b) for thin films[43].....	40
Figure 4-4: SEM micrographs of PS-b-PDMS BCP with different molecular weights .....	44
Figure 5-1: Schematic of the sputtering process .....	48
Figure 5-2: Plane-view SEM micrographs illustrating the effect of temperature on the micro-phase separation of (a) PSD1 (b) PSD2 and (c) PSD3 .....	52
Figure 5-3: Effect of thickness of BCP film in the solvent annealing process: (a) cross-section schematic of thickness evolution with annealing[78] (b) plane-view SEM micrographs[78] (c) zoomed-in image showing regions with one and two layers of PDMS spheres.....	53
Figure 5-4: Schematic of (a) simple solvent annealing setup (b) interaction of solvent with the polymer chains .....	54
Figure 5-5: Plane-view SEM micrograph showing PSD1 film solvent annealed using toluene; inset with higher magnification .....	55
Figure 5-6: Plane-view SEM micrographs showing effect of volume of toluene vapor in the solvent annealing of PSD1 .....	57
Figure 5-7: Plane-view SEM micrographs illustrating the effect of volume of toluene vapor in the solvent annealing of PSD3.....	58
Figure 5-8: Schematic of the Reactive Ion Etching system .....	60
Figure 5-9: SEM micrographs comparing erosion of PDMS spheres due to high bias O <sub>2</sub> plasma in RIE .....	61
Figure 5-10: Schematic of the ion-milling system.....	63
Figure 5-11: Secondary Ion Mass Spectroscopy of film stack .....	65

Figure 6-1: Out-of-plane XRD patterns showing the effect of sputtering power for Ru on its crystallographic texture.....	69
Figure 6-2: (a) Out-of-plane XRD patterns showing the effect of Ta sputtering power on the crystallographic texture of subsequently deposited Ru layer (b) Improvement in the FWHM of the rocking curve for Ru (00.2) peak with higher Ta sputtering power....	70
Figure 6-3: Out-of-plane magnetic hysteresis loop for a 5nm CoCrPt thin film .....	71
Figure 6-4: SEM micrographs and out-of-plane magnetic hysteresis loops for CoCrPt milled for 0-30 seconds.....	73
Figure 6-5: Cross-section bright-field TEM micrographs showing the evolution of dome-morphology in CoCrPt on ion-milling for 0-30 seconds .....	74
Figure 6-6: Out-of-plane and in-plane magnetic hysteresis loops from the various attempts at templated media growth using CoCrPt template layer .....	75
Figure 6-7: Out-of-plane and in-plane magnetic hysteresis loops for templated CoPt-SiO <sub>2</sub> media on Ru templates milled for 0-40 seconds.....	77
Figure 6-8: Summary of sputter-etching attempts .....	78
Figure 6-9: Plane-view SEM micrographs showing effect of sputter-etching .....	79
Figure 6-10: Out-of-plane magnetic hysteresis loops for untemplated magnetic media deposited on Ru underlayer exposed to atmosphere (red), not exposed to atmosphere (blue)...	82
Figure 6-11: Modified process flow for template fabrication using Pt.....	83
Figure 6-12: Schematic of the lattice mismatch in the close-packed plane of FCC Pt (111) and HCP Ru (0002) .....	84
Figure 6-13: Out-of-Plane XRD pattern of a Pt thin film deposited on Ta showing FCC (111) texture .....	85
Figure 6-14: (a) Out-of-plane AGM loops (inset showing zoomed in area of interest) and (b) in-plane AGM loops for CoPt-SiO <sub>2</sub> sheet films with varying Ru underlayer thickness.	86
Figure 6-15: (a)Out-of-plane and (b) In-plane magnetic hysteresis loops for templated media using Pt template layer with different milling times .....	87
Figure 6-16: (a)Out-of-plane and (b) In-plane magnetic hysteresis loops for templated media using Pt template layer with different milling times .....	88

Figure 6-17: (a) Out-of-plane M-H loops illustrating effect of ion-milling angle of Pt layer on templated media (b) Coercivity vs ion-milling angle .....	89
Figure 6-18: Out-of-plane and in-plane magnetic hysteresis loops illustrating the effect of Pt (111) rocking angle on templated media properties .....	90
Figure 6-19: Out-of-plane XRD patterns for templated media before and after media deposition, and rocking curves for the Pt (111), Ru (00.2) and CoPt (00.2) peaks.....	91
Figure 6-20: (a)Plane-view TEM micrograph of templated CoPt-SiO <sub>2</sub> media, (b) Grain size distribution and (c) TEM micrograph of ‘untemplated’ CoPt-SiO <sub>2</sub> media.....	92
Figure 6-21: TEM diffraction pattern for the templated CoPt-SiO <sub>2</sub> media. Gray value plot shown is for a vertical line drawn through the center of the diffraction pattern .....	93
Figure 6-22: (a) Cross-section HAADF STEM micrograph of templated CoPt-SiO <sub>2</sub> media (b) High resolution EDS of one of the templated media grains .....	95
Figure 7-1: (a) SEM images of the patterned disk, labeling patterns with different pitch (b) Magnified images of 1 Tdpsi region (27 nm pitch) .....	100
Figure 7-2: (a) Summary of varied and constant processing parameters (b) Coercivity vs ion-milling time for various samples (c) M <sub>r</sub> /M <sub>s</sub> vs ion-milling time for various samples (d) Effect of ion-milling time on the magnetic properties of templated media (e) Effect of Ru underlayer thickness on the magnetic properties of templated media .....	102
Figure 7-3: (a) Bright-field cross-section TEM micrograph of chosen sample (b) Magnified high-resolution cross-section TEM micrograph of Ru grown on one dome (c) High-Angle Annular Dark Field (HAADF) cross-section image .....	105
Figure 7-4: Schematic illustrating the am-C mask structure .....	107
Figure 7-5: Effect of pre-etching for (a) 30 sec (b) 60 sec on the magnetic properties of subsequently grown templated media.....	108
Figure 7-6: Comparing out-of-plane (a) XRD patterns and (b) M-H loops of templated and untemplated regions in the same sample .....	110
Figure 7-7: Plane-view TEM (a) Bright-field micrograph (b) Indexed diffraction pattern of templated BPM media S2 with H <sub>c</sub> = 5000 Oe .....	111
Figure 7-8: Plane-view bright field TEM micrograph for Region B from the templated BPM media S2 .....	112

Figure 8-1: Crystal structures of (a) MgO (b) FePt (c) W (d) Pt .....	115
Figure 8-2: (a) Out-of-plane and (b) in-plane x-ray diffraction patterns for 30 nm W film on MgO .....	116
Figure 8-3: (a) Out-of-plane and (b) in-plane x-ray diffraction patterns for 30 nm Pt film on MgO .....	118
Figure 8-4: Process flow and example SEM images showing the various stages of patterning for W and effect of heating with/without MgO cap layer .....	120
Figure 8-5: Effect of annealing on the dome-morphology patterned into Pt with and without the MgO cap layer.....	121
Figure 8-6: Bright field TEM micrographs of (a) templated FePt-SiO <sub>2</sub> media and (b) un-templated FePt-SiO <sub>2</sub> media.....	122
Figure 9-1: Schematic of alternate templated growth approach – I.....	125
Figure 9-2: SEM micrographs (a) tilt-view image of am-C pillars after pattern transfer (b) after spin-coating HSQ (planarization) (c) etch-back to expose the tops of the am-C pillars and (d) after removal of am-C pillars in RIE.....	127
Figure 9-3: (a) Out-of-plane XRD pattern for underlayer stack (red) and templated media (blue); (b) Rocking curve for the Ru (00.2) peak and (c) Rocking curve for the NiW (111) peak .....	128
Figure 9-4: Figure depicting the lattice mismatch in the close-packed planes of NiW FCC (111) and Ru HCP (00.2).....	129
Figure 9-5: (a) Out-of-plane and (b) In-plane magnetic hysteresis loops of templated (blue) and untemplated (red) media samples .....	131
Figure 9-6: TEM micrographs of templated media using the initial approach.....	132
Figure 9-7: Plane-view SEM micrographs of am-C pillars patterned using HSQ, and after pattern reversal using HSQ process .....	133
Figure 9-8: Schematic for alternate templated growth approach – II .....	134
Figure 9-9: Plane-view SEM images of C pillars and after ion milling into CoCrPt .....	135
Figure 9-10: (a) M-H loop comparing a 15 nm CoCrPt film before (red) and after (black) patterning (b) Coercivity vs milling time for 10 and 15 nm CoCrPt films .....	136
Figure 9-11: SEM and AGM results after patterning into a 10 nm CoCrPt film using PSD2....	138

Figure 9-12: Effect of ion-milling angle on the coercivity of the patterned film .....	139
Figure 9-13: (a) Bright field cross-section TEM after ion-milling into 10nm of CoCrPt using PSD2 (b) High-resolution TEM image (c) HAADF image of the patterned pillars .....	140
Figure 9-14: SEM images and M-H loops after media deposition on 10 nm tall CoCrPt posts patterned using PSD2.....	142
Figure 9-15: Cross-section TEM showing the morphology after pattern transfer into 5 nm of CoCrPt using PSD3.....	143
Figure 10-1: SEM micrograph showing self-assembled block copolymer pattern with 12 nm pitch .....	149
Figure 10-2: Examples of different nanostructures to be explored using templated growth.....	151

## List of Tables

Table 4-1: Molecular weights and minority volume fractions of PS-b-PDMS .....	43
Table 5-1: Summary of spin-coating conditions.....	50
Table 5-2: Table of RIE etch parameters.....	62
Table 5-3: Sputtering conditions in machine #4.....	64
Table 5-4: Milling rates of selected materials.....	65
Table 6-1: Optimized sputter conditions for Ta/Ru/CoCrPt/C film stack .....	71
Table 6-2: Gibbs free energy of oxidation reactions at room temp. ....	81
Table 7-1: Summary of processing parameters for pre-etching and sputtering.....	107
Table 8-1: Summary of sputtering parameters for FePt-SiO <sub>2</sub> deposition.....	122
Table 9-1: Summary of sputtering conditions for various thin films.....	126

# CHAPTER 1

## **Introduction and Background**

2.5 million terabytes (TB) of data are created in the world everyday[1], and the trend is growing at an exponential rate, so much so that approximately 90% of the digital data in the world today was created in the last two years. A large portion of this data is stored on magnetic hard disk drives. In 2012 alone, 569 million hard disk drives were shipped by the industry, with an average data storage capacity of 702 gigabytes (GB) per disk[2]. In order to keep up with such demand, hard disks have continually improved, and the areal density of a hard disk has grown an astonishing 8 orders of magnitude over the last 50 years as seen from Figure 1-1[3]. While the areal density using the current magnetic recording technology can be extended to approximately 1 terabit per square inch (Tbpsi), extensive research and development is underway on potential next-generation technologies such as Heat Assisted Magnetic Recording (HAMR)[4], Microwave Assisted Magnetic Recording[5] and Bit Patterned Media (BPM)[6] to take areal densities much beyond that achievable using the current technology.

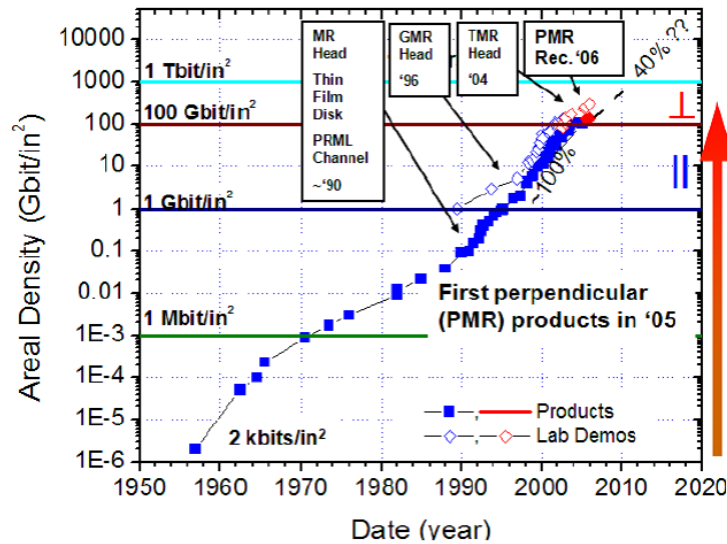


Figure 1-1: Evolution of areal density over the last 50 years[3]

## 1.1. Concept of Current Magnetic Recording Technology

In a hard disk, two states of magnetization of the data storage medium are used to code 0's and 1's or bits. These bits are arranged in circular 'tracks' on a disk as shown in Figure 1-2(a)[7]. A mechanical arm mounted with the read/write heads moves over these tracks to record or read information. In current perpendicular magnetic recording, the media consist of a magnetic CoCrPt-SiO<sub>2</sub> alloy thin film with a granular microstructure, as seen from the plane-view transmission electron micrograph (TEM image) in Figure 1-2(b)[8]. The magnetization of this layer is perpendicular to the plane of the film. Initially, consider that the entire medium is magnetized in one direction. In order to write a '1', a small region of the media, consisting of a group of CoCrPt grains is magnetized in the opposite direction using the write-head, creating a 'transition'. When the read-head passes over this 'transition', it registers a signal, and '1' is read. An absence of such a signal is read as a '0'. The magnetic media film stack currently used in commercial hard disks

may consist of more than one magnetic thin film, with or without grain boundary segregants. These ideas are briefly covered in Section 1.3 (b).

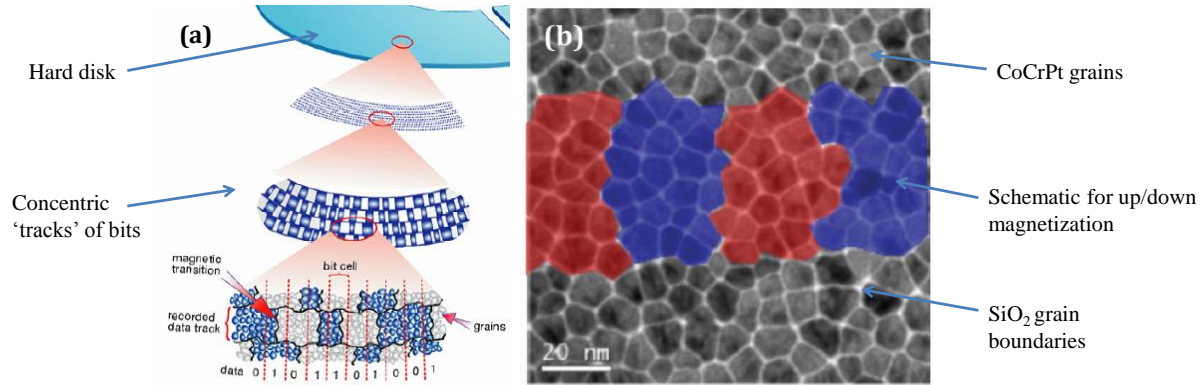


Figure 1-2: (a) Schematic of tracks and bits in PMR media[7] (b) TEM micrograph of PMR media with schematic of bits

## 1.2. Signal and Noise in Magnetic Recording

The magnetic recording system needs to have a certain minimum signal-to-noise ratio (SNR) in order to be used in a hard disk. The different components of the recording system such as the read/write head, the interface electronics and the recording media have different sources of noise which affect system performance. The SNR of the system at a particular recording density (bits per square inch) is thus a suitable indicator for how much data can be recorded in the system at that recording density. The evolution of the magnetic recording media from the longitudinal media technology to the perpendicular media technology that is currently in use today can be viewed as an attempt to improve the media SNR to further extend data storage capacities. Several aspects of PMR technology enabled higher SNR, such as the use of a soft underlayer in the magnetic media stack, the development of a ‘single-pole’ write head, development of the magnetic media with

good perpendicular orientation etc.[9] In this thesis, we focus on the materials engineering of the recording layer, where the bits are stored.

### 1.3. Materials and Microstructural Considerations in Current PMR

#### a. Intrinsic Material Aspects

The first magnetic material proposed for thin film PMR was a Co-Cr alloy, by Iwasaki et al in 1978[10]. Co has high uniaxial magneto-crystalline anisotropy with its magnetic easy axis being along the c-axis of the hexagonal close packed (HCP) crystal structure with the space group  $P6_3/mmc$  (shown in Figure 1-3). Thus a thin film of Co with (00.2) crystallographic fiber texture perpendicular to the plane of the thin film is a suitable magnetic film for PMR. However, since it is a thin film, the demagnetizing field of the material attempts to force the magnetic moment to be in the plane of the thin film. The net anisotropy of the material perpendicular to the plane of the thin film is given by,

$$K_{u,net} = K_{u,intrinsic} - 2\pi M_s^2$$

where  $K_{u,net}$  is the net anisotropy energy per unit volume perpendicular to the plane of the film,  $K_{u,intrinsic}$  is the intrinsic magnetocrystalline anisotropy energy per unit volume of the material and  $M_s$  is the saturation magnetization. Plugging in the values for Co ( $K_{u,intrinsic} = 4.5 \times 10^6$  emu/cc,  $M_s = 1400$  emu/cc) gives a negative value for  $K_{u,net}$  implying that the magnetization will be in the plane of the thin film, which is unsuitable for recording. Thus, the  $M_s$  of the Co is reduced by alloying with Cr in the 5-20 at% range[10]. However, the addition of Cr also reduces the magnetocrystalline anisotropy, thus limiting the amount of Cr that can be added.

Since then, CoCr has been further alloyed with several other elements such as Pt, Ta, B etc. as detailed in the review by Piramanayagam et al. [11]. Addition of up to 25-30% of Pt to Co was found to increase the uniaxial anisotropy[12]. Above this however, addition of Pt resulted in the formation of face-centered cubic CoPt which has no uniaxial anisotropy and is thus not suitable for magnetic recording. The additions of alloying elements such as Cr and Pt to Co has thus been used to tailor the values of anisotropy constant ( $K_u$ ), and the saturation magnetization ( $M_s$ ) to obtain maximum SNR.

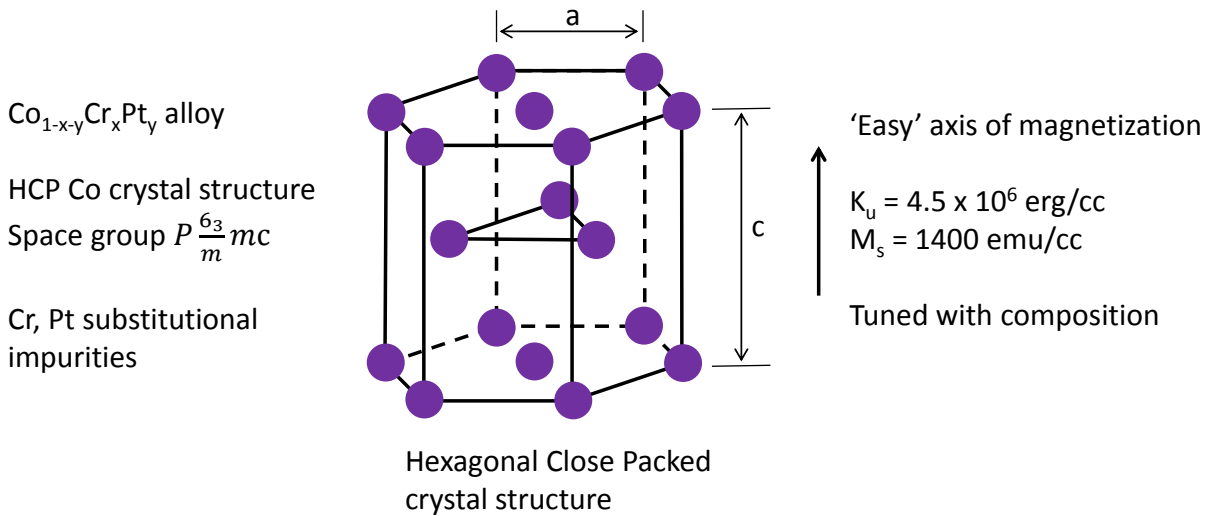


Figure 1-3: Crystal structure of CoCrPt alloys

Apart from the intrinsic material properties described above, crystallographic texture and the media microstructure also plays a critical role in determining the applicability of a thin film as a recording layer.

## b. Microstructural Aspects

The magnetic easy axis for the CoCrPt is along the c-axis or the (00.2) axis of the HCP CoCrPt. Thus the suitable (00.2) texture of the CoCrPt thin film perpendicular to the plane of the film is fabricated by epitaxially growing it on a suitable underlayer such as ruthenium (Ru)[13]. Ru also has the HCP crystal structure like Co, with good lattice matching with Co ( $\sim 7.3\%$  mismatch), which makes it suitable as an underlayer. In order to obtain (00.2) texture with low rocking angle ( $2-3^\circ$ )( $\Delta\theta_{50}$ ) (a measure of c-axis distribution) of the Ru, a thin layer of amorphous Ta, Ni based alloys such as NiW, or other interlayers are deposited first onto the SUL. These research works have been comprehensively reviewed in [11]. Low values of  $\Delta\theta_{50}$  ( $< 3-5^\circ$ ) are critical for high SNR of magnetic media. If there is a high distribution in c-axis (high  $\Delta\theta_{50}$ ), the component of  $\vec{M}$  perpendicular to the film plane is lowered, thus lowering the signal. Also, if the c-axis is not perpendicular to the film-plane, small external fields might be sufficient to flip the direction of  $\vec{M}$ , resulting in an increase in noise.

Magnetic exchange coupling between the grains increases the transition noise. It was earlier found that the Cr added to the magnetic alloy preferentially segregates to the grain boundary at high temperatures, resulting in exchange de-coupling between the magnetic grains[14]. However, high sputtering temperatures were needed to facilitate this, and the addition of excessive Cr to the alloy resulted in a reduction of  $K_u$ , making the media less attractive for recording purposes. It was then found that oxides such as  $\text{SiO}_2$  preferentially segregate to the grain boundaries of the magnetic media even at room temperature. This solved the earlier problem of exchange decoupling the grains while still being able to obtain sufficient  $K_u$  for high SNR. The oxide was either introduced as a reactive gas during the sputtering process[13], or from the target itself[15]. In the first case, the reactive oxygen alloyed with the Cr or other additive elements to form oxides which segregated

to the grain boundary. In the latter case, SiO<sub>2</sub> was added to the CoCrPt target (making a composite target), and it was found to segregate to the magnetic grain boundaries. If the thickness of the grain boundary segregant material is too high, the magnetic volume is lowered, resulting in a reduction in signal from the bit. If instead the grain boundaries are too thin, a distribution in the thickness of the grain boundary segregant results in an increase in noise. Experimental modeling of this effect with different oxide segregants with different thicknesses showed that for grain boundary thicknesses less than 1 nm, there was an exponential increase in the exchange coupling between grains, resulting in poor media performance. One such example is shown in Figure 1-4[16]. In fact, an increase in the grain boundary segregant thickness has helped reduce noise and improve media storage densities in the last few years as evident from the transmission electron micrographs of commercial magnetic media from 2008 and 2010 (Figure 1-5). This increase in storage capacity is attributed to better exchange decoupling between the magnetic grains, resulting in better SNR. Thus, although thinner grain boundaries will mean that there is higher magnetic volume in the bit resulting in a higher signal, the distribution in these thickness values causes an increase in switching field distribution. Minimizing the distribution in grain boundary segregant thicknesses would mean that thinner grain boundaries can be used, increasing SNR.

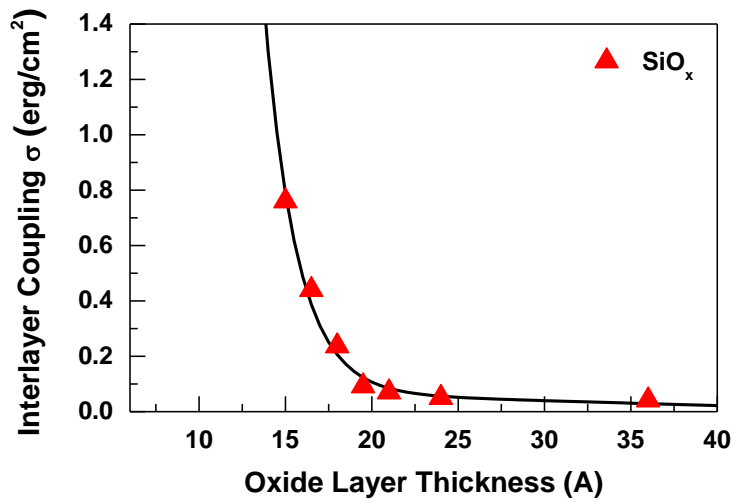


Figure 1-4: Exchange coupling energy density vs segregant layer thickness for different oxide segregants[16]

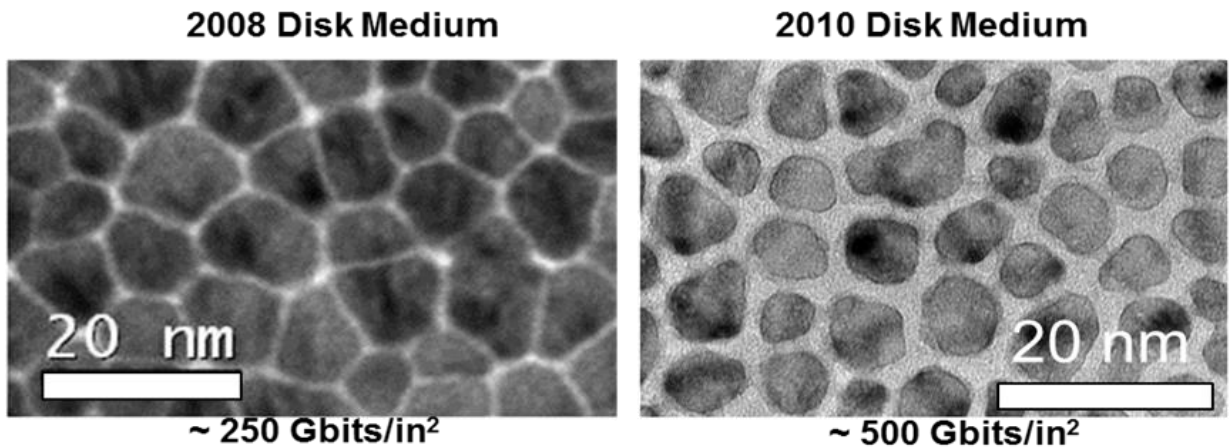


Figure 1-5: TEM micrographs of commercial PMR media from 2008 and 2010 (Courtesy: Prof. Jimmy Zhu)

Recently, more magnetic thin film layers have been added to the media layer. Continuous/Granular Composite (CGC) media consists of a combination of a granular media layer as described above capped by a continuous magnetic thin film without grain boundary

segregant[17], [18], which is found to lower the switching field distribution by modulation of lateral magnetic exchange coupling. In Exchange Spring media, each grain in the granular film has exchange break layers along the vertical direction modulating the vertical magnetic exchange coupling (apart from being exchange decoupled laterally using grain boundary segregants), resulting in better control of switching field and data stability[19], [20].

Another important aspect of the magnetic media microstructure is the grain size. We earlier saw that bits in a magnetic recording medium are made up of a number of magnetic grains (Figure 1-2). The SNR from magnetic media varies with the number of grains in each bit as:  $SNR (dB) \propto \log(N)$ . Now, in order to increase the storage capacity, we have to reduce the size of a magnetic bit, so that more bits can be stored per square inch on a hard disk. In order to keep SNR high enough, we have to keep a similar number of grains in each bit, and so the size of the magnetic grains has to be reduced. However, the grain size influences the stability of the recorded magnetization direction. The stability of recorded data hinges on the comparison between the magnetic anisotropy energy ( $E_b = K_u V$ ) and the thermal energy ( $k_B T$ ). The probability of switching of a magnetic grain per second (in the absence of an external applied magnetic field) is given by:

$$P_{\uparrow \rightarrow \downarrow} = f_0 e^{\frac{-K_u V}{k_B T}}$$

where P is the probability of switching of the magnetization per second,  $f_0$  is an attempt frequency ( $\sim 10^9$  / sec),  $K_u$  is the anisotropy constant of the material, V is the volume,  $k_B$  is Boltzmann's constant, and T is temperature. Based on this formula, the thermal stability of data can thus be simulated, and is shown below in Figure 1-6(a), which plots the time for 25% data decay against the anisotropy energy barrier. In order to ensure the stability of stored data, we have to maintain the energy barrier to the right of the curve, i.e., an energy barrier of approximately 40

$k_B T$ . Assuming ambient temperature of 300 K, an anisotropy constant of  $4 \times 10^6$  erg/cc (typical value for CoCrPt alloys), we can plot the variation of the energy barrier with the grain size (assuming cylindrical grains with a height of 10 nm) as shown in Figure 1-6(b) below. We see that the cut-off in grain size to maintain an energy barrier of  $40 k_B T$  for this particular configuration is approximately 8 nm, which is close to what is currently used in commercial magnetic media. However, if there is a large grain size distribution, it is likely that some of the grains are unstable to thermal agitations, which will result in loss of data. Thus in order to scale PMR media and realize its entire potential in terms of recording density, minimization of grain size distribution is critical.

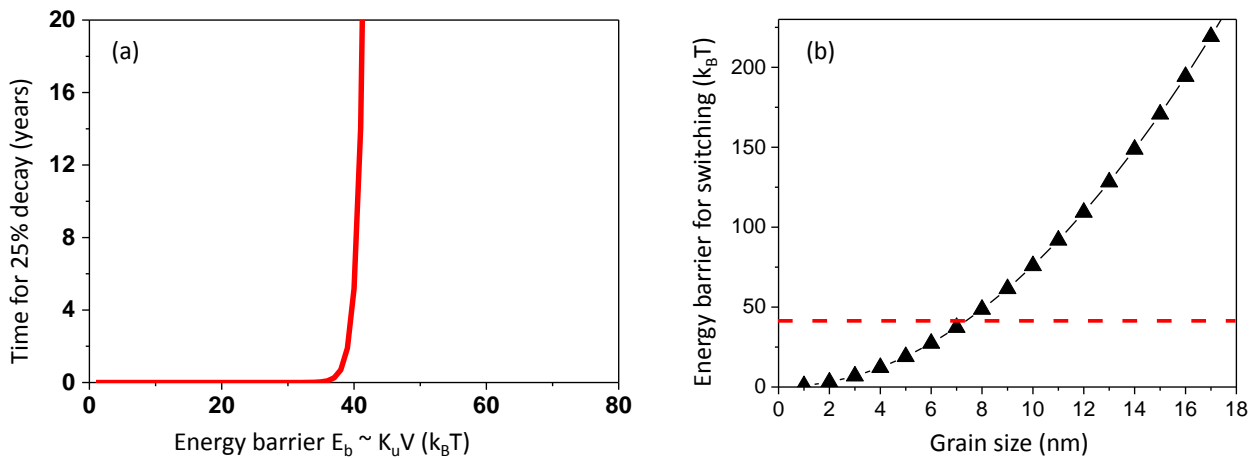


Figure 1-6: (a) Plot showing dependence of data stability on anisotropy energy (b) Energy barrier for switching vs grain size

Minimization of grain size and grain boundary thickness distributions may aid in further extending the data storage capacity close to 1 Tbps. However, extensive research is underway to find suitable magnetic recording technologies for the future, to enable recording densities of more than 1 Tbps. The following sections address the ‘media trilemma’ and two potential next-

generation magnetic recording technologies, Heat Assisted Magnetic Recording [4, 5] and Bit Patterned Media[6].

## 1.4. Media Trilemma

The stability of the written data depends on the energy barrier that prevents thermal energy  $k_B T$  from reversing the magnetization of a grain. As we discussed earlier, this energy barrier is proportional to  $K_u V$  where  $K_u$  is the magneto-crystalline anisotropy constant of the material and  $V$  is the volume of the grain[21]. In order to increase storage density while keeping the signal-to-noise ratio (SNR) acceptable (SNR is proportional to number of grains in a bit as discussed earlier), the grain size and hence  $V$  is reduced. Thus,  $k_B T$  can overcome  $K_u V$  and the magnetization in the grain could switch even though there is no field applied (superparamagnetism), resulting in a loss of data[22]. Choosing materials with high  $K_u$  can solve this problem, but higher applied fields would be required to switch the magnetization as the switching field scales with the anisotropy field  $H_k = \frac{2K_u}{M_s}$ [23], where  $M_s$  is the saturation magnetization of the material. Currently, the magnitude of the field is limited by the maximum flux density the material used in the write head ( $\text{Fe}_{65}\text{Co}_{35}$ ) can generate, to about 1.5 T[24]. Thus we see that SNR, thermal stability, and writability are interrelated and improvement of one may cause problems with the other.

## 1.5. Heat-Assisted Magnetic Recording (HAMR)

In case of HAMR, the problem of requiring high write-fields to record data in high anisotropy materials is circumvented by writing the data at an elevated temperature close to the Curie temperature of the recording medium[4]. A near-field transducer is used for heating the media. In the case of thin film recording media with magnetic grains decoupled by amorphous grain boundaries, the switching field scales with the anisotropy field  $H_k$ . The anisotropy field reduces

with an increase in temperature, and vanishes at the Curie temperature ( $T_c$ ). Thus, the head field required to write data on the media heated close to the Curie temperature is much lower, and within the head field available today, as illustrated in Figure 1-7. Then, as the media cools, the data is maintained in a stable fashion because the material has a high enough anisotropy.

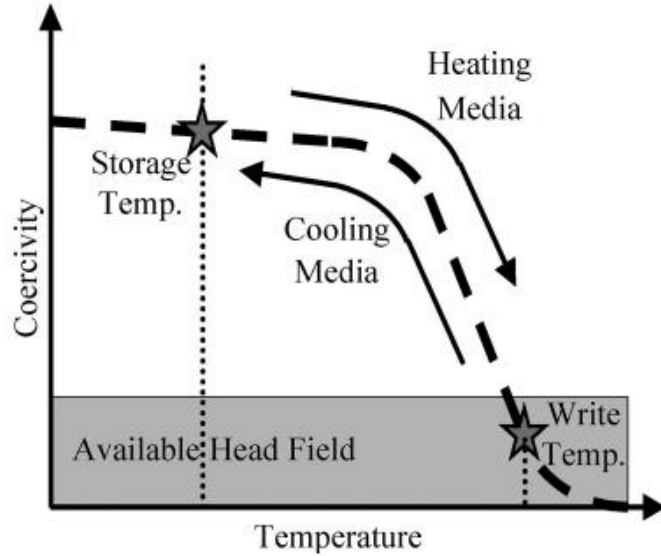


Figure 1-7: Schematic of coercivity and temperature for HAMR recording[4]

The material chosen for this purpose is FePt, which has an  $L1_0$  crystal structure (shown in Figure 1-8) with a space group of  $P4/mmm$ , and a high anisotropy constant of  $7 \times 10^7$  erg/cc[25]. As we discussed earlier, the higher anisotropy of FePt lowers the grain size where the FePt will be superparamagnetic, thus enabling higher grain densities and consequently, higher areal densities. Control of material properties such as magnetocrystalline anisotropy, Curie temperature, and control of the microstructural aspects such as texture, columnar grains exchange decoupled from one another, and minimization of the distributions in all of these has proved quite challenging and has attracted intense research over the past decade or so.

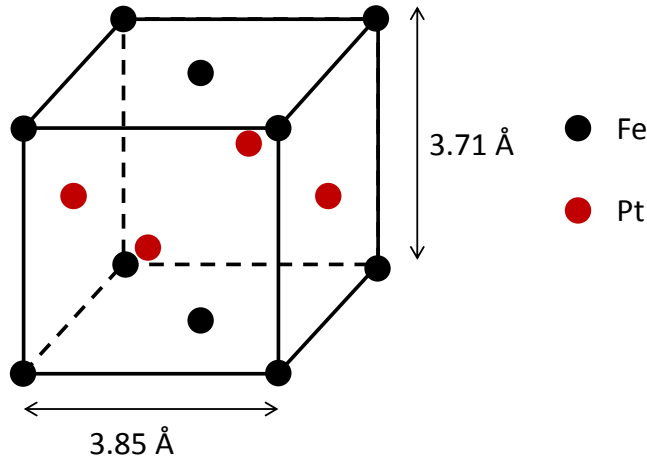


Figure 1-8: L1<sub>0</sub> crystal structure of FePt

## 1.6. Bit Patterned Media (BPM)

Another potential next-generation magnetic recording technology is based on bit-patterned media (BPM). Here, individual magnetic islands are patterned using lithography techniques, and each of these islands act as a bit. The advantage with BPM is that the position and volume of each bit is fixed, and so the statistical fluctuations in the position of the transition, which causes noise, is no longer an issue. However, the fabrication of BPM with high throughput is a big challenge, due to exactly the same reason, that the entire media now has to be patterned. These fabrication challenges are reviewed in [6]. As the author explains in that review, to compete with current perpendicular magnetic media (approximately ~ 700 Gbps), patterned media with center-to-center spacings of 36 nm and below are required, and in order to scale the storage density, patterns with sub-10 nm features will soon be a necessity, which cannot be achieved by high-throughput optical lithography. E-beam lithography can be used, but the throughput in this case is a limiting factor[26]. Alternative fabrication techniques, such as nanoimprint lithography, or a combination

of electron-beam lithography with directed self-assembly (DSA), are being explored for this purpose.

In case of nanoimprint lithography, a master is first patterned using a combination of electron beam lithography and directed self-assembly techniques, and is subsequently used to stamp a curable resist coating on every disk for high-throughput manufacturing[6], [27]–[32]. The resist is first spin coated onto the disk, and the rigid mold, which is usually made of quartz is then pressed onto the resist and UV-cured, leaving behind a negative of the pattern. In case of DSA, self-assembling materials such as block copolymers, nanoparticles and anodized aluminum oxide are used. Anodization of aluminum results in the formation of a periodic close packed arrangement of pores. The size and period can be controlled by current, density, or pH during the anodization process. After a template is created, the pores can be filled with magnetic metals by electrodeposition. Using such a technique, 11 nm pores with periods of 40 nm or more have been reported[33]–[35]. Nanoparticles have been found to self-assemble into two or three-dimensional structures with sub-10 nm features. For instance, monodisperse Co nanoparticles were synthesized in the size range of 3-10 nm by reduction from a salt solution, and solvent-cast to form an ordered 2-D array [36]. Arrays of nanoparticles can be used to create anti-dot or dot patterns which can be used as templates for media growth[37]. The challenges in this approach lie with reducing size dispersion during the synthesis of nanoparticles and preventing their agglomeration, which is particularly problematic for magnetic particles that have strong attractive forces. Orienting the easy axes of these nanoparticles in a specific direction is an additional challenge. Long-range positional ordering of nanoparticles over large areas has also proved quite challenging. Block copolymers are self-assembling materials which can form a wide-range of morphologies as discussed in chapter 4. They self-assemble into nanostructures which can be ‘guided’ using

topographical or chemical variations on the substrate over large areas[38]–[43]. Recently, a combination of lamella-forming block copolymers and a double-imprint strategy was used to demonstrate the fabrication of bit patterned media[44].

The approaches for the fabrication of magnetic islands in BPM can be broadly classified into two types: additive and subtractive. These two ideas are illustrated using a schematic in Figure 1-9.

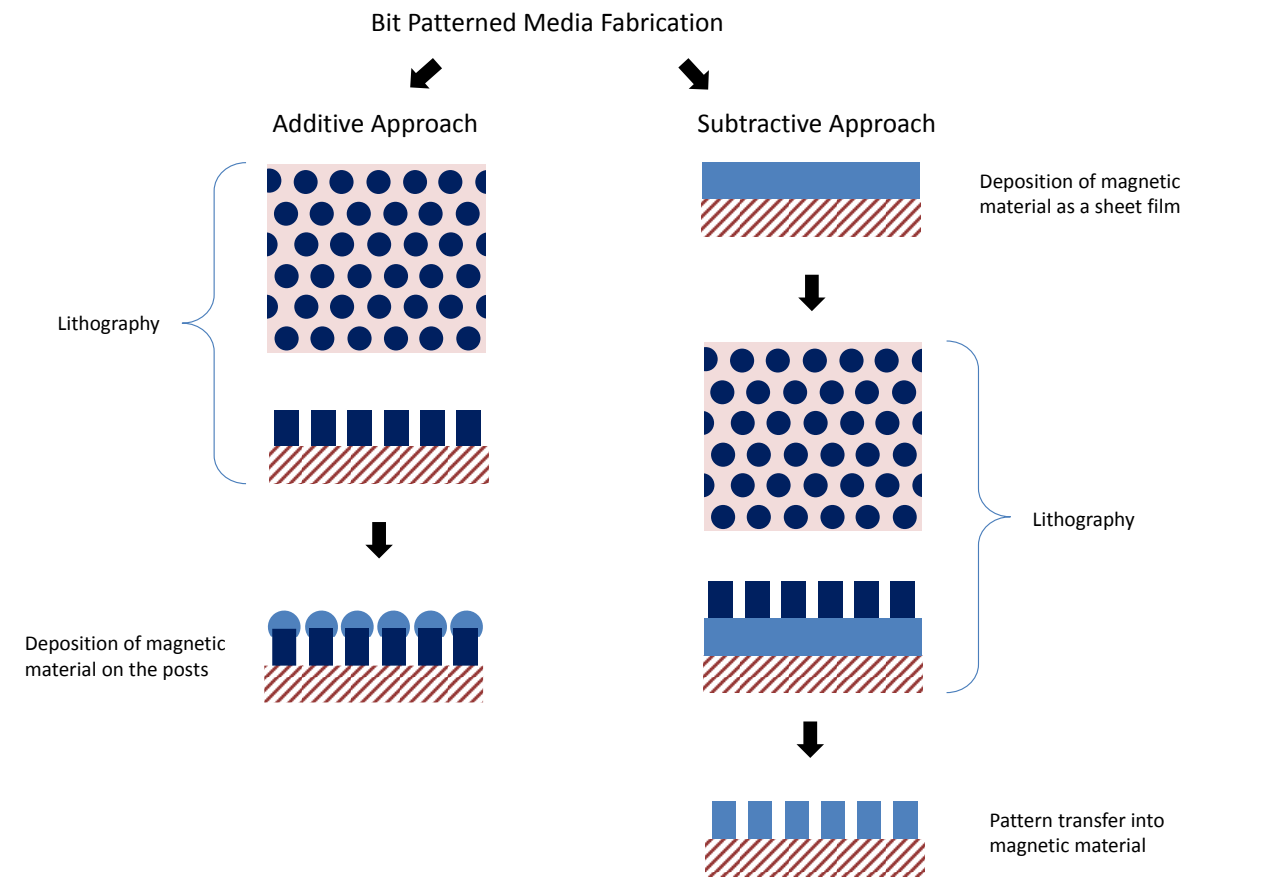


Figure 1-9: Schematic illustrating typical process-flows for additive and subtractive approaches for bit patterned media fabrication

In case of the additive approach, the substrate is patterned first, and the magnetic media is subsequently deposited. The patterning of the substrate is performed as discussed earlier, and the magnetic media is deposited typically by sputtering[45]. The sputtering conditions are optimized such that the deposition of the film is maximized on top of the patterned substrate and trench material is minimized[46]. However, the presence of trench material has been found to result in noise during the recording process. Usually, Co/Pd, Co/Ni and other such multilayers are used in case of the additive approach since their magnetic anisotropy does not require epitaxial growth. In these cases, surface/interface anisotropy fixes the magnetic easy axis perpendicular to the plane of the film[47]–[50].

In the case of the alternative, subtractive approach, the magnetic media is first deposited as a sheet film and then patterned using ion milling or reactive ion etching[51],[52]. Pattern transfer is quite challenging using RIE since etch-chemistries are not readily available for the etching of magnetic metal or alloy films. Pattern-transfer can be accomplished using ion-milling, but there are issues due to damage from the physical bombardment of the ion-beam, as well as redeposition issues when patterning is attempted at high densities[53]. Scaling to sub-20 nm features may be an additional challenge. In the case of ion-milling, patterning of features with aspect ratios  $(h/d) > 0.5$  is difficult, and so, as the center-to-center distance between adjacent bits is reduced (as is required for increasing areal density), the thickness of the film also needs to be reduced, resulting in a lowering of signal. There are no limitations on the kinds of materials which can be used in this approach, except those imposed by pattern transfer considerations.

There has been much progress in BPM fabrication, but the current approaches have both pros and cons, as described earlier. It is therefore of interest to explore other potential techniques for

BPM fabrication, avoiding etching/milling of the magnetic film, while also avoiding trench material in case of the additive approach.

## **1.7. Problem Statement**

There are several engineering challenges in the media fabrication for each of the magnetic recording technologies we discussed in the previous sections. Although current PMR media is close to reaching its recording density limits, control of the grain size and grain boundary thickness distributions may enable an improvement in achievable areal densities. Better control of film microstructure is also critical for the realization of HAMR media. Further, as discussed in Section 1.6, there is a need for alternative scalable approaches for bit patterned media fabrication.

## **1.8. Thesis Outline**

In this chapter, the current and future generation magnetic recording concepts were introduced, with focus on the magnetic media aspects, particularly material and microstructure. We also discussed the current research in these areas, and the challenges that still need to be overcome to further extend data storage capacities. The problem statement was then defined. Chapter 2 provides the hypothesis for our research and discusses a potential approach for attempting to control the magnetic media microstructure. A suitable process flow is outlined. Chapter 3 briefly describes the various structural, magnetic and microstructural characterization techniques used in this project. In chapter 4, we introduce the concepts related to block copolymer micro phase separation, and discuss the choice of block copolymer for our project. Short introductions and process development details are outlined in chapter 5, with particular focus on block copolymer thin film

processing. In chapter 5, we identify suitable template layer materials and compare the magnetic properties for the fabricated templated media. We subsequently discuss the microstructure of templated media with good magnetic properties and low grain size distribution. In chapters 7 and 8, we discuss the potential application of this templated growth technique for the fabrication of bit patterned media (chapter 7) and HAMR media (chapter 8). While all of the previous chapters dealt with the approach outlined in chapter 2, we attempted two other approaches for the fabrication of these templates; these results are discussed in chapter 9. In chapter 10, we revisit the conclusions from this project, and suggest potential directions for continuing the research.

# CHAPTER 2

## Hypothesis and Approach

### 2.1. Hypothesis

We hypothesize that control of magnetic media microstructure can be achieved by creating a pre-fabricated template designed in such a way that, when magnetic media consisting of the magnetic material and the segregant is sputtered onto it, the sites on the template facilitate the controlled growth of the magnetic media.

In the first part of this work, the template is patterned using self-assembling block copolymers, which form a uniform array of spheres of one block in the other block's matrix. The grain size of the media is thus defined by the center-to-center spacing in the block copolymer nanostructure resulting in a control of magnetic film microstructure that is not available just by the current untemplated sputtering process.

### 2.2. Approach

As discussed in chapter 1, current magnetic media consists of multiple magnetic thin films in order to optimize properties such as switching field, squareness of hysteresis loop, and for modulating the inter-granular exchange coupling between the magnetic grains. A certain degree of control over the microstructure of the granular media layer has been achieved using a dual-Ruthenium (Ru) underlayer[54], [55], wherein the bottom-Ru layer is sputter deposited with a low

Argon (Ar) pressure (high mobility condition) and the top-Ru layer is sputter deposited with a high Ar pressure (low mobility condition). In doing so, the top-Ru layer grows with a dome-like morphology[56], [57] which was found to facilitate a media microstructure where CoPt grows on top of the domes and the SiO<sub>2</sub> grew in the trenches between the Ru domes. Figure 2-1 below, which shows a cross-section Transmission Electron Microscopy (TEM) image of magnetic media from a commercial hard disk illustrates this concept. In this bright field image, we can see the Ru dome, along with the CoCrPt grain on top and the bright amorphous SiO<sub>2</sub> in the trenches. However, there is no control over the positions of these Ru domes, which are controlled only by the statistical nucleation and growth over the film surface.

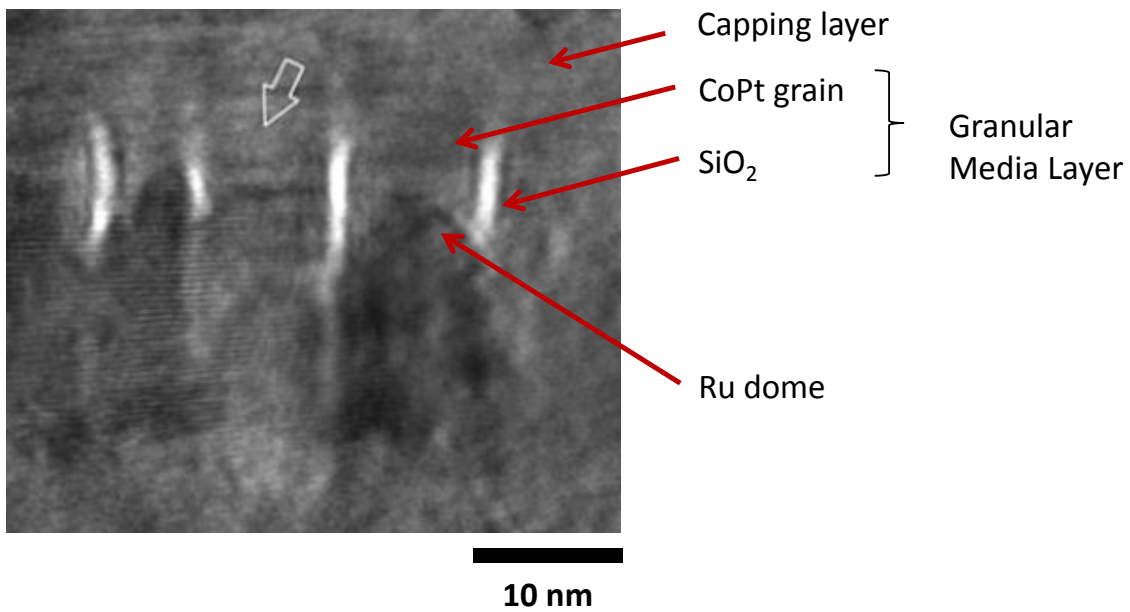


Figure 2-1: Bright-Field cross-section TEM image of commercial PMR media (Courtesy: Dr. Soyoung Park)

For fabricating a suitable template for magnetic media, we utilized the highly regular microstructure formed in the block copolymer thin films to pattern the dome-morphology into a suitable ‘template-layer’ thin film. The process-flow for this approach is shown in Figure 2-2. The initial film stack comprising of an adhesion layer (Tantalum), the template layer (to be discussed) and the hard-mask (amorphous carbon) were first sputtered onto single-crystal silicon substrates (with native oxide) purchased from MTI Corp. The block copolymer (BCP) chosen was poly (styrene-*b*-dimethyl siloxane) (PS-*b*-PDMS, m.wt. = 13.9 kg/mol,  $f_{\text{PDMS}} = 17.2\%$ ). The various sub-steps involved in BCP processing, and pattern transfer into amorphous carbon mask layer are discussed in detail in chapter 5. Using this as the hard mask, the required dome-morphology is then patterned into the template layer (chapter 6). In the ion-mill, the thin film to be milled is maintained such that the ion-beam has a non-zero direction with its plane normal. The thin film is also rotated to ensure uniform milling. This angle and the ion-milling time can be varied to modify the dome-morphology. The ion-milling and RIE times are optimized in such a way that the carbon hard mask is completely depleted upon completion of the ion-milling process. Onto this fabricated template, magnetic media consisting of CoPt-SiO<sub>2</sub> is deposited using the Z400#1 sputtering system using RF sputtering.

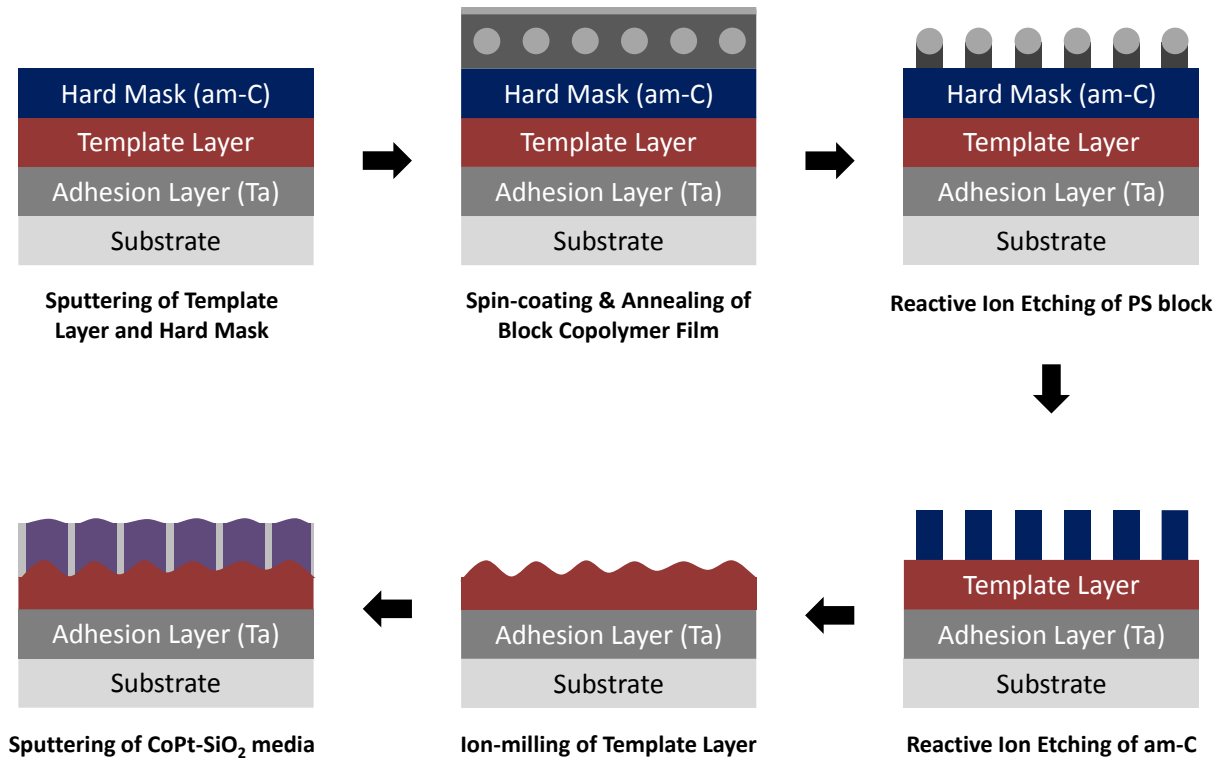


Figure 2-2: Process-flow for templated growth

As per our discussion, the CoPt should grow on top of the domes, with SiO<sub>2</sub> growing in the trenches. If this is the case, the grain size is then determined by the center-to-center distance between the domes in the template. Figure 2-3 shows a SEM image of the BCP pattern after solvent annealing, and a histogram showing the distribution in the ‘pitch’ (center-to-center distance between the spheres). The average pitch is 17.3 nm, with a standard deviation of 9.8%. A template fabricated using such a BCP pattern will result in magnetic media with a much better grain size distribution than what can be achieved just using sputtering[58], which results in grain size distributions of 20-25% .

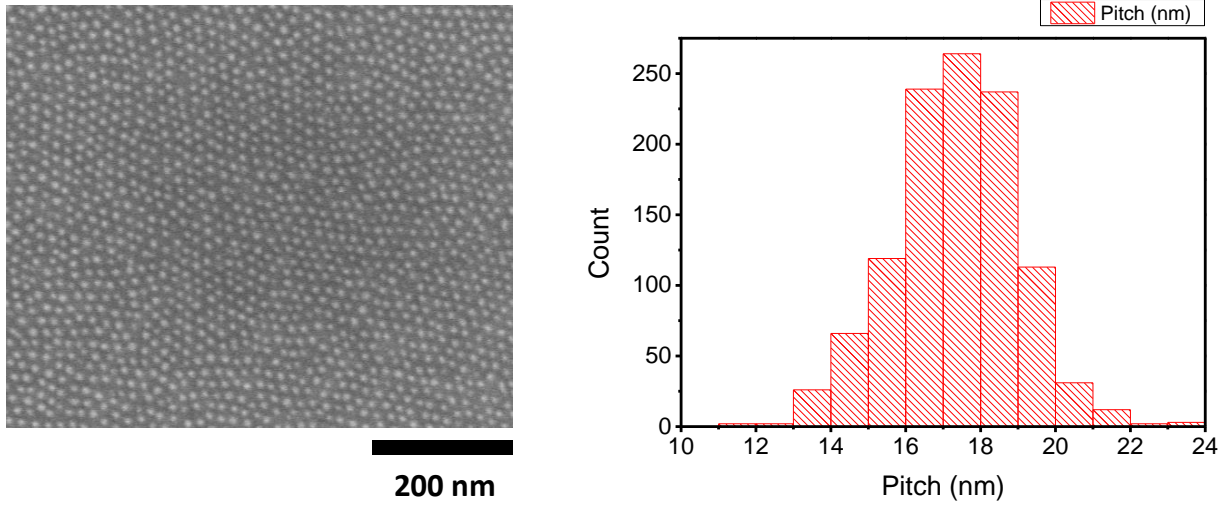


Figure 2-3: SEM image of the BCP pattern and histogram showing pitch distribution

# CHAPTER 3

## Characterization Techniques

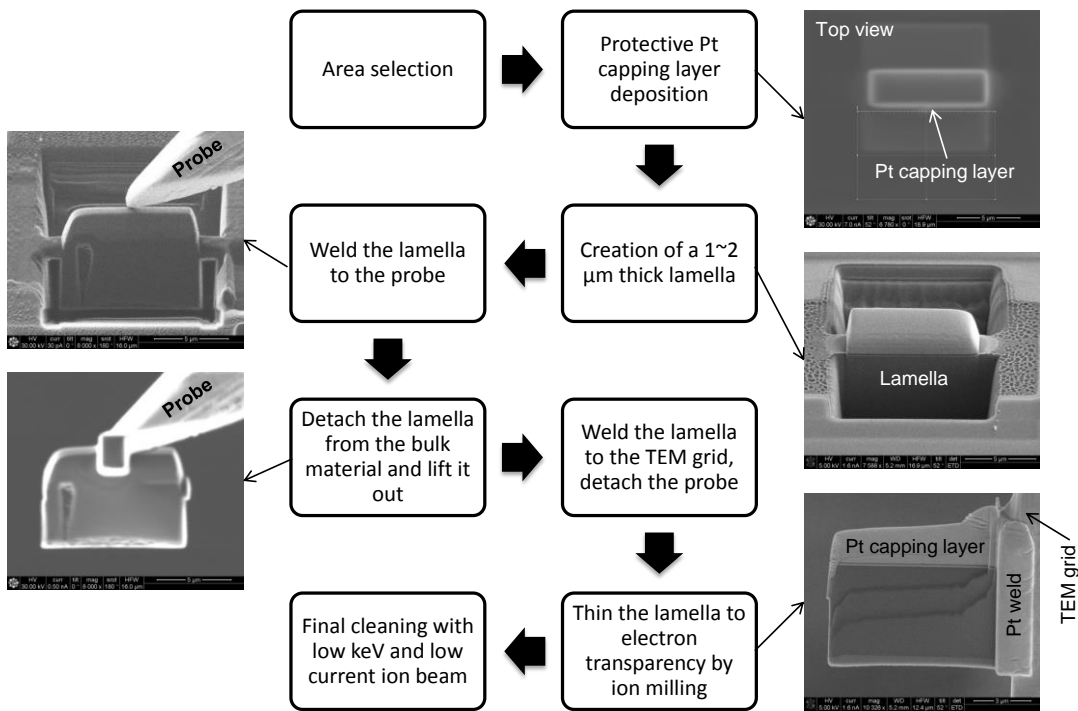
### 3.1. Scanning Electron Microscopy (SEM)

Scanning electron microscopy (SEM) is a characterization technique used for studying the morphology and chemistry of materials. In a vacuum chamber, an electron beam is generated using a filament source or a field emission source and focused onto the sample with a spot size  $< 5\text{nm}$  using a system of magnetic lenses. The incident electron beam interacts with the sample over an ‘interaction volume’, which increases with the acceleration voltage of the electron beam, and decreases with increasing atomic number of the sample. From approximately the first 10% of the depth, secondary electrons are emitted from the sample on its interaction with the incident electron beam. These are collected by an Everhart-Thornley (ET) detector and information is recorded. The electron beam is rastered on the sample using scan coils to study the area of interest. The key contributor to contrast in an SEM is topography, since the trajectories of the emitted secondary electrons strongly depend on the surface morphology and topography of the specimen. Composition/phase contrast can be studied using back-scattered electron imaging modes[59].

In order to study the block copolymer patterns in this thesis, we used a more advanced detector called a Through-the-Lens Detector. This detector is located above the objective lens inside the electron column and a low working distance (distance between the sample and the pole piece) of 4-5 mm is used. This was critical for the imaging of the block copolymer patterns since it has a

much higher resolution compared to the ET detector, thus allowing high-throughput imaging of the block copolymer patterns with minimal sample preparation. The SEM was utilized for monitoring the sample at various stages of the patterning process. Most of the scanning electron micrographs in this thesis were obtained using an FEI Sirion 600 SEM with an acceleration voltage of 10kV, spot size of 3, and a working distance of 4 mm.

We also used a NovaLab 600 Dual Beam FIB (Focused Ion Beam) SEM to prepare cross-section TEM specimens by a lift-out procedure. The various steps involved in this process are outlined below, in Figure 3-1. This TEM sample preparation technique is advantageous since very little material from the wafer is used for TEM sample preparation, unlike the grinding and polishing technique typically used. Additionally, since an SEM is used, we can prepare TEM samples from specific areas after first imaging them to ensure they are an area of interest.



Courtesy: Dr. Jingxi Zhu

Figure 3-1: Schematic and examples of TEM sample preparation using FIB liftout

During FIB-liftout for our samples, ion-beam conditions of 30 kV and 5-7 nA was used for creating the lamella, and the current is reduced periodically for the thinning steps, to around 0.5 nA for the final cleaning step. E-beam conditions of 5 kV, 1.6 nA was used for imaging.

A Quanta 600 FEG SEM fitted with Energy Dispersive X-Ray Spectrometry (EDS) was used to determine the compositions of the CoCrPt-SiO<sub>2</sub> and other alloy targets used in this work. During the interaction of the electron beam with the specimen, x-rays characteristic to the elements in the specimen are produced. The relative magnitude of these is analyzed to obtain the composition of the specimen. The compositions of these targets were determined by sputtering a thick (50-350 nm) film on an alumina or silicon substrate and doing EDS analysis, and are mentioned in the relevant sections.

### **3.2. Transmission Electron Microscopy (TEM)**

A TEM probes the interactions of a monochromatic electron beam with an electron transparent specimen. The transmitted beam contains information about the microstructure, chemistry and crystallography of the specimen. Depending on these characteristics, a fraction of the beam undergoes diffraction, while the rest get transmitted without any scattering. The wavelength of the electron beam depends on the accelerating voltage, which for a 200kV microscope is around 3 pm. Although the resolution of the microscope is ultimately limited by the defects and aberrations in its lenses, atomic resolution can be obtained in several advanced microscopes [60]. For the thin films used in this work, electron transparent samples were prepared by grinding and dimpling followed by thinning using ion-milling in a Gatan Precision Ion Polishing system. We also used FIB liftout to prepare TEM specimen as described in Section 3.1. In this project, we used three

TEMs: the JEOL 2000, 200kV FEI Tecnai F20 TEM, and the FEI Titan G2. TEM was used for the following characterization:

- i. Microstructure: The imaging mode uses both the direct and diffracted beams to provide phase-contrast. This is useful in our case, for instance, to observe the segregated microstructure for a granular film of CoPt-SiO<sub>2</sub>.
- ii. Crystallography: Using the diffraction mode, information about the structure and texture of the thin films can be extracted.
- iii. HAADF and EDS analyses in STEM mode described below.

In addition to conventional TEM, advanced microscopes are also fitted with Scanning Transmission Electron Microscopy (STEM) capabilities. In this mode, the electron beam is focused as a spot and raster scans the sample. The first half of the operation is thus similar to the operation in an SEM, with the key difference that the transmitted electron beam is analyzed in this case. This mode enables analyses such as EDS (composition analysis technique described in Section 3.1), and High Angle Annular Dark Field (HAADF) imaging. In case of HAADF, an annular (ring-shaped) detector is placed at a high angle with respect to the direct beam so that the signal arises primarily from incoherent scattering, which depends on the atomic number 'Z'. Thus in a HAADF image, elements with higher atomic numbers appear brighter[61]. Such a technique can be useful when diffraction contrast is unable to provide us with sufficient information.

### **3.3. X-Ray Diffraction (XRD)**

X-Ray Diffraction is used to study the crystallographic aspects of materials. It is based on the diffraction of x-rays from the atomic planes of a crystal, which is possible since the wavelengths

of x-rays are on the same order of magnitude as the lattice plane spacings. Figure 3-2(a) shows the schematic of a typical thin film XRD experiment. An X-Ray tube generates a beam of x-rays by striking a metal target, such as copper (Cu), with a beam of high energy electrons. This high energy electron beam knocks off inner-shell electrons from Cu atoms, and when outer-shell electrons relax into the inner shell, an x-ray with a wavelength corresponding to the energy difference between the outer and inner shells is produced[62]. For our studies, we used Cu K- $\alpha$  radiation with a wavelength of 1.54 Å, which is produced when an L-shell electron relaxes into the innermost K shell. All other wavelengths are filtered out and a parallel, collimated beam of x-rays is produced. The equipment used was a Panalytical X'pert Pro MPD X-Ray Diffractometer with an acceleration voltage of 45 kV and a current of 40 mA.

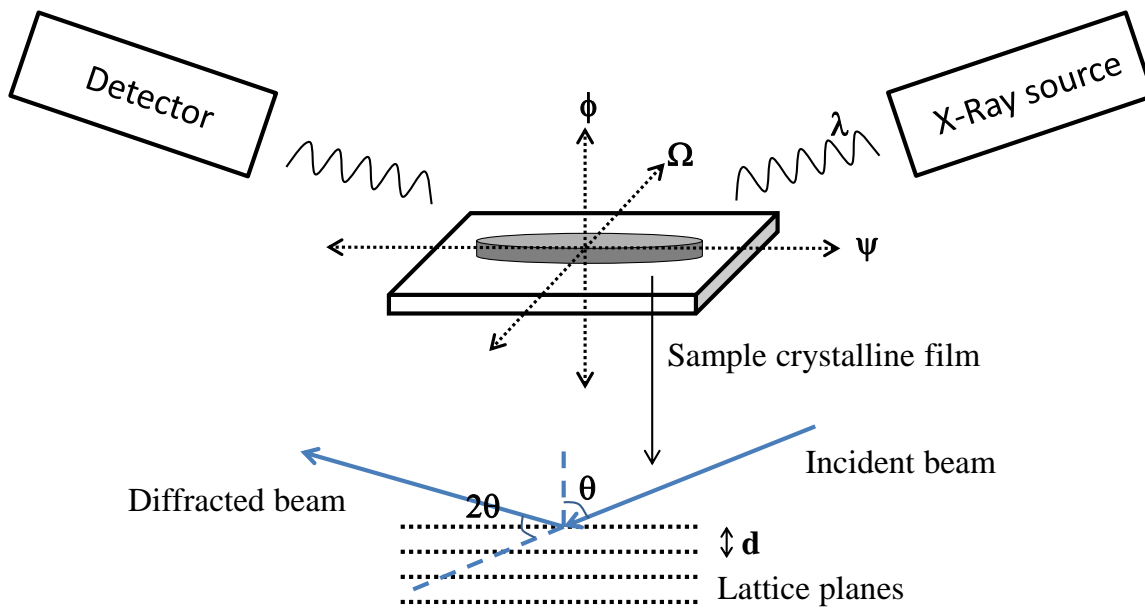


Figure 3-2: (a) Schematic of the XRD experiment (b) Depiction of X-Ray beam with respect to lattice planes of the sample

The Bragg law describes the diffraction condition for x-rays interacting with the specimen:

$$2d_{hkl} \sin \theta = n \cdot \lambda$$

where  $d_{hkl}$  is the lattice plane spacing,  $\theta$  is the angle between the incident beam and the normal to the lattice planes,  $n$  is the order of diffraction, and  $\lambda$  is the wavelength of the x-ray. The intensity of the diffracted beam depends, among other factors, on the square of the structure factor  $F_{hkl}$ , given by:

$$F_{hkl} = \sum_{i=1}^N f_i \exp 2\pi i(hx_i + ky_i + lz_i)$$

Here,  $f_i$  is the atomic scattering factor for the  $i^{\text{th}}$  atom in the unit cell,  $x_i$ ,  $y_i$ ,  $z_i$  are the fractional coordinates of the atoms in the unit cell, and  $h$ ,  $k$ , and  $l$  are the Miller indices of the lattice planes. The intensity of the diffracted beam thus has information about the crystallographic structure of the sample.

For the thin films studied in this thesis, XRD is used to study the crystallographic texture of the films[62]. For this purpose, we typically do three kinds of scans: an out-of-plane scan, an in-plane scan and a rocking curve. In an out-of-plane  $\theta$ - $2\theta$  scan, the diffraction is from the planes with their normals perpendicular to the plane of the thin film. In an in-plane scan, the sample is rotated about the  $\psi$  axis so that the planes with their normals lying in the substrate plane are probed. The rocking curve is an  $\Omega$  scan. The Bragg condition is held fixed for a particular peak on the out-of-plane scan, i.e. a particular set of lattice planes. The  $\Omega$  is then scanned around  $10^\circ$  about the peak value, and the full-width at half maximum (FWHM) in the intensity vs  $\Omega$  curve is a measure of the distribution of the plane normal or the fiber texture of the film.

### 3.4. Alternating Gradient Field Magnetometer (AGM)

An Alternating Gradient Field Magnetometer (AGFM) can be used to study magnetic hysteresis loops and other magnetic properties of a specimen (shown in Figure 3-3). In this technique, the sample is subjected to a large applied field (up to 13 kOe) ( $H_{DC}$ ) and a smaller alternating magnetic field ( $H_{AC}$ ). Now, when a magnetized sample is subjected to an alternating magnetic field, it experiences a force as:

$$\vec{F} = -\vec{\nabla} \cdot E = \vec{\nabla} \cdot (\vec{M} \cdot \vec{H}_{AC}) \sim |M|(\nabla \vec{H}_{AC})$$

If there is thus a magnetic field gradient, the sample experiences a force, and the displacement due to this force is then recorded using a piezoelectric sample holder, which converts a displacement to a voltage signal. Since this force is proportional to the magnetization, a magnetic hysteresis loop can be recorded ( $M$  on varying  $H_{DC}$ )[63]. The measurements on the samples in this thesis were performed using a Princeton Alternating Gradient Field Magnetometer with a maximum field of 13 kOe.

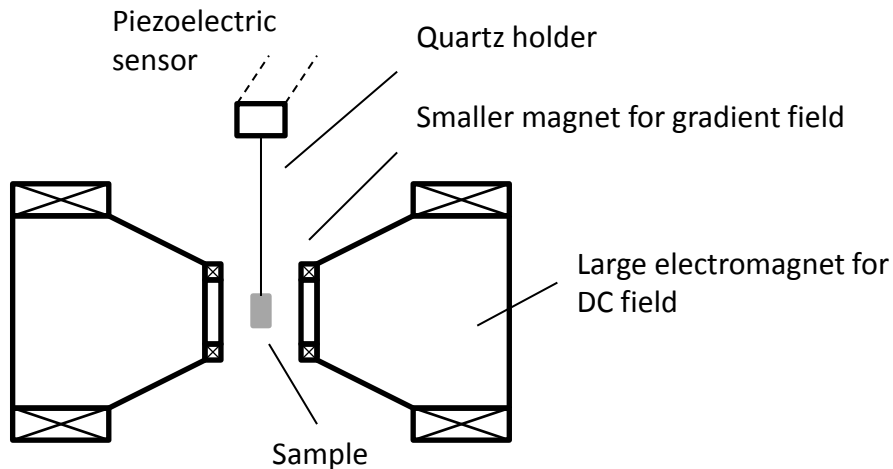


Figure 3-3: Schematic of an Alternating Gradient Field Magnetometer

### **3.5. Magneto-Optic Kerr Effect (MOKE)**

The Magneto-Optic Kerr Effect describes the rotation of the plane of polarization of a polarized light beam upon reflection from a magnetized specimen. The magnitude of rotation depends upon the component of magnetization of the sample parallel to the direction of light propagation[63]. In order to utilize this effect for the measurement of magnetic hysteresis loops, the following ‘polar’ MOKE setup was constructed in-house, in collaboration with Andrew Gamble. Polar MOKE implies that the magnetization of the film is perpendicular to the surface of the thin film and parallel to the plane of incidence of the laser beam. Figure 3-4(a) shows the schematic of the MOKE setup and Figure 3-4(b) shows a picture of the setup.

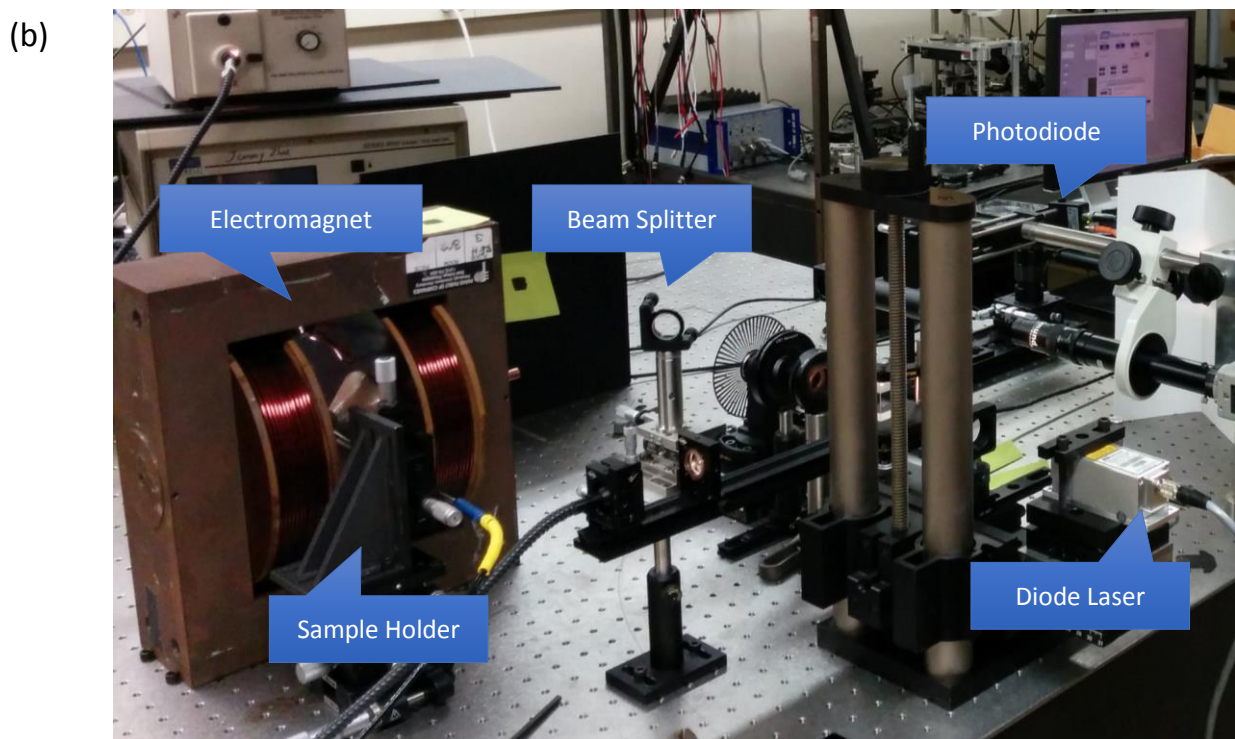
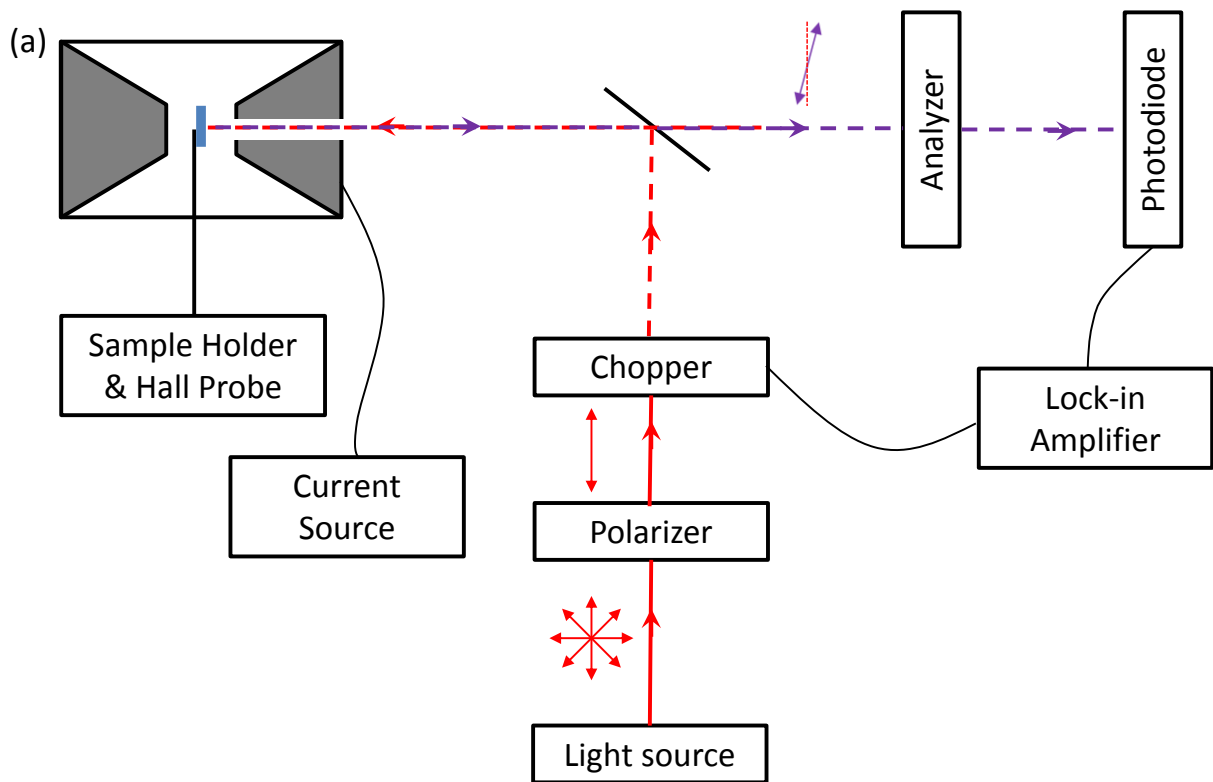


Figure 3-4: (a) Schematic of the MOKE setup (b) Picture of the MOKE setup

The light source consisted of a diode laser purchased from CVI Melles Griot with an output wavelength of 642 nm and adjustable power (<100mW). The laser beam was directed first through a polarizer to linearly polarize the beam, and then towards the sample by means of a beam splitter. The sample is mounted between the poles of an electromagnet powered by a voltage controlled Kepco current source ( $I_{\max} \sim 20$  A). Holes are drilled into the pole pieces of the magnet so that the laser beam can be incident on the sample. The reflected beam is passed through an analyzer and then onto a silicon photodiode. An optical chopper in the incident beam path is connected to a lock-in amplifier as a reference signal (5 kHz) along with the photo-diode which records the output signal. The polarizer and analyzer are first set at  $90^\circ$  with respect to each other (extinction condition), and then the analyzer is rotated by  $3^\circ$  to increase the output signal. A Labview program was utilized to vary the current (thereby the magnetic field), and record the voltage output (which depends on the magnitude and direction of film magnetization). A calibration plot of current applied to the electromagnet vs the generated magnetic field is shown in Figure 3-5(a). This was measured using a Hall probe placed at the center of the gap between the two pole pieces of the electromagnet. As we can see from the plot, for the maximum current of 20A, a field of 12.5 kOe was generated. Figure 3-5 (b) shows the magnetic hysteresis loops of a granular CoPt-SiO<sub>2</sub> magnetic media film with perpendicular anisotropy and exchange decoupled magnetic grains. A reference loop taken using the AGM (described in section 3.4) matches well with the hysteresis loop generated from the MOKE setup. The laser power used in this case was 15mW and the beam was unfocused. The opening of the hysteresis loop obtained from MOKE at the high positive fields is due to sample drift. In some cases, the laser spot was focused by means of a lens of 15 mm focal length inserted into the pole piece of the electromagnet and a beam spot size of approximately 17  $\mu\text{m}$  could be obtained. This way, samples with different patterned regions can be studied. The

MOKE measurements presented in this thesis were recorded either using this setup or another similar setup constructed by Zhengkun Dai.

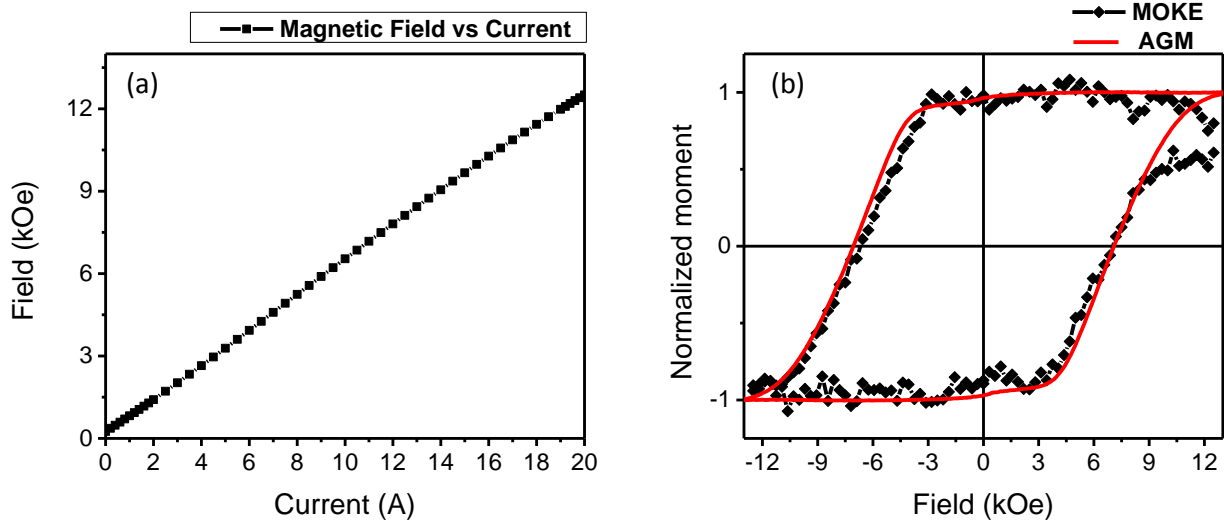


Figure 3-5: (a) Calibration curve showing current applied to magnet vs magnetic field generated (b) comparing magnetic hysteresis loops measured from MOKE and AGM for a perpendicular magnetic thin film

# CHAPTER 4

## Background on Block Copolymers

### 4.1. Introduction

Block copolymers are materials which consist of two or more ‘blocks’ of homopolymer chains covalently bonded in a linear fashion. The molecular formula of two common di-block copolymers poly (styrene-*b*-methacrylate) and poly (styrene-*b*-dimethylsiloxane) are shown in Figure 4-1. The different natures of these polymer chains which however are constrained by the covalent bond results in interesting ‘phase separation’ behavior. Recently, there has been much research in these materials due to their self-assembly into nanostructures with periods around 5-100 nms, with potential applications in nanolithography and bit patterned magnetic recording media[39], [41]–[43], [64]–[68]. Micro-phase separation of block copolymers occurs since the two blocks of homopolymers are usually immiscible and the equilibrium microstructure is thus the one where they have a minimum interfacial area. However, macro-scale phase separation is prevented since these two blocks are covalently bonded together.

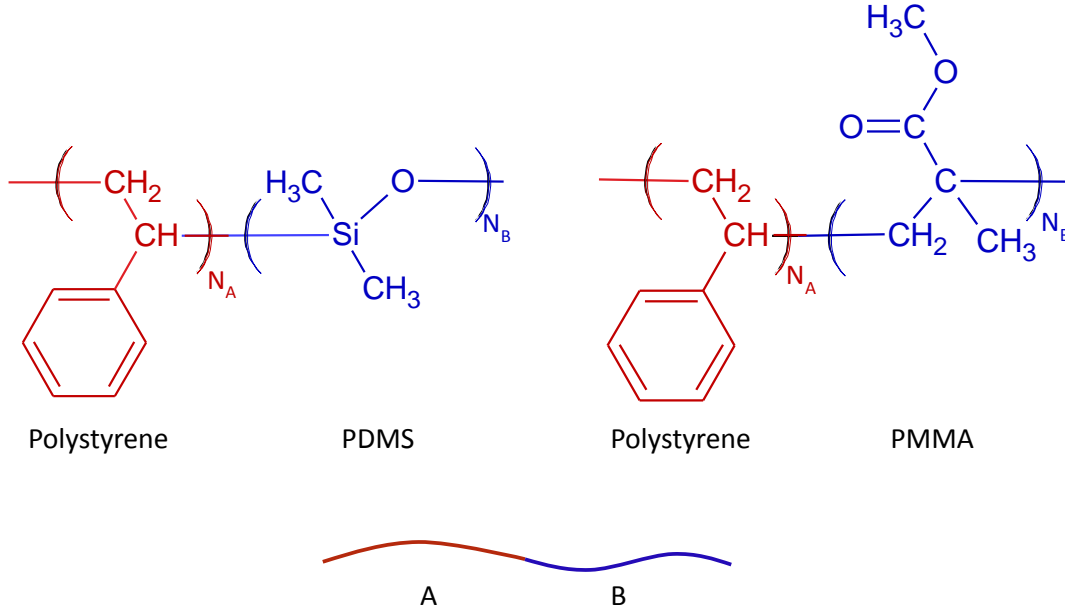


Figure 4-1: Molecular formulae of commonly used BCPs PS-PDMS and PS-PMMA

## 4.2. BCP Thermodynamics: Flory-Huggins Theory

The Flory-Huggins theory is one simple way to understand the thermodynamics of such a micro-phase separation process. The Flory-Huggins approach examines the Gibbs free energy of mixing ( $\Delta G_{mix}$ ) of these polymers. Using a quasi-lattice approach similar to that used to explain the behavior of solid solutions in the regular solution model, the contributions of enthalpy and configurational entropy of mixing are used to develop an expression for  $\Delta G_{mix}$  as follows[69]:

$$\Delta G_{mix} = RTn_s \left( \chi\phi_A\phi_B + \frac{\phi_A}{N_A} \ln \phi_A + \frac{\phi_B}{N_B} \ln \phi_B \right)$$

where 'R' is the gas constant, 'T' is temperature, 'n<sub>s</sub>' is the total number of sites in the modeled polymer lattice, ' $\phi_i$ ' is the volume fraction of the i<sup>th</sup> block, 'N<sub>i</sub>' is the degree of polymerization,

and ‘ $\chi$ ’ is the Flory-Huggins parameter. For mixing to occur spontaneously,  $\Delta G_{\text{mix}}$  should be  $< 0$ . The configurational entropy of the system always increases upon mixing as this results in a larger number of configurations of the system, and hence an increase in entropy, which is given by  $S = k \ln \Omega$ , where  $\Omega$  is the number of possible configurations of the system. Assuming ideal chain behavior for the polymer chains, this gives us the expression  $\Delta S_{\text{mix}} = -Rn_s \left( \frac{\phi_A}{N_A} \ln \phi_A + \frac{\phi_B}{N_B} \ln \phi_B \right)$ . As we can see, this term is always positive and lowers the  $\Delta G_{\text{mix}}$ . However, given that  $N_i$  for polymers is usually a large number, the contribution of  $\Delta S_{\text{mix}}$  is generally quite low. The phase separating behavior is thus due to the enthalpy term:  $\Delta H_{\text{mix}} = RTn_s(\chi\phi_A\phi_B)$ . If the ‘ $\chi$ ’ parameter is positive (negative), the enthalpy term favors de-mixing (mixing). The Flory-Huggins theory is a mean-field theory, which thus assumes that each polymer chain in the system experiences a mean field due to the presence of the other polymer chains in the system. The local interactions, such as those due to excluded volume interactions, conformational entropy etc. are also accounted for using the ‘ $\chi$ ’ parameter in practice.

In terms of  $\Delta G_{\text{mix}}$ , the two important parameters from the expression that helps us pick polymers which phase-separate are thus ‘ $\chi$ ’: the Flory-Huggins parameter, and  $N$ : the degree of polymerization. A large positive ‘ $\chi$ ’ favors phase-separation since it makes the enthalpy large and positive. A large  $N$  lowers the negative contribution to  $\Delta G_{\text{mix}}$  from the entropy term and thus favors phase separation. Often in literature, these two parameters are combined as the product  $\chi N$ , and a large positive value of this product is desirable for phase separation.

In a block copolymer system, this micro-phase separation process can be considered as a transition from a mixed to an ordered state, as illustrated in Figure 4-2(reproduced from [70]). The

driving force for ordering arises from the positive enthalpy of mixing. Both configurational and conformational entropy oppose the ordering. We already discussed the effect of configurational entropy through the Flory-Huggins model. The change in conformational entropy of the system arises since ordering is nearly always accompanied by a stretching of the polymer chains, which lowers the number of possible conformations. The effect of this entropy term can be seen from the critical value of  $\chi N$  which is necessary for micro-phase separation. In the case of polymer blends, as discussed in the Flory-Huggins theory above, this critical value  $(\chi N)_c$  is 2, i.e. if the value of  $\chi N$  for the system is less (greater) than 2, the system will remain in the single phase (two-phase). For a symmetric block copolymer system however, this critical value becomes approximately 10[69] due to the decrease in the conformational entropy term, as seen in Figure 4-3(a).

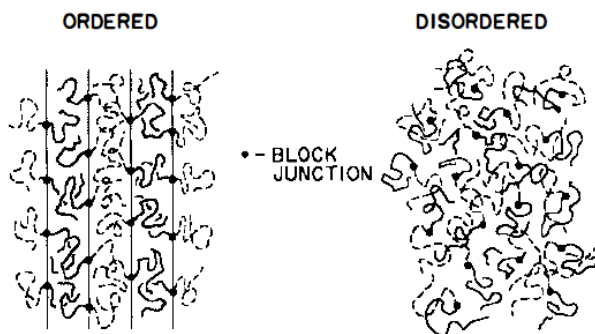


Figure 4-2: Schematic of the ordering in BCPs[70]

### 4.3. BCP Morphologies

The morphology of the ordered state is the one which has the minimum interfacial area between the two blocks, with the constraint that a certain volume fraction of the two blocks have to be accommodated, which will thus be the morphology with the lowest Gibbs free energy. Depending on the volume fractions of the two blocks, different morphologies can be obtained, as outlined in

the structural phase diagram in Figure 4-3, which was computed with a self-consistent mean field theory[43], [71], [72]. In this diagram, we see that if  $\chi N$  is too small, a homogenous mixed phase is obtained, and as the  $\chi N$  becomes sufficient for phase separation, an ordered state is obtained whose morphology is determined by the volume fractions of the two blocks.

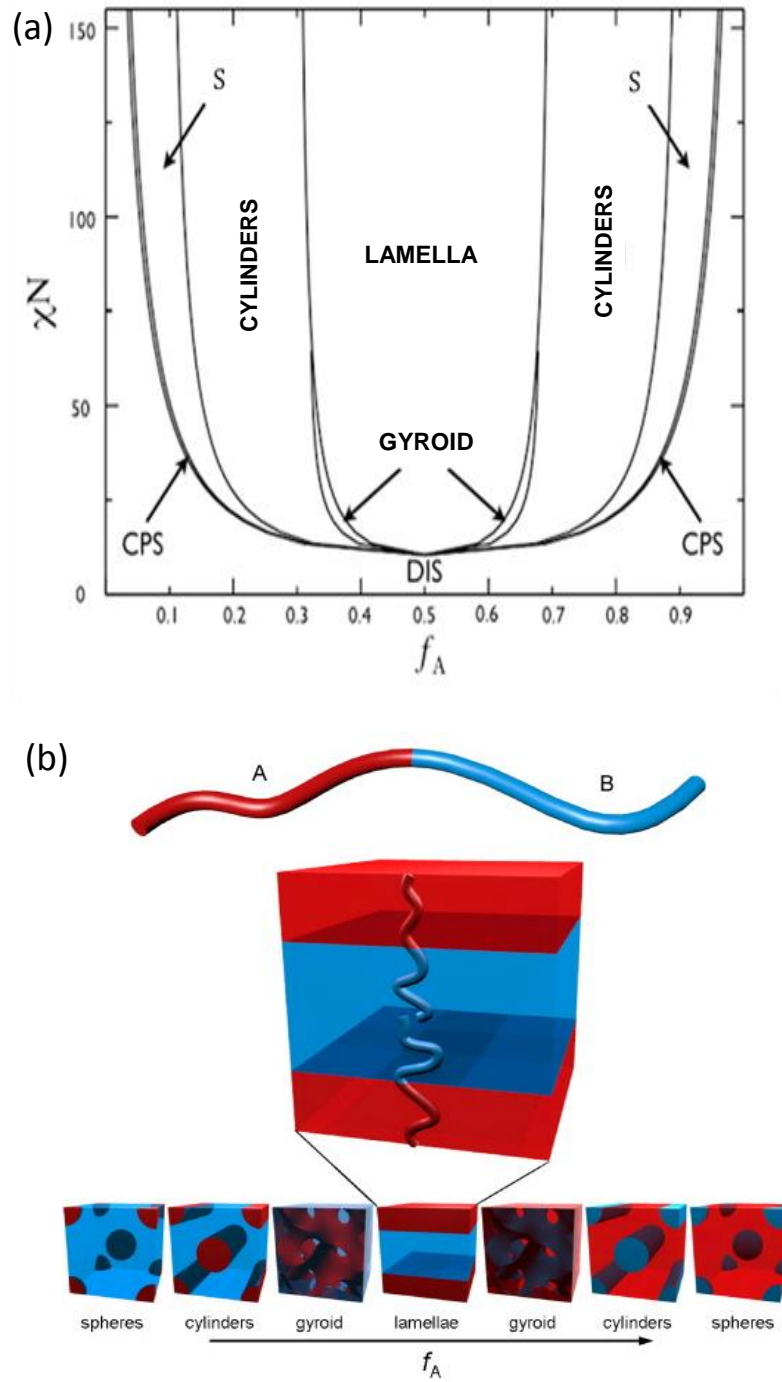


Figure 4-3: BCP morphologies (a) structural diagram[71], [72] (b) for thin films[43]

#### **4.4. BCP Thin Films**

The earlier paragraphs describe the behavior of the block copolymers in bulk. When thin films of block copolymers are used, as in our research for example, surface energetics and thickness of the films also play a critical role. The effect of confinement arises when the thickness of the block copolymer film is not commensurate with the period of the nanostructure formed after phase separation. In such a case, the polymer chains will have to stretch or be compressed to accommodate the excess polymer, which results in an unfavorable reduction in entropy. In these cases, the polymer films spontaneously form islands and holes to accommodate the chain stretching/compression. Surface energetics play a role depending on the relative wetting behavior of the two blocks with the surface. To understand this, let us consider a lamellar block copolymer A-B in contact with a substrate C. If B-C interactions are favorable, we will obtain a layered morphology where the alternating A-B layers are parallel to the substrate surface in order to maximize the B-C interface area. On the other hand, if A and B are neutral to C, no particular interactions are preferred, and the stacking of A-B layers will be perpendicular to the substrate surface[67].

#### **4.5. Choice of Block Copolymer**

In this project, we worked predominantly with the diblock copolymer poly (styrene-b-dimethyl siloxane), henceforth abbreviated as PS-b-PDMS. Figure 4-1 shows the molecular formula of this block copolymer (BCP) where  $N_A$  and  $N_B$  are the degrees of polymerization for the individual blocks. There are two key reasons due to which this polymer is suitable for this project. PS-b-PDMS has a high Flory-Huggins ( $\chi$ ) parameter of 0.26[73] at room temperature. We discussed in

Section 4.2 of this chapter that  $\chi$  is an important indicator of the phase-segregating tendency of the BCP, which is proportional to  $\chi N$ , where  $N$  is the degree of polymerization of the BCP. Degree of polymerization is a measure of the chain length, or the molecular weight of the polymer. For obtaining polymers with small sub-20 nm features, it is thus advantageous to have a high  $\chi$  value so that  $\chi N$  is still sufficient to drive micro-phase separation[69]. The  $\chi$  value for PS-b-PDMS is higher than other commonly studied BCPs, such as poly (styrene-b-methyl metha acrylate) ( $\chi = 0.04$  to  $0.06$ )[74] or poly (styrene-b-ferrocenyl dimethyl silane) ( $\chi = 0.08$ )[75]. The other critical advantage of PS-b-PDMS lies in reactive ion etching (RIE) which is a commonly used pattern-transfer technique in subtractive patterning processes. From the molecular formula shown earlier in Figure 4-1, we see that the polystyrene block of the BCP has a carbon-based backbone, while the polydimethylsiloxane (PDMS) has a silicon-based backbone. This property can be exploited in reactive ion etching, in which the polystyrene block etches much faster in an oxygen plasma due to its carbon based backbone as compared to PDMS[40], [76]. The volume fraction of the PDMS minority block was kept between 15-20%. In this range, as discussed in Section 4.3 of this chapter, we obtain spheres of one block in the other block's matrix upon the micro-phase separation of the block copolymer. While the morphology is determined by the volume fraction of the minority block, the 'pitch' of the resulting patterns depends largely on the overall molecular weight as discussed in the next section.

## 4.6. Manipulating Feature Sizes in BCP Patterns

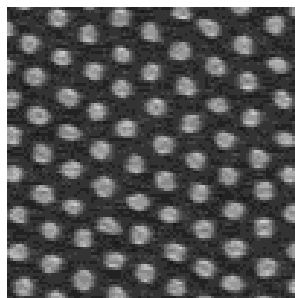
The molecular weight of the BCP is directly related to the chain lengths of the polymer blocks. BCPs of different molecular weights result in different pitch or center-to-center spacing between

the minority block spheres. Table 4-1 shows a list of the PS-b-PDMS BCPs that we studied, along with the molecular weights and PDMS volume fractions, and Figure 4-4 shows the resultant block copolymer microstructure. The fabrication details of these films will be described in the next chapter.

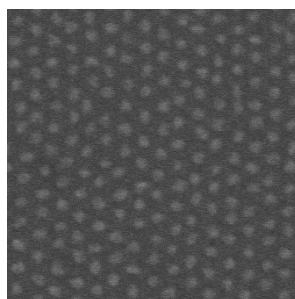
Table 4-1: Molecular weights and minority volume fractions of PS-b-PDMS

<b>Polymer ID</b>	<b>Molecular weight (kg/mol)</b>	<b>Volume fraction of minority block (%)</b>
PSD1	51.5	17.7
PSD2	18	17.9
PSD3	13.9	17.2

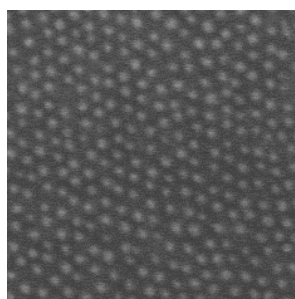
PSD1  
Mwt: 51.5 kg/mol  
Pitch ~ 36 nm  
Density ~ 0.6 Tdpsi



PSD2  
Mwt: 18 kg/mol  
Pitch ~ 20 nm  
Density ~ 1.9 Tdpsi



PSD3  
Mwt: 13.9 kg/mol  
Pitch ~ 17 nm  
Density ~ 2.6 Tdpsi



**100 nm**

Figure 4-4: SEM micrographs of PS-b-PDMS BCP with different molecular weights

In the plane-view SEM micrographs shown above, we see a regular hexagonal array of spheres of PDMS (bright) in a polystyrene matrix (dark). The distribution in pitch for these cases ranges from approximately 8% for PSD1 to 12% for PSD3. The distribution in pitch and the number of defects in the pattern, such as a missing dot or connected dots increases with decreasing molecular weight. As we discussed in Section 4.2, the enthalpic contribution to the free-energy term which is responsible for micro-phase separation in BCP is proportional to  $\chi N$ , where  $\chi$  is the Flory-

Huggins parameter, and  $N$  is the degree of polymerization. As molecular weight decreases,  $N$  decreases, and thus the enthalpic penalty for a mixed phase reduces, resulting in the presence of a larger number of defects in the pattern.

## **4.7. Summary**

Background on the block copolymer self-assembly and micro-phase separation were presented. The Flory-Huggins parameter and pattern transfer considerations enabled the choice of poly (styrene-*b*-dimethyl siloxane) as the block copolymer for this project. The details regarding block copolymer fabrication are presented in the next chapter.

# CHAPTER 5

## Nanofabrication Techniques

### 5.1. Introduction

The general approach for template fabrication was presented in chapter 2. In this chapter, we introduce the various fabrication techniques used and present the process development details. The various steps in the general process flow for template fabrication are:

- Sputtering the template layer and film stack
- Spin coating the block copolymer film and annealing
- Pattern transfer into the hard mask using Reactive Ion Etching
- Ion-milling into the template layer

### 5.2. Sputtering the Template Layer and Film Stack

Sputtering is a physical vapor deposition technique which occurs in a chamber that has been pumped down to a low base pressure, of the order of  $10^{-7}$  or  $10^{-8}$  torr. A schematic of the sputtering process is shown in Figure 5-1. An inert (or sometimes reactive, depending on the application) gas such as Argon (Ar) is first introduced into the chamber bringing the pressure inside to the mTorr range. A plasma is then generated in the chamber by applying a bias between the cathode and anode. A stray electron close to the cathode gets accelerated towards the anode due to the bias. During this process, it collides with the Ar atoms present in the chamber and if the energy of the

electron at this point is higher than the ionization energy of Ar, the Ar atom gets ionized, releasing another electron into the system. These two electrons are subsequently accelerated toward the anode, and they continue to ionize other Ar atoms, resulting in a stable plasma due to this avalanche effect. The  $\text{Ar}^+$  ions that are generated are accelerated towards the cathode, and they impinge upon it. A fraction of these collisions result in the release of atoms comprising the cathode, which then get deposited all over the chamber, and also on the substrate, thus forming a thin film.

Sputtering can be classified broadly into DC or AC depending on the power supply used. DC plasma is the simplest method, but when used to sputter insulators, positive charge gets built up on the surface of the cathode/target preventing  $\text{Ar}^+$  ions from further knocking off target atoms. In order to circumvent this issue, an AC power supply is used, where the positive and negative charges are switched with a MHz (radio-frequency) preventing charge buildup and facilitating the sputtering process. In order to make the sputtering process more efficient, a magnet is sometimes attached to the target. The magnetic field confines the plasma close to the target resulting in a more efficient sputtering process. This is called magnetron sputtering.

A key advantage of sputtering is its ability to deposit alloy films. One way to sputter an alloy film is to modify a sputtering target of A with chips of B which are attached to it using a conductive epoxy. This way, both A and B are sputtered off by the plasma, resulting in an alloy film. Another way to sputter alloy films involves confocal sputtering where two targets are lit up at once, and they are oriented onto the substrate so that both films are being deposited at the same time, resulting in an alloy film. A third way is to use a composite target in which the target itself is an alloy.

Parameters such as Ar pressure, RF/DC power, bias and film growth rate have to be optimized to obtain the required sample properties, as will be described in appropriate sections in the

forthcoming chapters. Four sputtering systems: Z400#1, Nanofab machine #2, #3 and #4 were used in this project. A profilometer was used to determine the sputtering rate by sputtering a film on a masked substrate. After sputtering for a pre-determined time, the mask was removed and a step was thus created, whose height was then measured using the profilometer to determine the average sputtering rate.

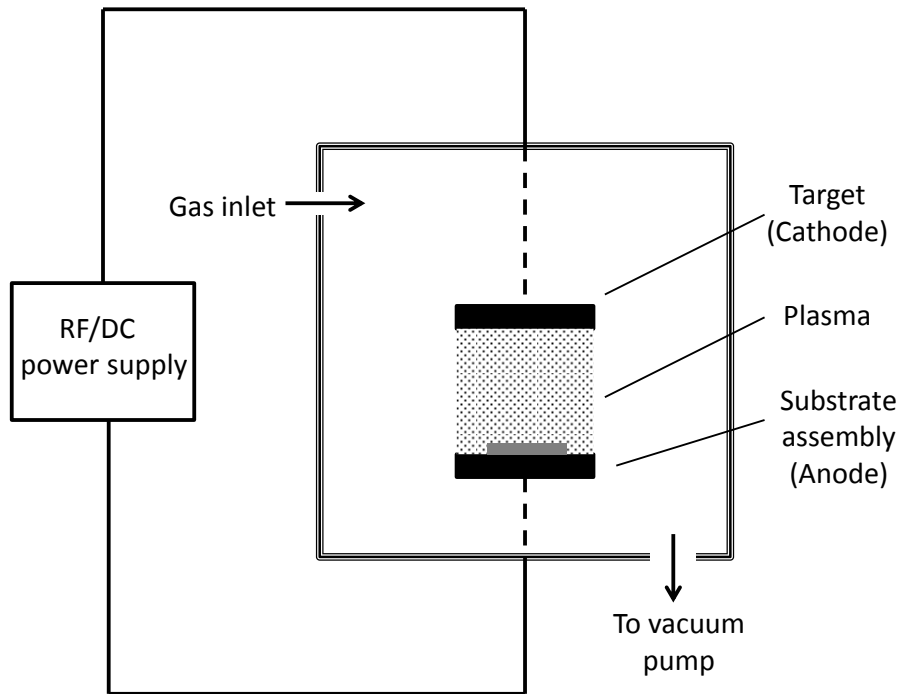


Figure 5-1: Schematic of the sputtering process

The choice of template layer and its fabrication for the templated growth of PMR media is discussed in detail in the next chapter. The hard mask was chosen to be amorphous carbon (am-C). Carbon is an excellent hard mask for ion-milling into underlying materials because of its extremely low ion-milling rate of approximately 3.5 nm/min. On the other hand, it can be etched using an oxygen plasma in a Reactive Ion Etching system (approximately 10 nm/min). As mentioned briefly in Section 4.5, this high etch rate in an oxygen plasma can be used for pattern

transfer from a PS-b-PDMS film into the carbon mask. A 20 nm carbon film was sputtered using sputtering system #4 using DC sputtering with a power of 150W, 5 mT Argon pressure at a rate of 2.2 nm/min. This sputtered carbon film had an RMS roughness of approximately 6.1 Å as measured using Atomic Force Microscopy and is suitable for the fabrication of block copolymer films.

### **5.3. Spin Coating of BCP Film**

Spin-coating is one of the most convenient and reproducible methods to obtain thin films of polymers. PS-b-PDMS powders (as purchased from Polymer Source Inc.) are dissolved in toluene. Syringe filters with pore sizes of around 0.2 µm are used to remove impurities. This solution is then dispensed onto the sample wafer which is mounted on a vacuum chuck. During this dispensing step, the wafer is rotated at a low speed of about 600 rpm (dynamic dispense technique). This aids the spreading of the solution over the entire sample. The rotation is then accelerated to the final spinning speed, which is usually between 2000-6200 rpm. The spin speed chosen depends on the concentration and viscosity of the polymer solution, as well as the desired final film thickness. During the spinning, the centrifugal force pushes the solution to the edges, and once surface tension is overcome, the solution falls off, leaving behind a thin film of the solute[77].

The concentration of the BCP solution and the spin-coating parameters such as spread speed, spin speed and the respective times were optimized so that one monolayer of PDMS spheres in a PS matrix can be obtained. The thickness required is thus just slightly higher than the pitch of the block copolymer, in order to account for the segregation of a PDMS layer to the air-film interface[40]. In most cases, the concentration and spin-coating conditions were picked based on

the resultant block copolymer microstructure, observed using the SEM. Unless specified otherwise, the following spin-coating conditions were used for BCP thin films.

Table 5-1: Summary of spin-coating conditions

Step	Speed (rpm)	Time (sec)
Spread	600	6
Spin	4000 (500 rpm per sec ramp)	60

#### 5.4. Annealing of BCP Film

Spin coating is not an equilibrium process. In order to obtain the equilibrium microstructure of the block copolymer film (refer Figure 4-3), we increase the mobility of the polymer chains through solvent or thermal annealing. In case of thermal annealing, the polymer film is subjected to an elevated temperature close to its glass transition temperature ( $T_g$ ) by placing it in a vacuum oven. The annealing temperature and time have to be optimized. While too little mobility may cause a poorly micro-phase separated microstructure, too high a mobility may cause dewetting of the polymer film. Further, the  $\chi$  (Flory-Huggins) parameter, which is a measure of the driving force for micro-phase separation, is inversely proportional to temperature, and thus a higher temperature need not necessarily provide the most regular pattern[69]. The SEM micrographs illustrating the effect of thermal annealing on the block copolymer microstructures are shown in Figure 5-2. The annealing temperature for PSD1 was varied from 130 to 222°C, with a constant annealing time of 24 hours. For PSD1, an average pitch of 35 nm and the lowest pitch distribution of ~ 8.6% was obtained for the 175 °C case, while further increase in temperature both worsened the pitch distribution (~ 9.8% for 190°C case) and caused the onset of dewetting. The onset of

dewetting is indicated by the appearance of holes in the film which can be seen in the lower magnification image for the 192°C case. At 222°C, dewetting was very advanced and only small parts of the film remained. For PSD2, which has a lower molecular weight, a lower pitch and thus a lower optimal film thickness (to obtain one monolayer of PDMS spheres in a PS matrix), we see that the dewetting of the film is complete at 192°C. A temperature 130°C resulted in the lowest pitch distribution of ~ 10% for PSD2, with a mean of 20 nm. For PSD3, with an average pitch of 17 nm, we found that even at 115°C, holes started appearing in the pattern. A temperature of 95°C on the other hand is clearly insufficient to form a regular pattern as seen from the SEM image. Improvement in the wetting of the block copolymer thin film can be achieved by using different ‘brush’ layers between the substrate and the polymer film[40][67], and also by the use of solvent annealing[67]. Further, the thickness of the block copolymer film is a critical parameter in the prevention of dewetting. Islands and holes start to form in the film if the film thickness is not commensurate to the pitch of the BCP as shown in Figure 5-3. Parts (a) and (b) are reproduced from [78], showing the effect of an incommensurate thickness during the annealing of the BCP. When we zoom in, shown in Figure 5-3 (c), which is an example from our case, (partially etched using RIE), we see a region of two layers of spheres and one layer of spheres.

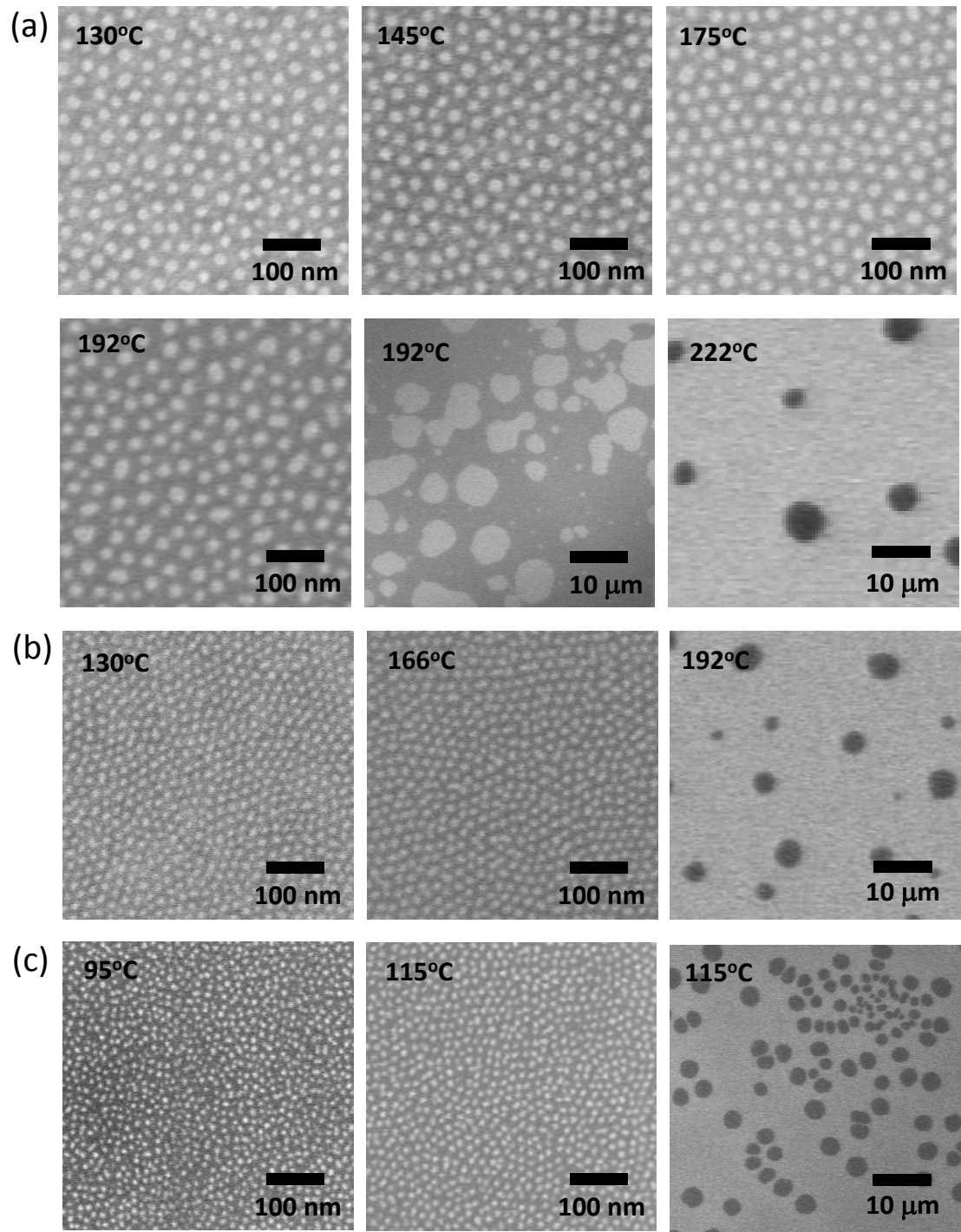


Figure 5-2: Plane-view SEM micrographs illustrating the effect of temperature on the micro-phase separation of (a) PSD1 (b) PSD2 and (c) PSD3

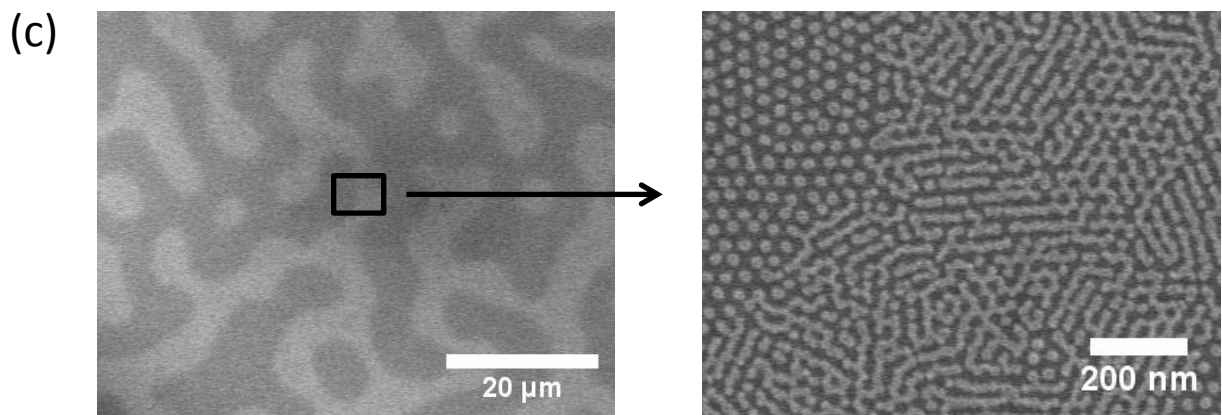
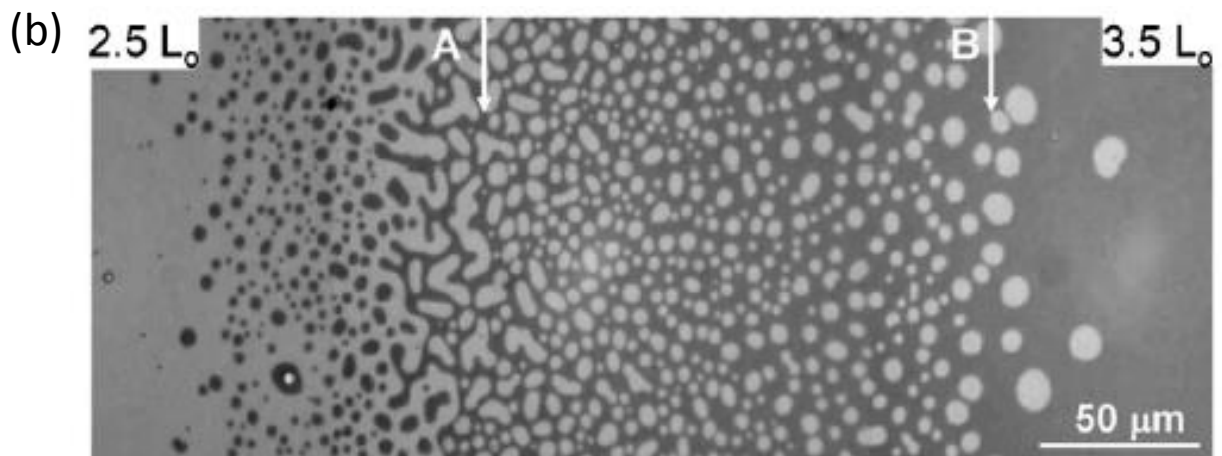
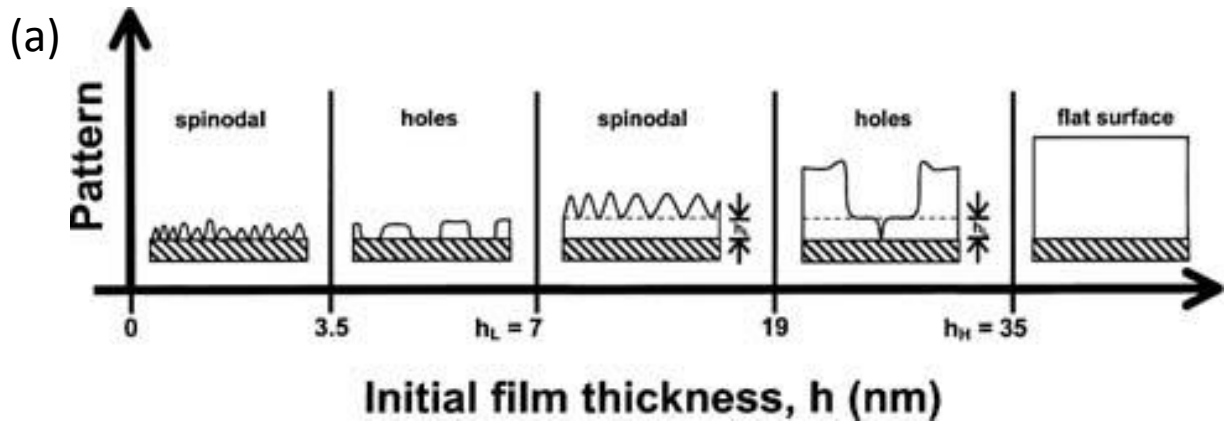


Figure 5-3: Effect of thickness of BCP film in the solvent annealing process: (a) cross-section schematic of thickness evolution with annealing[78] (b) plane-view SEM micrographs[78] (c) zoomed-in image showing regions with one and two layers of PDMS spheres

We also explored the use of solvent annealing for the block copolymer micro-phase separation process. Here, the polymer film is subjected to the vapor of a suitable solvent. The schematic of the simple procedure we followed for solvent annealing is shown in Figure 5-4(a). Since polymer-solvent molecule interactions are energetically favorable, the polymer film absorbs the solvent and swells, as shown in Figure 5-4(b).

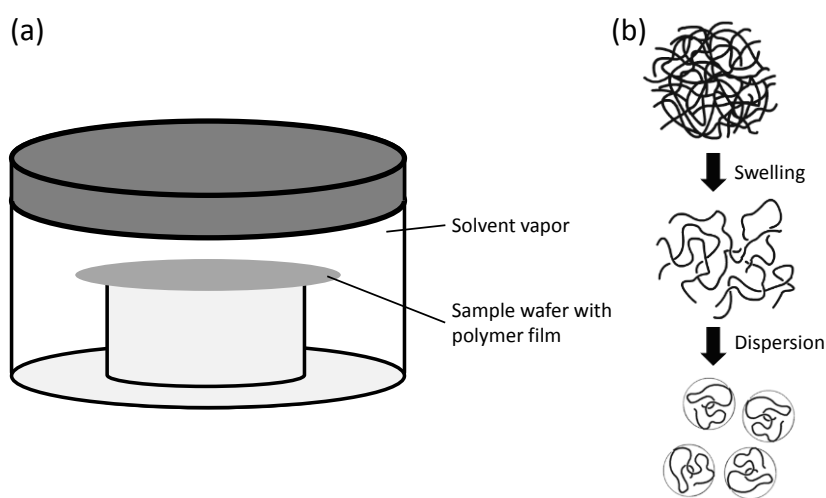


Figure 5-4: Schematic of (a) simple solvent annealing setup (b) interaction of solvent with the polymer chains

The chains have an increased free volume and thus increased mobility. The vapor pressure of the solvent and the annealing time are optimized to obtain the required microstructure. If the vapor pressure or the annealing time is too low, the ordering of the BCP domains is affected. However, if it is too long, the polymer film dewets, which is analogous to the dispersion of polymer chains in solution as shown in Figure 5-4(b). The degree of swelling of the polymer film also depends on the nature of the polymer chain-solvent interactions, thus making the choice of solvent very important. Solvent vapor annealing is now a very popular technique for facilitating the micro-

phase separation of block copolymers in a short-time scale, and with very few defects, particularly for applications in next-generation lithography [79]. In order to better control the solvent annealing process, precise control of the solvent vapor flow rates, vapor pressure, and monitoring of the thickness in-situ using spectral reflectometry or ellipsometry has been explored recently[80]. Figure 5-5 shows an example of the effect of solvent annealing on a PSD1 block copolymer thin film. This BCP forms a hexagonal lattice of PDMS spheres in a PS matrix with a center-to-center spacing of approximately 35 nm as discussed earlier.

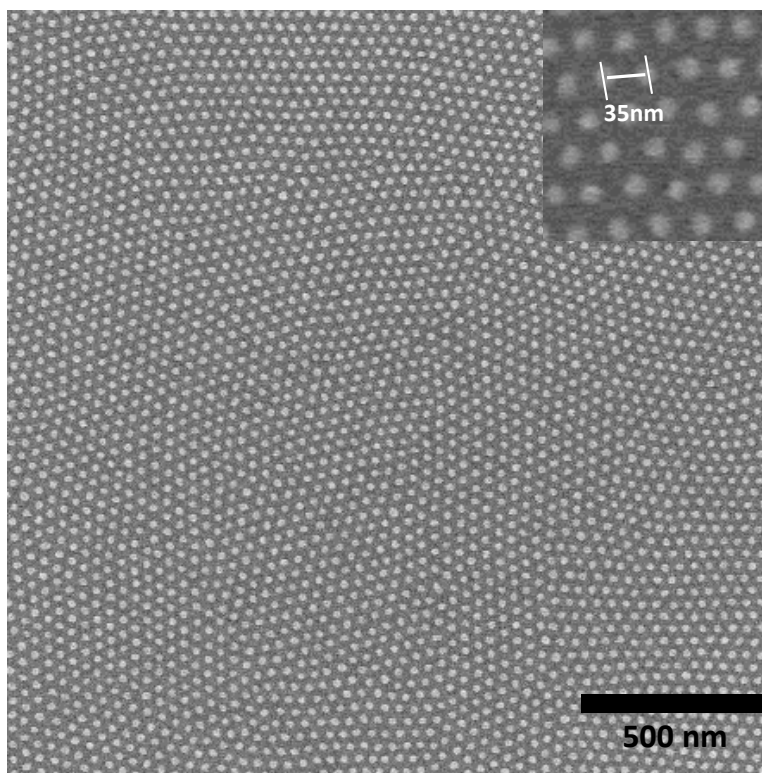


Figure 5-5: Plane-view SEM micrograph showing PSD1 film solvent annealed using toluene; inset with higher magnification

For our studies, we worked with toluene vapor. Toluene is a good solvent for both PS and PDMS, as indicated by the Hildebrand solubility parameters ( $\delta_{PS} \sim 18.5$ ,  $\delta_{PDMS} \sim 15$ ,  $\delta_{Toluene} \sim$

18.3)[81][82]. The volume of toluene in the solvent annealing system was varied and a constant time of 3 hours was used. Figure 5-6 shows the effect of increasing toluene vapor in the micro-phase separation of PSD1. In the case of no annealing, we see interlinked PDMS regions, due to the lack of mobility during the spin-coating process. With increasing amount of toluene in the chamber, we see that the defects in the hexagonal lattice of PDMS in the PS matrix get ironed out, and for 19 ml, we get the best results. Further increase in toluene volume resulted in dewetting of the block copolymer. In case of PSD4 (SEM micrographs shown in Figure 5-7), we see that a lot less toluene is required. The time in this case was fixed at 14 hours. Use of 0.2 ml of toluene resulted in dewetting, with certain regions of the film having well-ordered monolayer of PDMS spheres and the other regions most likely having a double layer of PDMS spheres. In the case of 0.1 ml of toluene, we see that the dewetting process has just begun, and small regions with two layers of PDMS spheres have nucleated in a matrix of the film which has a well-ordered monolayer of PDMS. 0.08 ml of toluene was found to be optimum volume for obtaining a uniform monolayer of spheres across the entire substrate, with a well-ordered microstructure. The average pitch was found to be 17.3 nm, with a standard deviation of 9.8%.

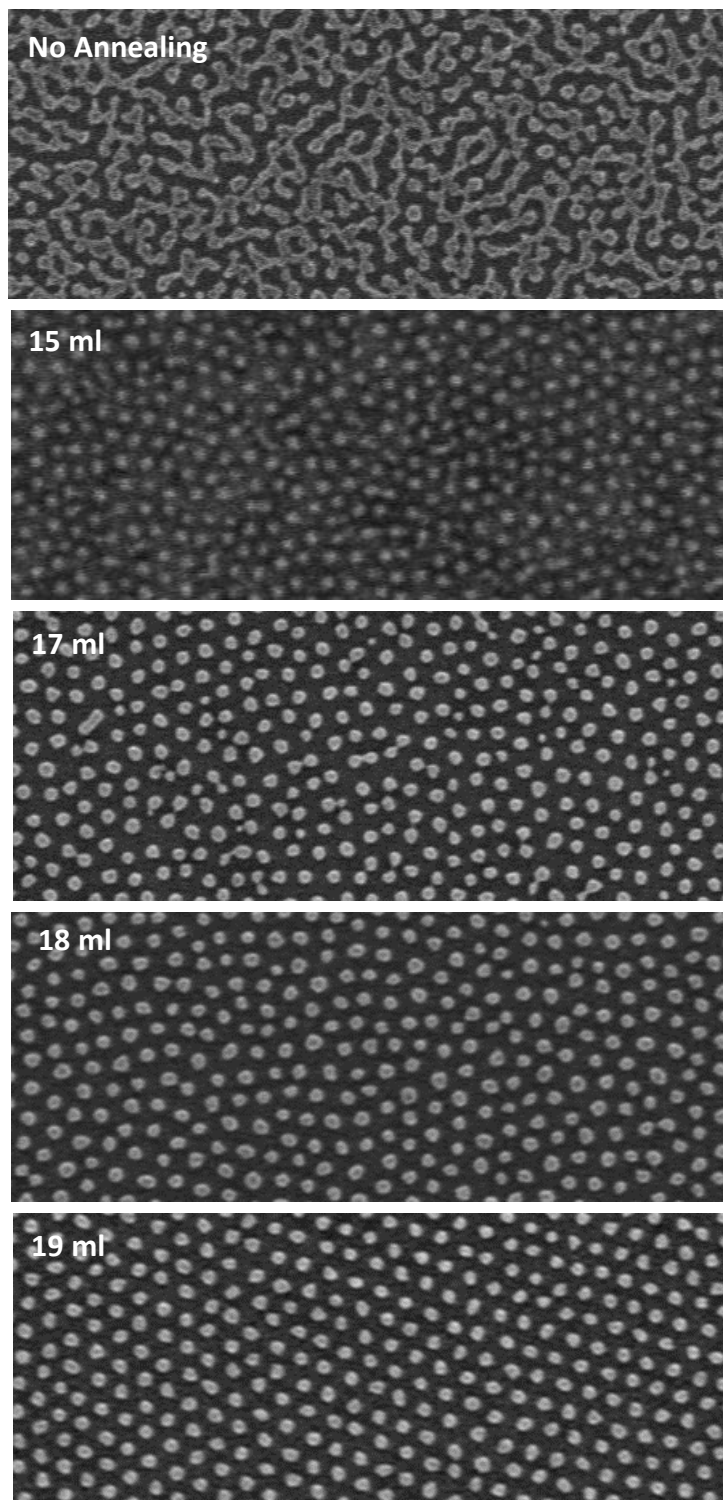


Figure 5-6: Plane-view SEM micrographs showing effect of volume of toluene vapor in the solvent annealing of PSD1

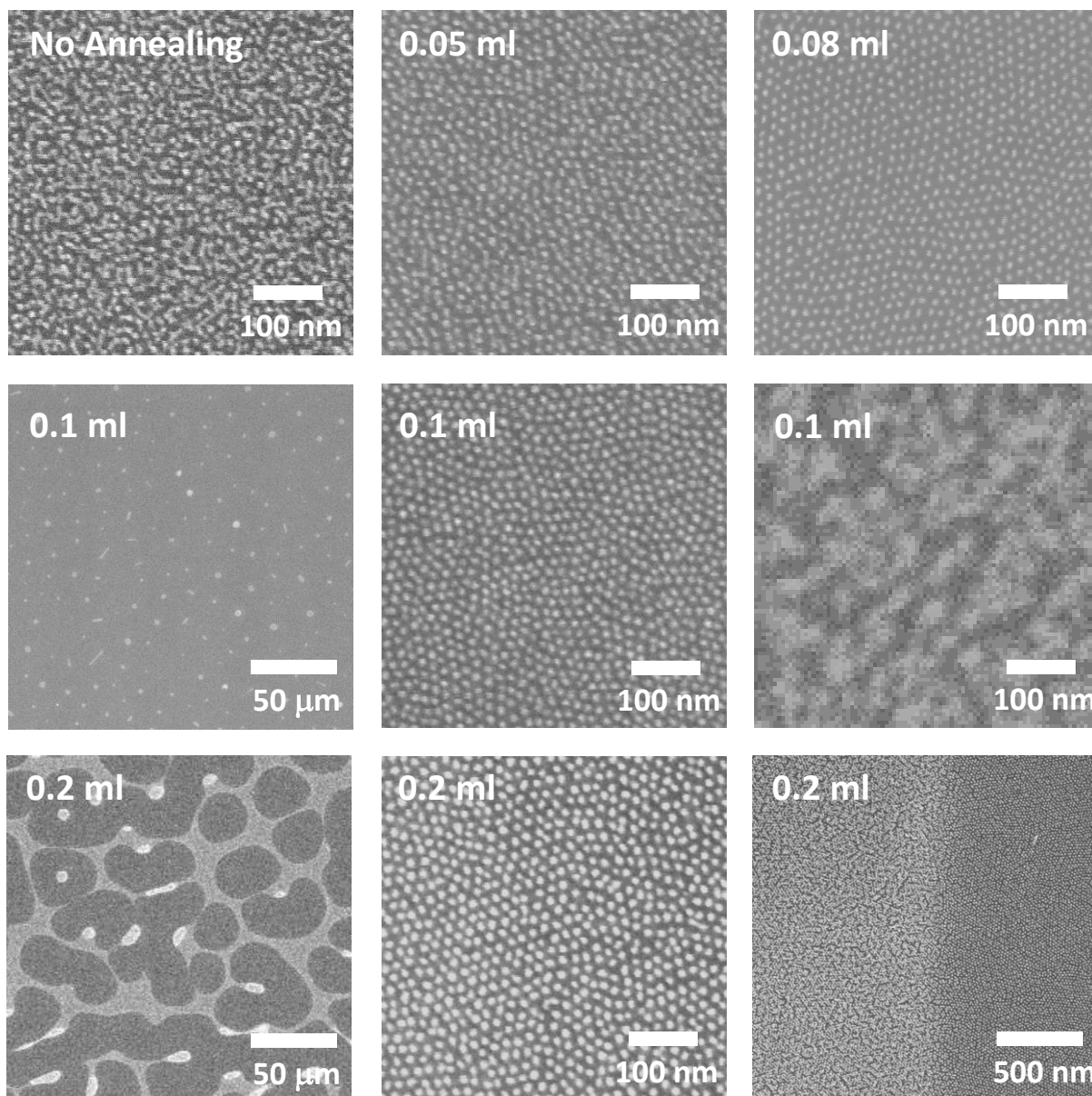


Figure 5-7: Plane-view SEM micrographs illustrating the effect of volume of toluene vapor in the solvent annealing of PSD3

## 5.5. Reactive Ion Etching (RIE)

Pattern transfer techniques commonly used in lithography can be classified into dry/wet etching techniques. Wet-etching techniques involve the use of an etchant solution such as an acid depending on the material to be etched. But wet-etching techniques are difficult to control precisely when small features have to be transferred. Dry-etching techniques such as reactive ion etching (RIE) and ion milling are used in these cases[83].

A parallel-plate reactive ion etching system is shown in Figure 5-8. The chamber, which consists of a wafer platter (anode) and grounded chamber walls (cathode), is typically filled with a chemically reactive gas. When a large radio frequency bias is applied to the wafer platter, electrons are stripped from the reactive gas leading to the formation of ions and radicals (i.e. a plasma) within the chamber. Given a net difference in the size of the anode and cathode, and since the mobility of electrons is far greater than that the heavier ions, a net negative bias is created on the wafer platter leading to a DC potential difference between the electrodes. As a result, the positively charged ions and radicals are directed towards the substrate surface. When the ions and radicals impinge on the surface of the sample, they cause both physical sputtering and chemical etching. By optimizing etch parameters such as gas flow, pressure, bias voltage, and gas combination, it is possible to achieve anisotropic etch profiles while minimizing the effects of physical sputtering.

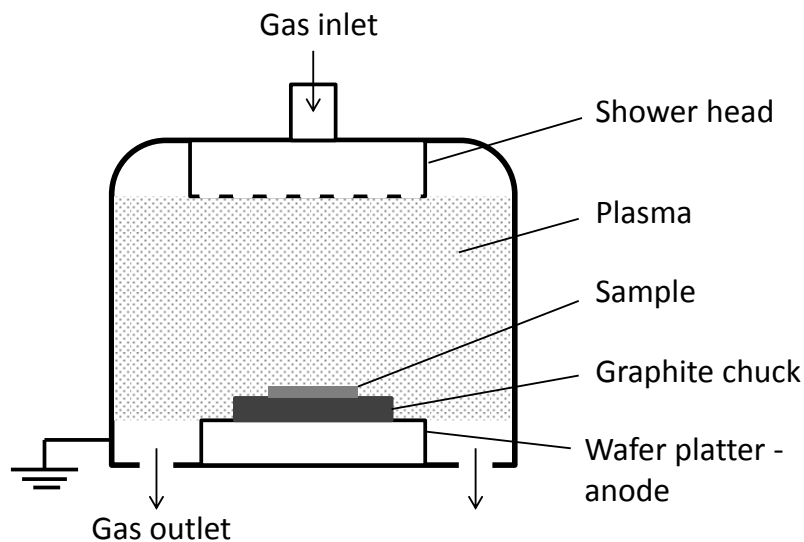


Figure 5-8: Schematic of the Reactive Ion Etching system

As we discussed earlier in Section, one of the important features of this block copolymer PS-b-PDMS is the difference in the properties of the polymer chains of polystyrene and polydimethyl siloxane. The polystyrene has a carbon-based backbone while the polydimethyl siloxane has a silicon-based backbone. A Plasma-Therm 790 Reactive Ion Etching system was used for pattern transfer. The pattern transfer recipes were first developed for PSD1, and then applied to the smaller pitch polymers with modifications as found necessary. As reported in [40], a thin layer of PDMS segregates to the air-film interface due to its low surface tension (19.9 mN/m) as compared to polystyrene (40.7 mN/m). This is first etched using a short  $\text{CF}_4$  plasma of 20-35 seconds. In the next stage, an  $\text{O}_2$  plasma is used to preferentially etch the polystyrene while not etching the PDMS spheres. The key parameters in RIE which had to be optimized were the RF power of the plasma, and the pressure of the gas, both of which indirectly control the bias voltage. It was found that a high pressure, low power oxygen plasma, with a resulting low bias voltage was the most suitable for etching the block copolymer. The etching process in RIE is both due to chemical etching by

the reactive plasma, as well as physical etching due to the bombardment at high bias voltages. On the other hand, a bias voltage is important if the etch has to be anisotropic (directional). From SEM micrographs shown in Figure 5-9, we see that in the case of the block copolymer, a high bias voltage damages the PDMS spheres, and a low bias voltage is more suitable.

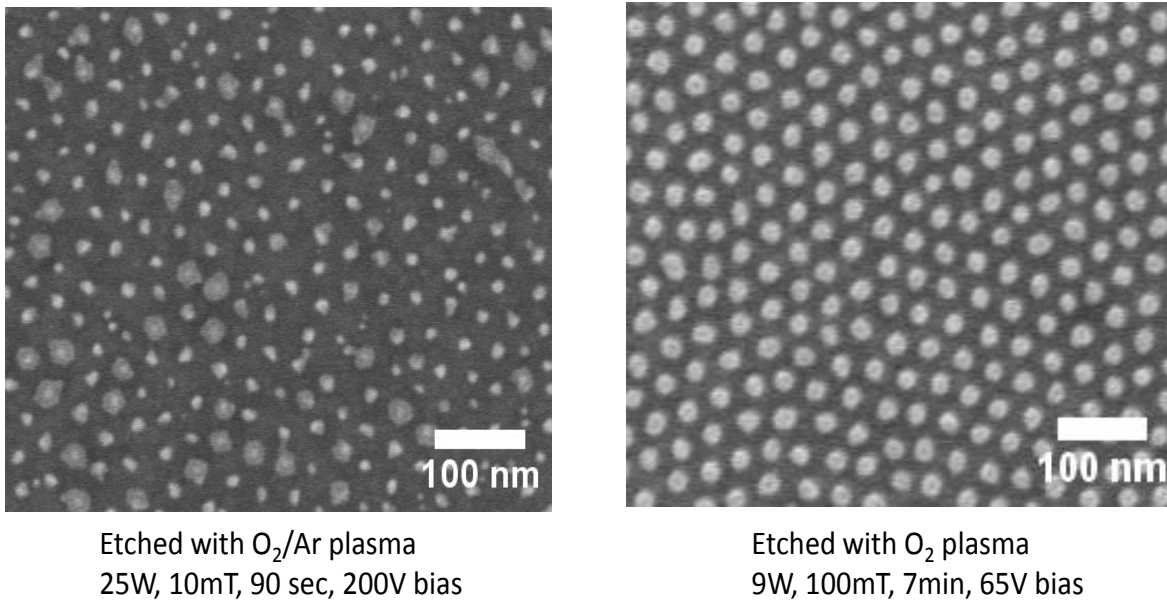


Figure 5-9: SEM micrographs comparing erosion of PDMS spheres due to high bias O<sub>2</sub> plasma in RIE

A suitable mask structure can then be developed to improve the aspect ratio of the ‘pillars’. The first layer of the mask structure was chosen to be amorphous carbon, since this will have a high etch-rate in an oxygen plasma as compared to the PDMS spheres. If high-aspect ratio structures are needed, an alternating film stack of C/SiN<sub>x</sub>/C may be suitable. In case of the smaller-pitch block copolymers, the recipes developed for PSD1 were found to be suitable with modifications in the etching-time of the individual layers. The etch-recipes are tabulated below, in Table 5-2:

Table 5-2: Table of RIE etch parameters

<b>Polymer</b>	<b>Etch-step</b>	<b>Gas</b>	<b>Flow</b>	<b>Power</b>	<b>Pressure</b>	<b>Bias</b>	<b>Time</b>
PSD1	Top PDMS layer	CF <sub>4</sub>	20 sccm	20W	10mT	190V	35 sec
	PS matrix etch	O <sub>2</sub>	20 sccm	9W	100mT	65V	420 sec
PSD2	Top PDMS layer	CF <sub>4</sub>	20 sccm	20W	10mT	190V	25 sec
	PS matrix etch	O <sub>2</sub>	20 sccm	9W	100mT	65V	300 sec
PSD3	Top PDMS layer	CF <sub>4</sub>	20 sccm	20W	10mT	190V	20 sec
	PS matrix etch	O <sub>2</sub>	20 sccm	9W	100mT	65V	270 sec
Mask	am-C mask etch	O <sub>2</sub>	20 sccm	20W	10mT	200V	150 sec

## 5.6. Ion-Milling

In contrast to reactive ion etching, ion milling occurs purely due to physical bombardment of the substrate by a beam of gaseous atoms. An ion milling system, shown in Figure 5-10, consists typically of a Kaufman source in which an electron filament is first heated to produce electrons which are then accelerated towards the anode using an applied bias. On its way, it gains sufficient energy to ionize the gaseous atoms that were introduced, typically a noble gas such as Argon. These gaseous ions are introduced from the Kaufman source into the ion-milling chamber, and accelerated towards the substrate surface with a potential between 300 to 1000 V. The pressure in the chamber is maintained quite low so that the Ar ions do not undergo many collisions. As a result, the beam impinging on the substrate surface is nearly coherent, and vertical. Before the Ar ions reach the substrate surface, a neutralizer releases electrons into the chamber to neutralize the Ar ions into neutral Ar atoms. These atoms then impinge on the substrate causing physical etching.

The advantages of ion milling are the anisotropic nature of the etching process as well as the fact that practically any material can be etched using this technique. The substrate is sometimes placed at an angle with respect to the ion beam to obtain optimum pattern transfer. Issues such as redeposition, beam-damage to the film surface, faceting etc. have to be avoided[32], and the desired pattern-transfer characteristics have to be obtained by optimizing the beam current, beam voltage and the substrate-beam angle.

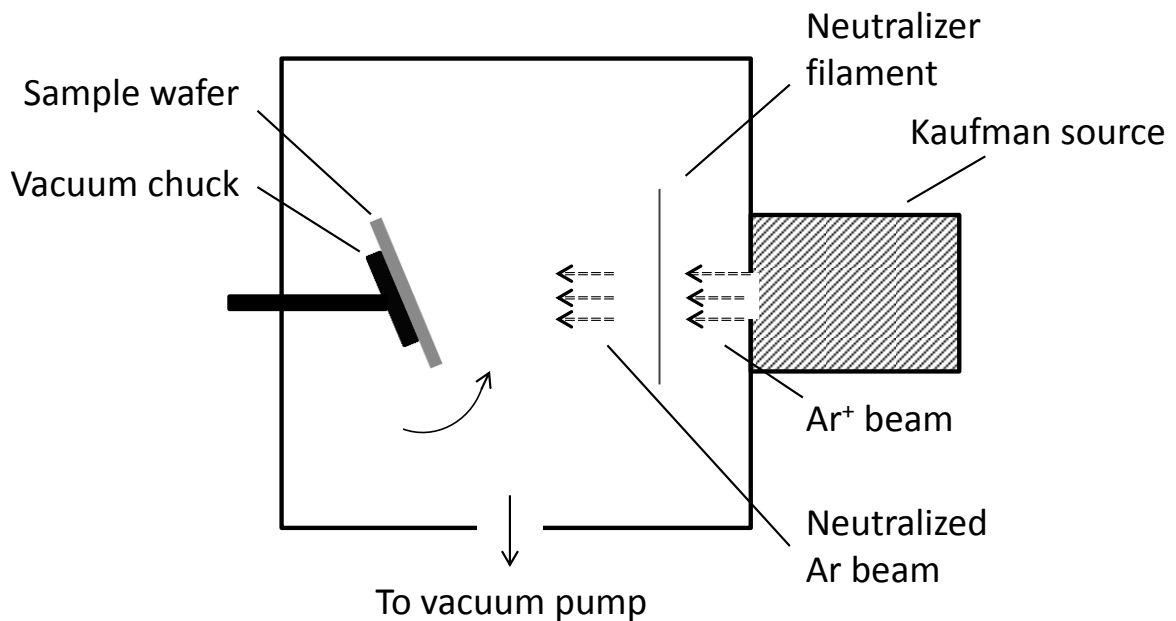


Figure 5-10: Schematic of the ion-milling system

The ion-milling process was performed using a Commonwealth Scientific Ion Mill equipped with a secondary ion-mass spectrometer (SIMS) end-point detector. A film-stack of Ta (3nm)/Pt(30nm)/Ru(15nm)/CoCrPt(20nm)/C(10nm) was sputtered using machine #4, and the end-point detection system was used to determine the etch-rates of these materials. The samples were ion-milled using a 500V, 40mA Ar beam. The substrate was oriented such that the normal to the

substrate plane made an angle of 12.5° with the Ar beam, and the substrate was rotated to ensure uniform ion-milling. When the film stack is milled, the ejected ions are analyzed using a mass spectrometer. Using this technique, individual species of ions can be identified based on their charge/mass ratio. The rate of ion-milling was obtained using the full-width at half-maxima of the various signals in the plot (Figure 5-11), and are tabulated below (Table 5-4). The etch-rate for amorphous carbon could not be calculated using this technique since the background noise for the carbon spectrum in the chamber was too high. It was thus determined by the usual procedure involving the measurement of a step height before and after etching.

Table 5-3: Sputtering conditions in machine #4

<b>Layer</b>	<b>Machine</b>	<b>Power</b>	<b>Pressure</b>	<b>Rate</b>	<b>Thickness</b>
Ta	#4	150W (DC)	2.5mT Ar	24 nm/min	4 nm
Pt	#4	25W (DC)	2.5mT Ar	7.8 nm/min	30 nm
Ru	#4	93W (DC)	2.5mT Ar	13.7 nm/min	15 nm
CoCrPt	#4	50W (DC)	2.5mT Ar	12.3 nm/min	20 nm

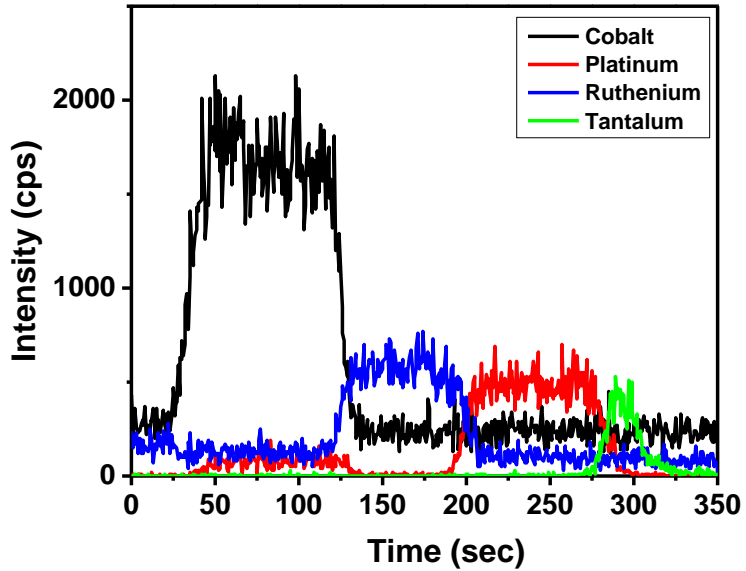


Figure 5-11: Secondary Ion Mass Spectroscopy of film stack

Table 5-4: Milling rates of selected materials

<b>Material</b>	<b>Rate of ion-milling</b>
Co (CoCrPt)	13 nm/min
Ru	12 nm/min
Pt	21 nm/min
Ta	8.5 nm/min
am-C	3.5 nm/min

The ion-milling process optimization was done on a case-by-case basis, and the details are provided in the relevant sections in the subsequent chapters.

## **5.7. Summary**

A brief introduction and processing details for the several steps in the process flow were discussed in this chapter. Typical spin-coating, solvent annealing and etching recipes were specified, while changes are noted in relevant sections in the upcoming chapters.

## CHAPTER 6

# Template Layer Development for PMR Media

### 6.1. Introduction

In this chapter, we discuss the magnetic and microstructural properties of templated media based on CoPt-SiO<sub>2</sub>. The polymer PSD3 (13.9 kg/mol,  $f_{\text{PDMS}} = 17.2\%$ , refer Table 4-1) was used to pattern an array of PDMS spheres with a center-to-center distance of approximately 17 nm. The pattern was subsequently transferred into an amorphous carbon hard mask using RIE as described in chapter 5. Ion-milling was then used to pattern the dome-morphology into different template layers. In the following sections, we discuss the various material choices for the template layer and compare the magnetic properties of the templated media in each case. The best choice for the template layer is then identified and further structural and microstructural characterization is done.

### 6.2. Remarks on the CoPt-SiO<sub>2</sub> Sputtering Process

A CoPt-SiO<sub>2</sub> composite target (Co target modified with SiO<sub>2</sub> and Pt chips) was used in the following study. The films were sputtered in the Z400#1 sputtering system at room temperature using a recipe of 100W RF and 45 mT Ar pressure at a rate of approximately 10 nm/min (unless otherwise specified). The high Ar pressure was used to enable columnar growth. In order to estimate the volume fraction of SiO<sub>2</sub> in the sputtered film, a 200 nm thick film was deposited onto an alumina substrate and Energy Dispersive X-Ray Spectroscopy (EDS) was used to determine the composition (atomic percentage) of Co, Pt and Si in the film. The density of CoPt was

estimated using the calculated mass (based on the atomic percentages from EDS) and the calculated volume (based on the lattice parameters obtained using XRD), and was found to be approximately 15.82 gm/cc. For amorphous SiO<sub>2</sub>, the reported value of density of amorphous SiO<sub>2</sub> (2.65 gm/cc) was used. Assuming that all of the Si exists in the film as SiO<sub>2</sub>, the volume fraction of SiO<sub>2</sub> can thus be calculated. Using this method, the composition of the target was found to be Co<sub>0.74</sub>Pt<sub>0.26</sub> (where the subscripts denote the atomic fractions of Co and Pt in CoPt), with 11.5 volume % of SiO<sub>2</sub>.

### **6.3. CoCrPt Thin Film as Template Layer**

The first choice for a template layer was a 5 nm thin film of a CoCrPt alloy with 66 atomic % Co, 15% Cr and 19% Pt (estimated using EDS). The advantage of using domes of a magnetic material such as CoCrPt to template the growth of the magnetic media is that, even if the aspect ratio of the domes required to cause templated growth is high, there will be no non-magnetic part in the magnetic grain. At a pitch of approximately 17 nm, pattern transfer using ion-milling into thick CoCrPt films is challenging, and so, the CoCrPt thickness was chosen to be 5nm. If the milling does not separate the magnetic domes in the template, the resulting template will have a continuous, exchange coupled CoCrPt layer underneath the CoPt-SiO<sub>2</sub> magnetic media grains, which will be unsuitable for recording.

#### **a. Setting up the Film Stack**

The initial film stack consisted of Ta (3nm)/Ru (25nm)/CoCrPt (5nm) and C (20nm). All the films were sputtered in sputtering system #4. The Ru layer underneath the CoCrPt facilitates the HCP (00.2) crystallographic texture of the CoCrPt layer. The texture of the Ru layer strongly depends on the sputtering conditions used for the Ta adhesion layer. Figure 6-1 shows the out-of-plane XRD patterns for 25nm Ru films sputtered on the Ta adhesion layer. The sputtering

conditions for the Ta are specified in the legend, and the sputtering power of the Ru was varied. The indexed peaks in the XRD pattern indicate that the Ru grains are randomly oriented, and although the (00.2) peak is stronger than the others, it is not suitable for CoCrPt growth.

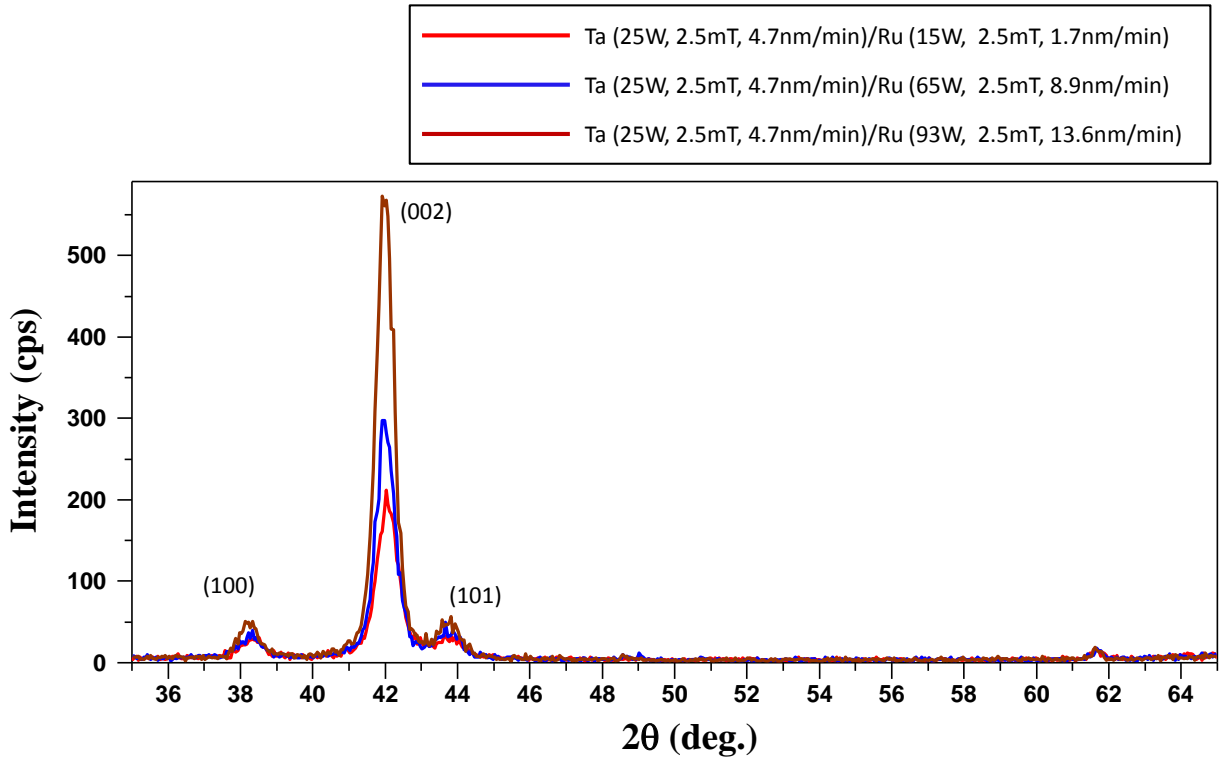


Figure 6-1: Out-of-plane XRD patterns showing the effect of sputtering power for Ru on its crystallographic texture

Figure 6-2(a) shows the XRD patterns illustrating the effect of Ta sputtering power on the Ru texture. The Ru (00.2) peaks have been normalized. We see that with increasing Ta sputtering power (which in turn implies increased sputtering rate), the (10.0) and (10.1) peaks of the Ru film sputtered on the Ta are suppressed. Rocking curves of the Ru (00.2) peak, shown in Figure 6-2(b), further illustrate the improvement in texture with increasing Ta sputtering power. Further

improvement in the rocking angle of the Ru (00.2) layer can be achieved using NiW or Pt (111) intermediate layers.

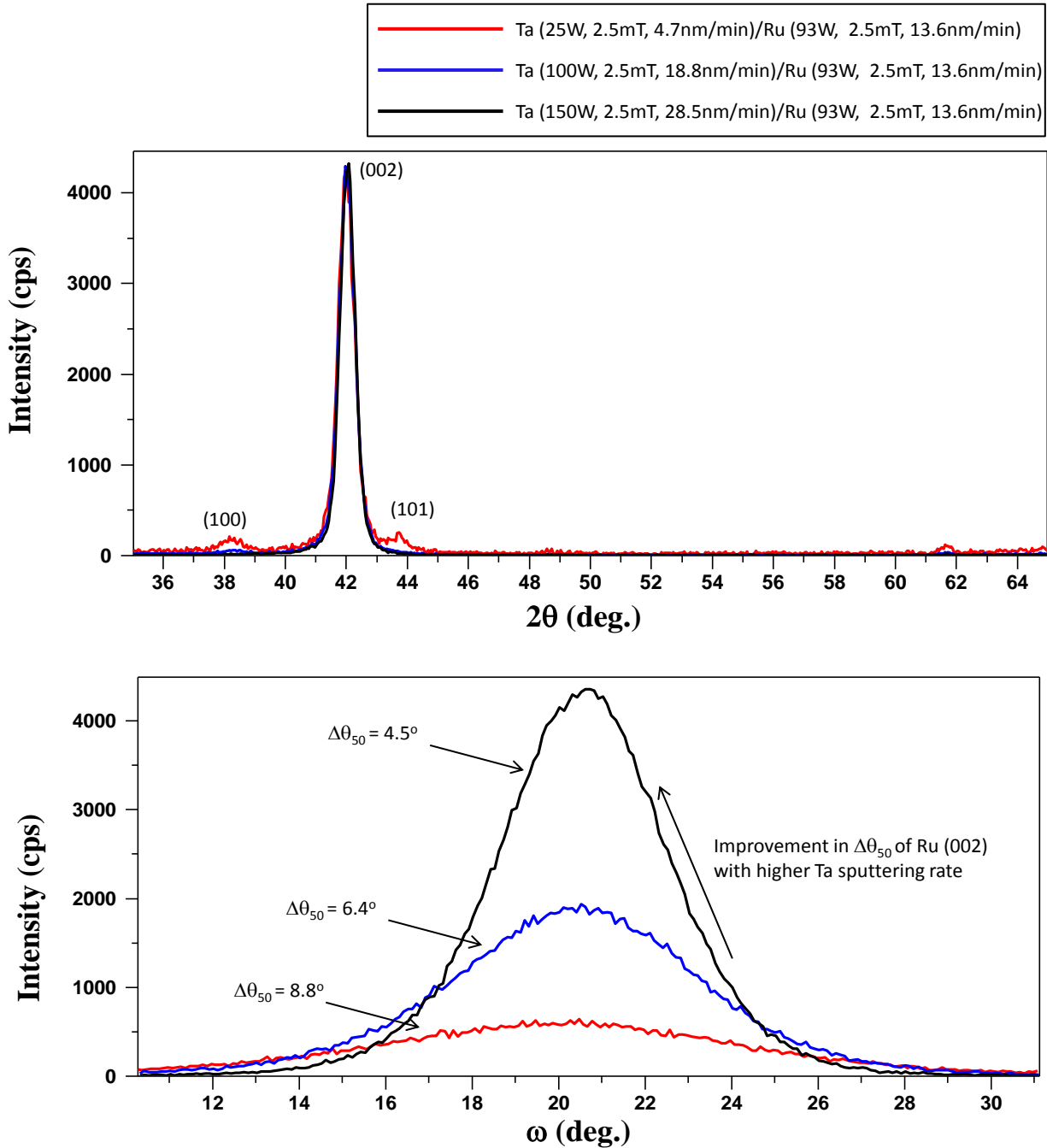


Figure 6-2: (a) Out-of-plane XRD patterns showing the effect of Ta sputtering power on the crystallographic texture of subsequently deposited Ru layer (b) Improvement in the FWHM of the rocking curve for Ru (00.2) peak with higher Ta sputtering power

When 5 nm of CoCrPt is sputtered onto the Ru layer, the peak intensity of the CoCrPt is too low, and due to the proximity in positions of the Ru and CoCrPt (00.2) peaks, it is not discernible in XRD. (00.2) texture of CoCrPt can be inferred from the out-of-plane magnetic hysteresis loop shown in Figure 6-3.

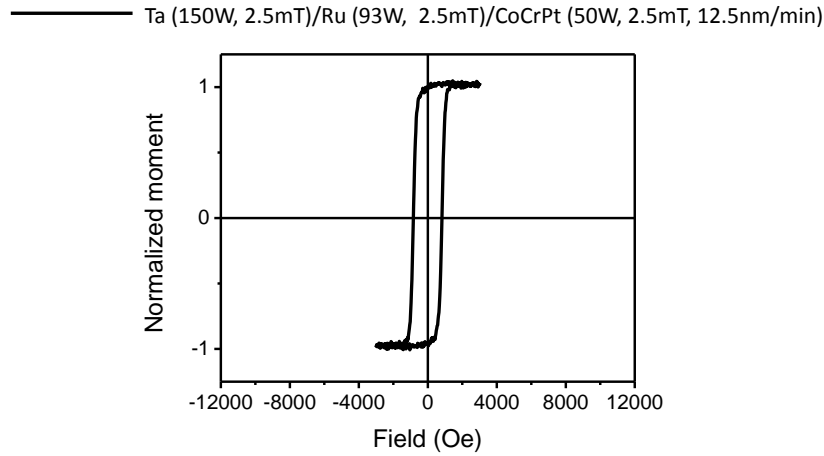


Figure 6-3: Out-of-plane magnetic hysteresis loop for a 5nm CoCrPt thin film

The optimized sputtering conditions for the film stack are summarized below in Table 6-1.

Table 6-1: Optimized sputter conditions for Ta/Ru/CoCrPt/C film stack

Layer	Machine	Power	Pressure	Rate	Thickness
Ta	#4	150W (DC)	2.5mT Ar	24 nm/min	4 nm
Ru	#4	93W (DC)	2.5mT Ar	13.7 nm/min	25 nm
CoCrPt	#4	50W (DC)	2.5mT Ar	12.3 nm/min	5 nm
Am-C	#4	150W (DC)	5mT Ar	2.16 nm/min	20 nm

## **b. Block Copolymer Fabrication and Pattern Transfer**

Spin-coating the PSD3 block copolymer, solvent annealing and etching into the carbon hard mask were performed as described previously. The samples were ion-milled for 20 and 30 seconds. During ion-milling the substrate normal was maintained at an angle of  $12.5^\circ$  w.r.t the ion beam. Since the template layer here is magnetic, the AGM was used to study the magnetic properties of these CoCrPt domes. Figure 6-4 shows the plane-view SEM images and magnetic hysteresis loops of the samples after milling for 20 and 30 seconds. After pattern transfer using RIE, the PDMS sphere size is  $\sim 10$ - $12$  nm, and post ion milling, this has increased to  $\sim 14$  nm. A cross-sectional view will help understand the morphology after the milling process, and this is discussed shortly. From the magnetic hysteresis loops, we see that the coercivity of the CoCrPt sheet film prior to milling is low, and the  $M_r/M_s = 1$ . Since the CoCrPt is a continuous film with no segregant, the magnetic grains are exchange coupled, and the low coercivity is not surprising. The  $M_r/M_s$  indicates that the film has good HCP (00.2) texture with the magnetic easy axis perpendicular to the plane of the film. On milling for 20 and 30 seconds however, we see that the coercivity and the  $M_r/M_s$  of the sample are sharply reduced. One reason for this could be the presence of a thin beam-damaged CoCrPt layer on top with ‘soft’ magnetic behavior. Another possibility is that the magnetic volume after milling is close to the superparamagnetic regime.

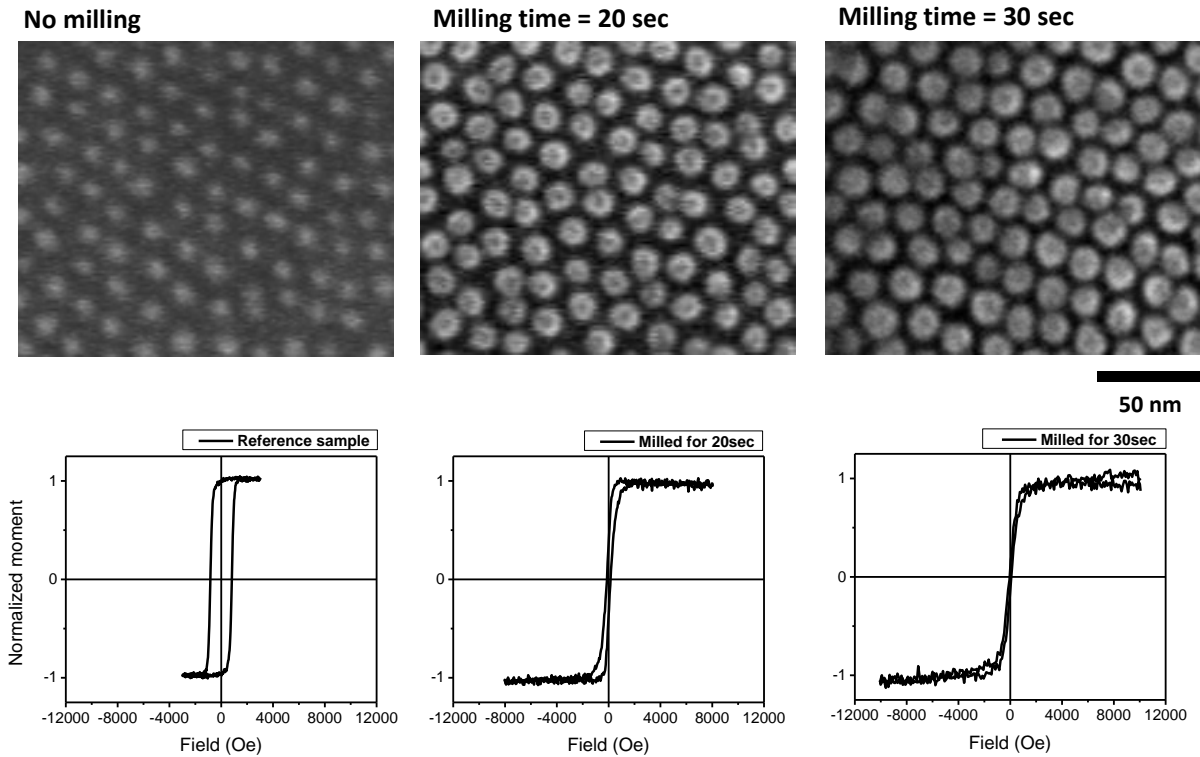


Figure 6-4: SEM micrographs and out-of-plane magnetic hysteresis loops for CoCrPt milled for 0-30 seconds

Cross-section Transmission Electron Microscopy was performed using the Tecnai TEM. Figure 6-5 shows the three cross-section micrographs of the un-milled, 20 sec milled, and 30 sec milled samples. These were scaled and stacked using the amorphous Ta layer at the bottom of the film stack. From these TEM micrographs, we can see the dome-morphology of the patterned CoCrPt layer. In the first image, we see the unpatterned CoCrPt sheet film. After 20 seconds of ion-milling, it appears that the milling front (from the top) has reached the Ru layer, giving domes of CoCrPt. On 30 seconds of milling, the milling front has moved further down, and from the stacking of these TEM images, we see that not much CoCrPt is left. Since the lattice parameters of CoCrPt and Ru in the (00.2) planes are similar, it is difficult to pinpoint the location of the CoCrPt/Ru interface. Also, it is difficult to discern if the amorphous carbon mask is still remaining

because of its electron transparent nature. Approximating these domes as the segments of a sphere, the volume of each dome can be written as  $V = \frac{\pi h}{6}(3a^2 + h^2)$ , where ‘h’ is the height of the segment (considered to be 3 nm) and ‘a’ is the bottom radius of the segment (considered as 5 nm), which gives  $V \sim 130 \text{ nm}^3$ . Since the milling front is now in the Ru layer, the volume of the CoCrPt part of the dome is thus less than  $130 \text{ nm}^3$ , which is close to the superparamagnetic regime, which explains the lowering of coercivity and low  $M_r/M_s$  in the hysteresis loops. We proceeded with the templating process-flow to see what effect this would have on the sputtered CoPt-SiO<sub>2</sub> magnetic media.

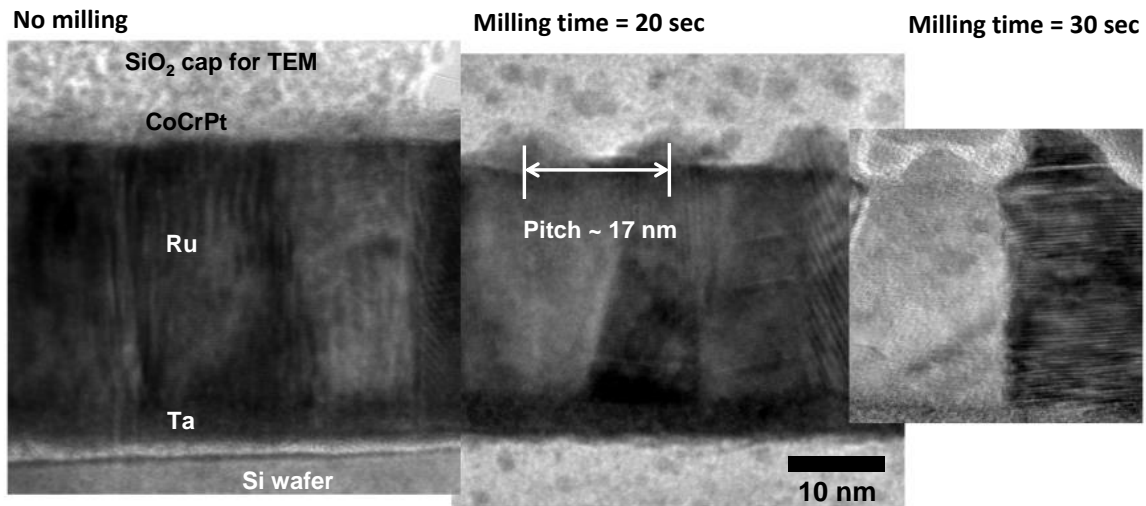


Figure 6-5: Cross-section bright-field TEM micrographs showing the evolution of dome-morphology in CoCrPt on ion-milling for 0-30 seconds

### c. Media Deposition Results and Discussion

Since the sample is exposed to atmosphere after the ion-milling, a short sputter-etch has to be performed in the sputtering machine prior to the sputtering of the CoPt-SiO<sub>2</sub>. However, the sputter-

etch is essentially just a milling process, and will damage the morphology of the domes. Also, since the Ar beam during the sputter-etch is perpendicular to the plane of the substrate, redeposition may occur, and a fresh surface may not really be generated. Another issue with the sputter-etching process in the Z400#1 system is that the matching networks are not quite reliable during the sputter-etching process, and work for very few sputter-etch conditions. Based on this, a 50W RF Ar plasma at 15 mT pressure was selected for the sputter-etching process. The previously milled samples were sputter-etched for 6 and 9 seconds, and without breaking vacuum, a 15 nm media layer of CoPt-SiO<sub>2</sub> was deposited also by RF sputtering, with a power of 100W, at 45 mT Ar pressure. AGM was then used to study the out-of-plane and in-plane magnetic hysteresis loops of these templated media samples, and are shown in Figure 6-6.

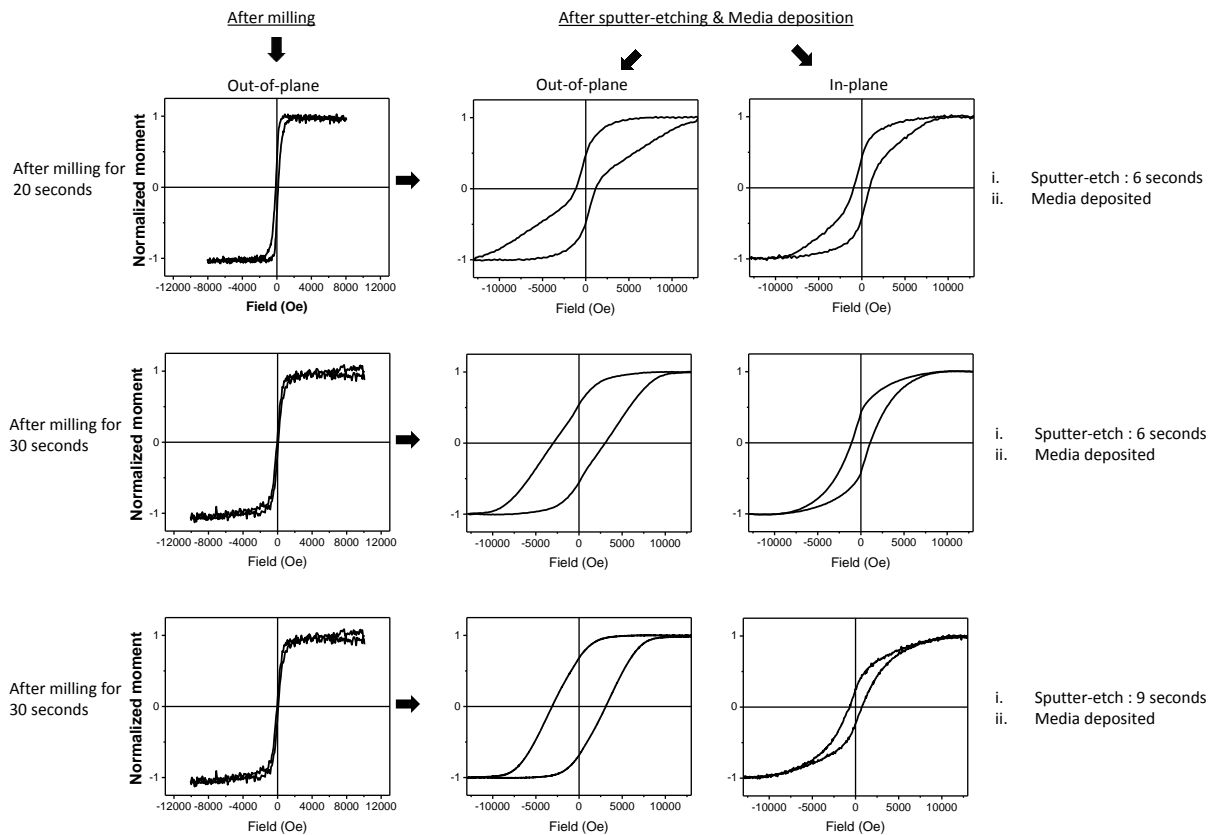


Figure 6-6: Out-of-plane and in-plane magnetic hysteresis loops from the various attempts at templated media growth using CoCrPt template layer

From the out-of-plane (OP) magnetic hysteresis loop for the first case shown above, we see that there appears to be a magnetically soft region that brings the coercivity down. As discussed earlier, this could be the effect of the magnetically ‘soft’ CoCrPt domes remaining after ion-milling in the template. In the next two cases, where milling was done for 30 seconds, the soft region is no longer present, but the coercivity ( $\sim 2500$  Oe) and remnant magnetization ( $\sim 0.6 M_s$ ) are low. Here, the CoCrPt has likely been milled away during the sputter-etch step. Thus, even if these domes template the growth of magnetic media as we require, the poor magnetic properties of these domes will influence the magnetic grains, acting as sites where switching starts, and lowering the switching field of the media, which is not a desirable effect. CoCrPt is thus not a suitable material for the design of the template layer. For the next study, we used Ruthenium (Ru) as the template layer material.

## **6.4. Ru Thin Film as Template Layer**

In chapter 1, we discussed the benefits of Ru as the underlayer of choice for PMR media, due to its close lattice matching with CoCrPt alloys. It therefore can also function as a suitable template layer.

### **a. Template Fabrication Details**

The initial film stack consisted of Ta (3nm)/Ru (25nm) and was sputtered in machine #4 using the conditions previously specified in Table 6-1. The subsequent process steps are also similar to the previously described case.

### **b. Media Deposition Results and Discussion**

Once the ion-milling was completed, the sample was sputter-etched for 6 seconds (50W RF, 16.5mT Ar) prior to the deposition of 15 nm of CoPt-SiO<sub>2</sub> magnetic media (100W RF, 45mT Ar).

Magnetic hysteresis loops of these templated media samples are shown in Figure 6-7. In order to understand the effects of templating, a reference sample was made without any patterning. However, in order to emulate the effects of the patterning process, all the steps except for the block copolymer patterning were performed on this sample. This was done particularly to understand the effects of sputter-etching.

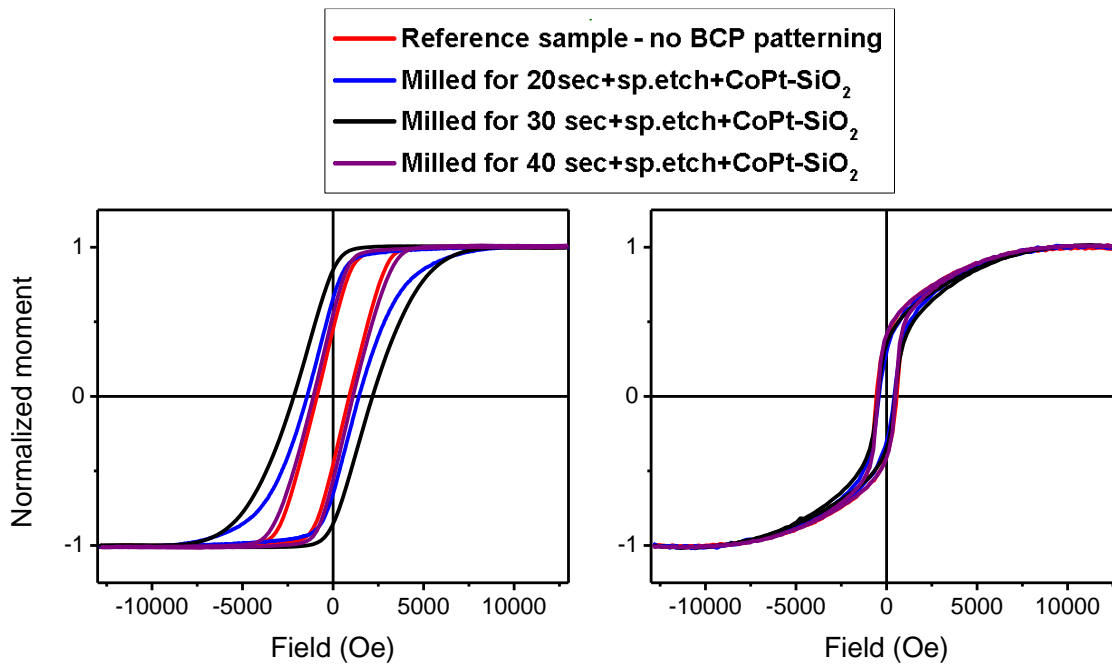


Figure 6-7: Out-of-plane and in-plane magnetic hysteresis loops for templated CoPt-SiO<sub>2</sub> media on Ru templates milled for 0-40 seconds

The first thing to note in the out-of-plane hysteresis loops is the poor  $M_r/M_s$  of the reference sample, a consequence of the sputter-etching of the Ru film prior to the deposition of CoPt-SiO<sub>2</sub>. On fabricating the dome morphology of Ru, the coercivity of the media increases, and is the highest for 30 sec milled sample. For  $t_{\text{mill}} = 40$  sec, the coercivity again becomes similar to the reference sample, indicating that the template morphology is no longer present. Once the amorphous carbon hard mask is eroded away in the milling process, there is no longer any selectivity in milling, so

the dome-morphology will eventually flatten out since ion-milling is a line-of-sight process. The in-plane hysteresis loops in all four cases are quite similar. Since the saturation field in the in-plane loop is a measure of the anisotropy field of the film, we can say that all these samples have similar anisotropy fields, which indicate that the improvement in the out-of-plane hysteresis loops at  $t_{\text{mill}} = 30$  seconds must be due to microstructural effects such as better segregation of the CoPt and SiO<sub>2</sub>. To further improve the magnetic properties, we tested various sputter-etching conditions on sheet Ru films to find the optimum conditions. The results are summarized in the plot below (Figure 6-8) of  $M_r/M_s$  of the media film vs sputter-etching time for different sputtering conditions of magnetic media.

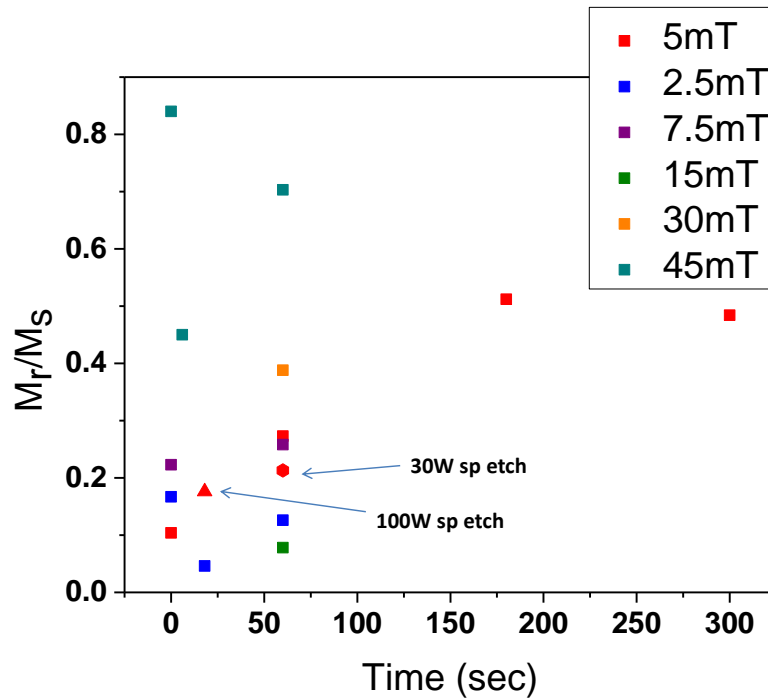


Figure 6-8: Summary of sputter-etching attempts

Ideally, after sputter-etching, the  $M_r/M_s$  of the film should be 1 if the texture is good, and if there are no defects causing premature switching of the magnetization. As seen from the figure, none of the sputter-etching conditions resulted in good magnetic properties. This was the case for sputter-etching for different times, at different conditions as well as different deposition conditions of the magnetic media. Further, the dome morphology patterned into the Ru layer by ion-milling is stable only for 6-9 seconds, as seen from the SEM micrographs shown below in Figure 6-9. After this time, the damage to the domes is evident.

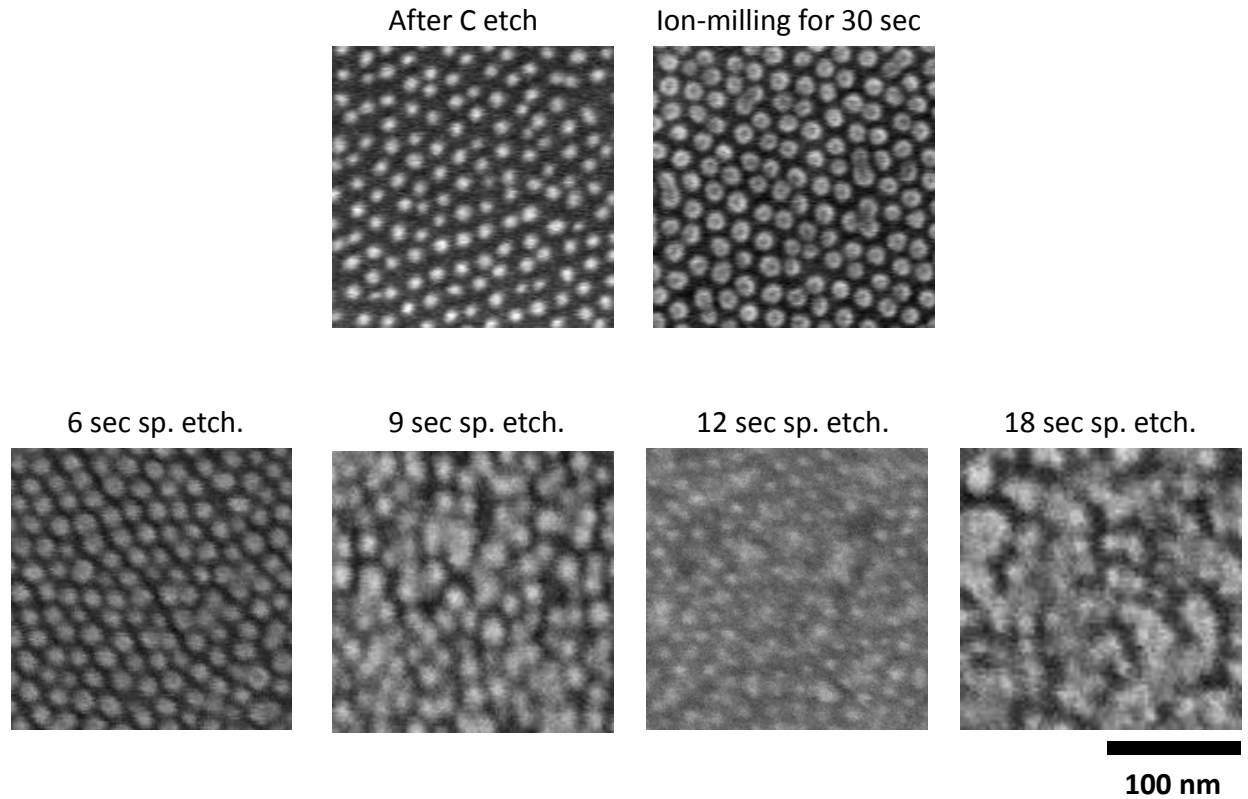


Figure 6-9: Plane-view SEM micrographs showing effect of sputter-etching

It is evident from the above tests that sputter-etching quickly damages the dome-morphology of the Ru underlayer. We also see from the sheet-film tests that sputter-etching of the underlayer

results in poor magnetic properties of the magnetic media, which is likely due to damage to the underlayer surface, and the subsequent poor texture of the media. We thus need to develop a process that avoids sputter-etching completely, and is yet able to template the growth of magnetic media, with good texture and magnetic properties. The design of a Platinum (Pt) template layer is a key step in this direction.

## 6.5. Pt Thin Film as Template Layer

### a. Advantage of using Pt

Platinum is a transition metal with an FCC crystal structure (space group:  $P\frac{4}{m}\bar{3}\frac{2}{m}$ ). It is one of the least reactive metals, and does not oxidize at room temperature. Table 6-2 below tabulates the Gibbs free energy for the oxidation reactions at room temperature for the various metals used here, generated using the software package FactWeb (a part of FactSage, a database of thermodynamic properties[84]). A negative free energy of mixing indicates that the reaction is spontaneous and vice-versa. We see that Pt has a positive  $\Delta G_{\text{reaction}}$  at room temperature, showing that it does not oxidize at room temperature.

Table 6-2: Gibbs free energy of oxidation reactions at room temp.

Element – Oxide	Reaction	$\Delta G_{\text{reaction}}$ at 298.15K
Co (CoO)	$Co(s) + \frac{1}{2}O_2(g) \rightarrow CoO(s)$	-214 kJ
Co (Co <sub>3</sub> O <sub>4</sub> )	$3Co(s) + 2O_2(g) \rightarrow Co_3O_4(s)$	-794.96 kJ
Ru (RuO <sub>2</sub> )	$Ru(s) + O_2(g) \rightarrow RuO_2(s)$	-253.04 kJ
Pt (PtO <sub>2</sub> )	$Pt(s) + O_2(g) \rightarrow PtO_2(s)$	165.88 kJ

### b. Sheet-Film Test of Modified Approach

In order to establish if exposure of Ru to atmosphere (as was the case in the previous attempts) or lack of exposure (current attempt) influences the magnetic properties of the CoPt-SiO<sub>2</sub> media, we devised the following test. In the first case, 3 nm Ta/25 nm of Ru was sputtered onto a single-crystal Si substrate using sputtering machine #4. The sputtering conditions used were the ones optimized from the previous studies (Table 6-1). Then, 10 nm of CoPt-SiO<sub>2</sub> was deposited onto the film stack using a 100W RF plasma at 45 mT Ar pressure, in the sputtering system Z400#1. Since two different systems were used, the sample was exposed to atmospheric conditions after the sputtering of the Ru layer (Sample I). For the other case, 3 nm Ta/10 nm Pt was sputtered onto the silicon substrate using sputtering machine #3 (Sample II). For Pt, DC sputtering was used (25W, 2.5mT, 7.8nm/min). Then, 5 nm of Ru and 10 nm of CoPt-SiO<sub>2</sub> were sputter-deposited in Z400#1. In this case, the break in vacuum is after the deposition of the Pt layer, which will be the case for the patterned samples as well. The AGM was used to study the out-of-plane magnetic hysteresis loops, which are shown in Figure 6-10.

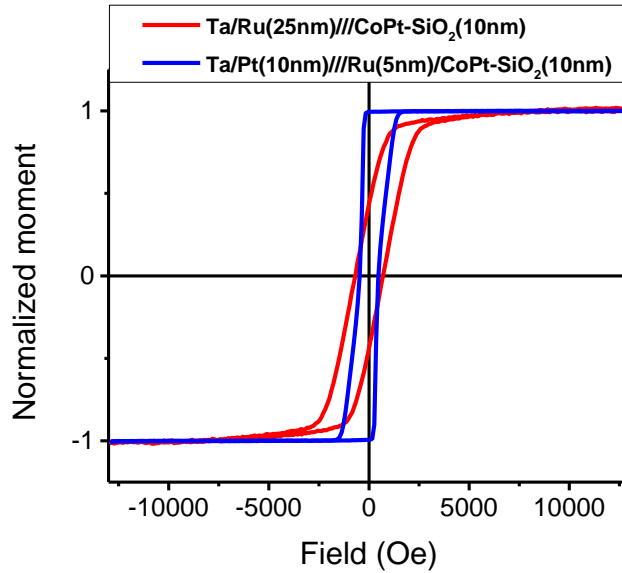


Figure 6-10: Out-of-plane magnetic hysteresis loops for untemplated magnetic media deposited on Ru underlayer exposed to atmosphere (red), not exposed to atmosphere (blue)

From the out-of-plane hysteresis loops, we see that sample II has  $M_r/M_s = 1$ , whereas sample I has a poor remanence. This study indicates that Sample II, where the Ru and CoPt-SiO<sub>2</sub> were sputtered without a break in vacuum, has better magnetic properties, as compared to sample I where the vacuum is broken between the two sputtering steps. This supports our hypothesis that the use of a Pt template layer which facilitates the above process is a good direction for attempting templated magnetic media. It is important to note that the magnetic properties of sample II are better than Sample I, but are not suitable for magnetic recording as it is. The coercivity of the magnetic film is quite poor, and the magnetic grains are exchange coupled, as indicated by the sudden drop in magnetization as soon as the nucleation field is reached. Sample II is used as a control sample for the magnetic properties obtained under these sputtering conditions and Ru thickness, when the magnetic grain growth is not templated using the block copolymer self-assembly process.

### c. Modified Process Flow

Platinum also has a high milling rate of 21 nm/min (see Figure 5-11), and the dome-morphology can easily be patterned into the Pt template layer using ion-milling as described in the earlier sections, exploiting the difference in milling rates between am-C and Pt. The modified process flow for template fabrication and media growth using Pt is shown in Figure 6-11.

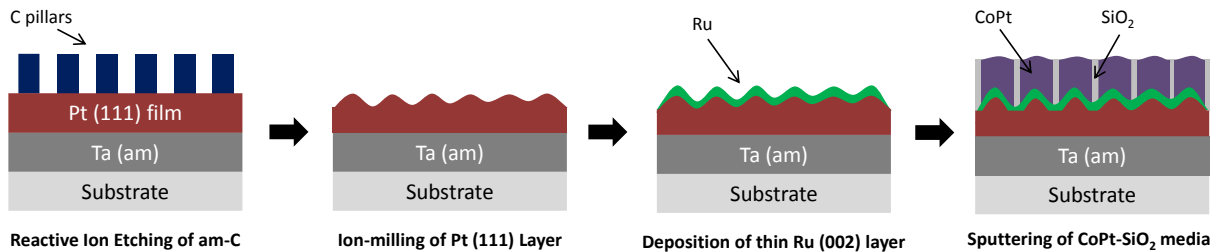


Figure 6-11: Modified process flow for template fabrication using Pt

The process flow is similar to the previous case, with the additional step of sputtering a thin Ru layer after patterning the dome morphology of Pt. When CoPt is sputtered directly onto Pt (111) textured film, it starts to grow with the FCC (111) texture, which does not possess uniaxial anisotropy and is thus not suitable for magnetic media. However, the lattice mismatch along the close-packed direction of Ru (00.2) and Pt (111) is only 2.5% (Figure 6-12), and so a thin Ru layer can be used to obtain the desired (00.2) texture of the CoPt. Pt naturally grows with the (111) crystallographic texture when sputtered onto a Ta adhesion layer, and can subsequently be used as a suitable underlayer for the epitaxial growth of Ru with the (00.2) texture.

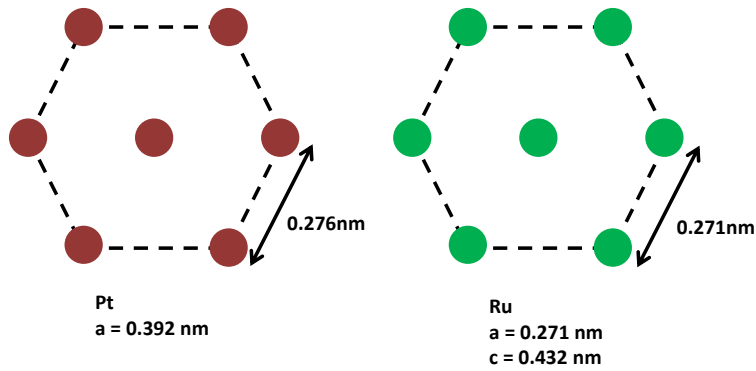


Figure 6-12: Schematic of the lattice mismatch in the close-packed plane of FCC Pt (111) and HCP Ru (0002)

Figure 6-13 shows out-of-plane XRD pattern of a 15 nm Pt film deposited on the Ta adhesion layer. The peak at  $2\theta = 39.5$  corresponds to Pt (111). The BCP fabrication and pattern transfer were then performed as outlined and discussed in the process flow (Figure 6-11). The sample with the patterned dome-shaped morphology of Pt was then used as the template. The milling time was varied between 20 and 30 seconds.

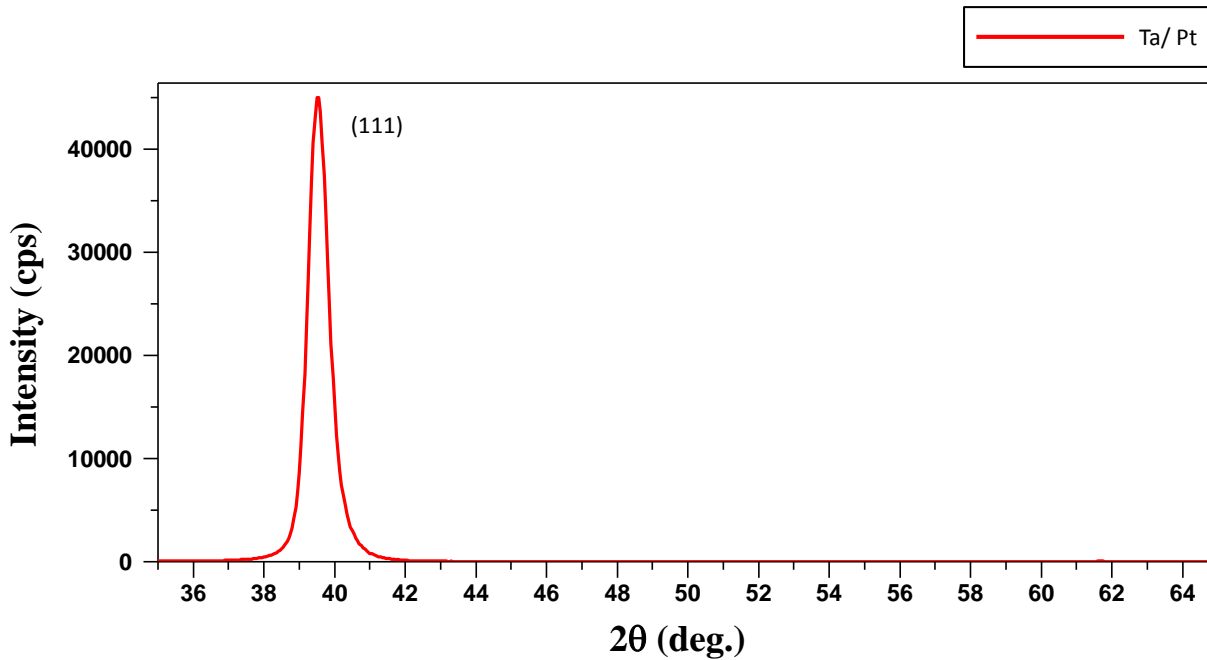


Figure 6-13: Out-of-Plane XRD pattern of a Pt thin film deposited on Ta showing FCC (111) texture

As discussed earlier, the next step in the process is the sputtering of the Ru and CoPt-SiO<sub>2</sub> layers. The sputtering conditions for the Ru were picked to obtain a conformal coating over the patterned Pt domes, with sufficient texture to enable good c-axis orientation of the CoPt-SiO<sub>2</sub> layer. Thus, an Ar sputtering pressure of 5mT was utilized. In order to determine the minimum Ru thickness that is required, CoPt-SiO<sub>2</sub> (100W RF, 10nm, 45mT, 10nm/min) was sputtered onto sheet film Ru layers of varying thicknesses. The layers underneath the Ru were Ta (3nm) /Pt (15nm). As we see from the out-of-plane magnetic hysteresis loops shown in Figure 6-14(a), thickness of above 2.4 nm of Ru seems sufficient for obtaining perpendicular magnetization of the CoPt-SiO<sub>2</sub> layer. From the in-plane hysteresis loops (Figure 6-14(b)), we also see that for thicknesses above 2.4 nm, the saturation field for the CoPt-SiO<sub>2</sub> is similar, indicating similar values for the anisotropy

coefficient. A thickness of 5 nm for the Ru was picked for the subsequent tests leaving sufficient margin.

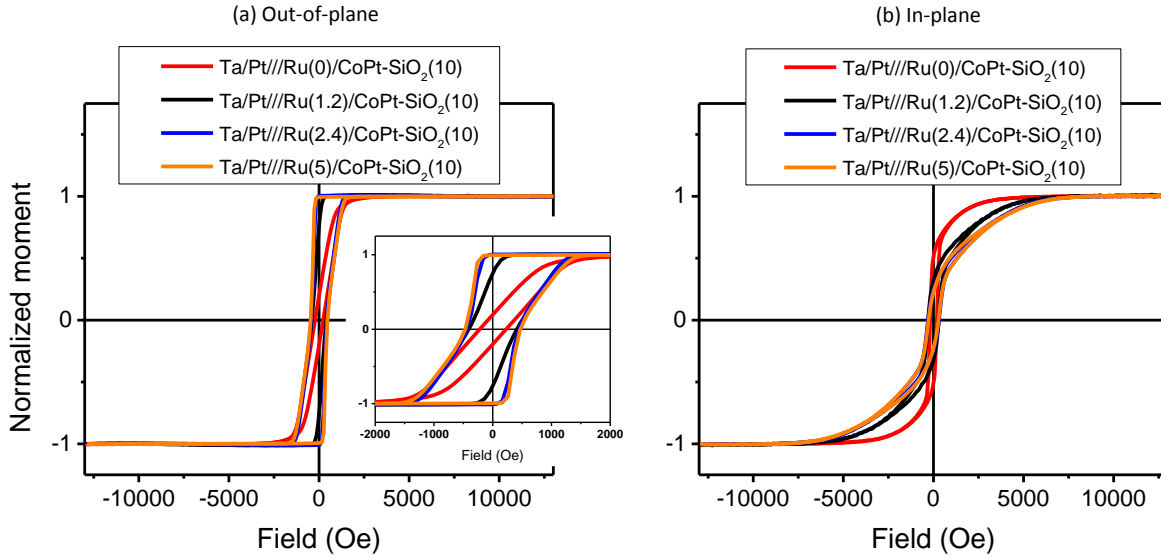


Figure 6-14: (a) Out-of-plane AGM loops (inset showing zoomed in area of interest) and (b) in-plane AGM loops for CoPt-SiO<sub>2</sub> sheet films with varying Ru underlayer thickness

#### d. Media Deposition Results and Discussion

5 nm of Ru and 10 nm of CoPt-SiO<sub>2</sub> were sputter-deposited onto the patterned template without breaking vacuum as described earlier, and AGM was used to study the magnetic properties (shown in Figure 6-15). 25 seconds of ion-milling gives us the best magnetic properties in terms of coercivity (~ 5 kOe) and remnant magnetization (~ 0.83 M<sub>s</sub>).

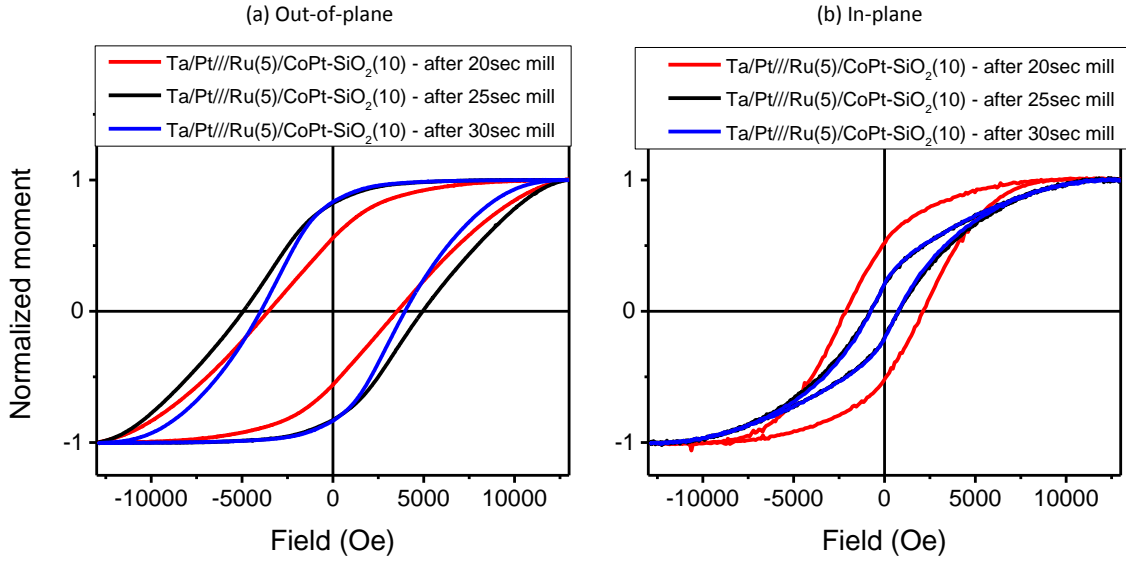


Figure 6-15: (a)Out-of-plane and (b) In-plane magnetic hysteresis loops for templated media using Pt template layer with different milling times

The coercivity of the templated media obtained using the Pt template layer (~ 5 kOe) is much higher than that obtained using the Ru or CoCrPt as the template layers (~ 2.2 kOe). Sputtering of the CoPt-SiO<sub>2</sub> over a fresh Ru surface without any break in vacuum, and without any sputter-etching likely played an important role in the relative improvement in the magnetic properties.

Figure 6-16 compares the hysteresis loops of templated sample and an ‘un’templated reference sample. We see that the templated sample has a much higher coercivity, but there is also a lowering of the remnant magnetization. The higher coercivity can be attributed to better exchange decoupling between the magnetic grains as described earlier in our discussion of the film microstructure in chapter 1. In contrast, we see that the reference sample has a very low coercivity, which is due to higher exchange coupling between the CoPt grains. The low remnant magnetization could be due to poor (00.2) texture of the CoPt. The lowering of remnant magnetization may be due to regions in the sample where the BCP pattern was poorly defined, but

further investigation is necessary to confirm this. Poor (00.2) texture of the CoPt with wide rocking curve could be another possible reason. The templating process also seems to aid the improvement of the uniaxial anisotropy. The saturation field in the in-plane hysteresis loops is a good measure of the anisotropy field of the sample, which can be written as,  $H_k = H_s + N_d M_s$ , where  $H_k$  is the magnetic anisotropy field,  $H_s$  is the saturation field for in-plane measurement,  $N_d$  is the demagnetization factor, and  $M_s$  is the saturation magnetization of the material. Further, the uniaxial anisotropy constant can be subsequently estimated as  $K_u = \frac{M_s H_k}{2}$ . Assuming that  $N_d$  for both the templated and untemplated cases are  $4\pi$  since these are both magnetic thin films, we find that the templated CoPt film has a higher  $K_u$  of  $7.7 \times 10^6$  erg/cc (as compared to  $6.5 \times 10^6$  for the untemplated sample). This calculated value is an approximate one however, since the demagnetization factor  $N_d$  could change based on the media microstructure. On the other hand, the non-zero remnant magnetization in the in-plane curve indicates the presence of a small percentage of magnetic grains with in-plane orientation. As mentioned earlier, this could be the contribution from poorly patterned regions, but further investigation is necessary to confirm this.

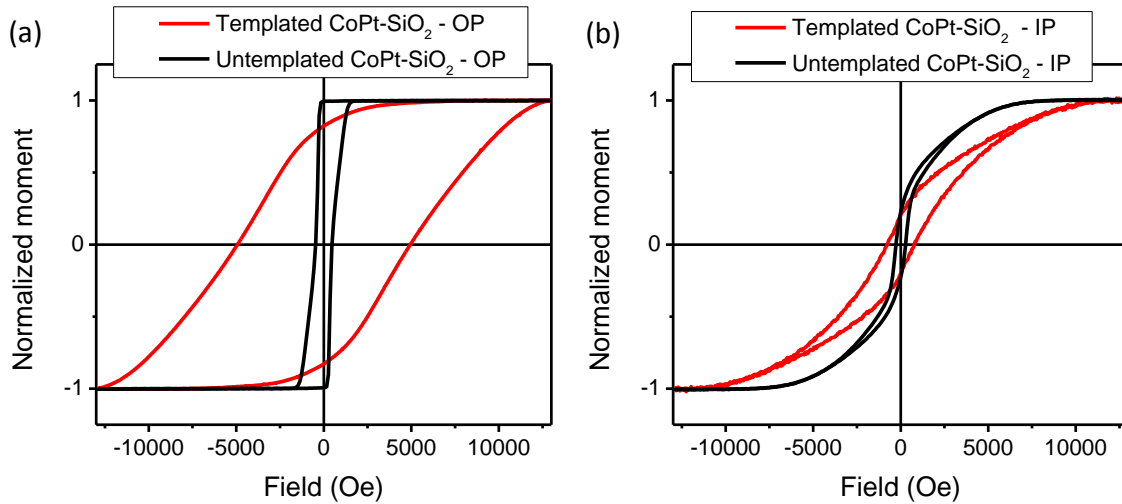


Figure 6-16: (a) Out-of-plane and (b) In-plane magnetic hysteresis loops for templated media using Pt template layer with different milling times

We attempted to improve the magnetic properties of the templated media by varying two parameters: the ion-milling angle for the Pt template fabrication, and the thickness of the Pt layer itself. In the first study, the Pt thickness was still maintained as 15 nm. Ion-milling angle was varied between 12.5° and 27.5°. In Figure 6-17 below, we see that the optimum ion-milling angle is 22.5°. For 27.5°, we see that the  $M_r$  does not change by much, however, the coercivity reduces, and the loop shape indicates that the exchange coupling between the CoPt grains is increasing. Increasing the Pt thickness from 15 to 30 nm resulted in an improvement in Pt (111) texture, which translated to an improvement in the magnetic properties of the media, as shown in Figure 6-18. We see that the improved Pt texture increases both the  $M_r$  and the  $H_c$  of the templated media.

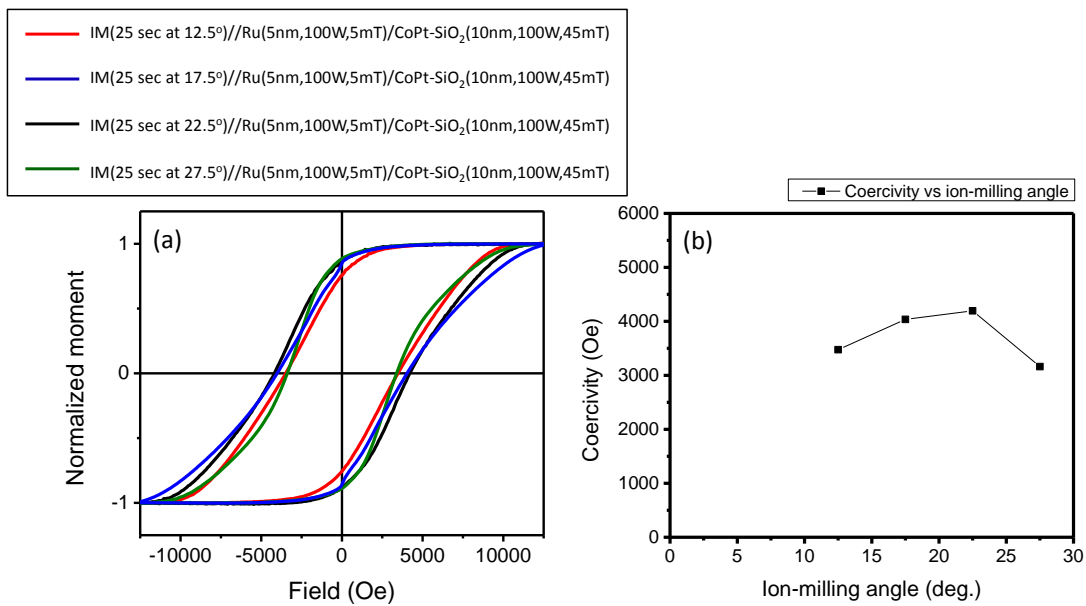


Figure 6-17: (a) Out-of-plane M-H loops illustrating effect of ion-milling angle of Pt layer on templated media  
(b) Coercivity vs ion-milling angle

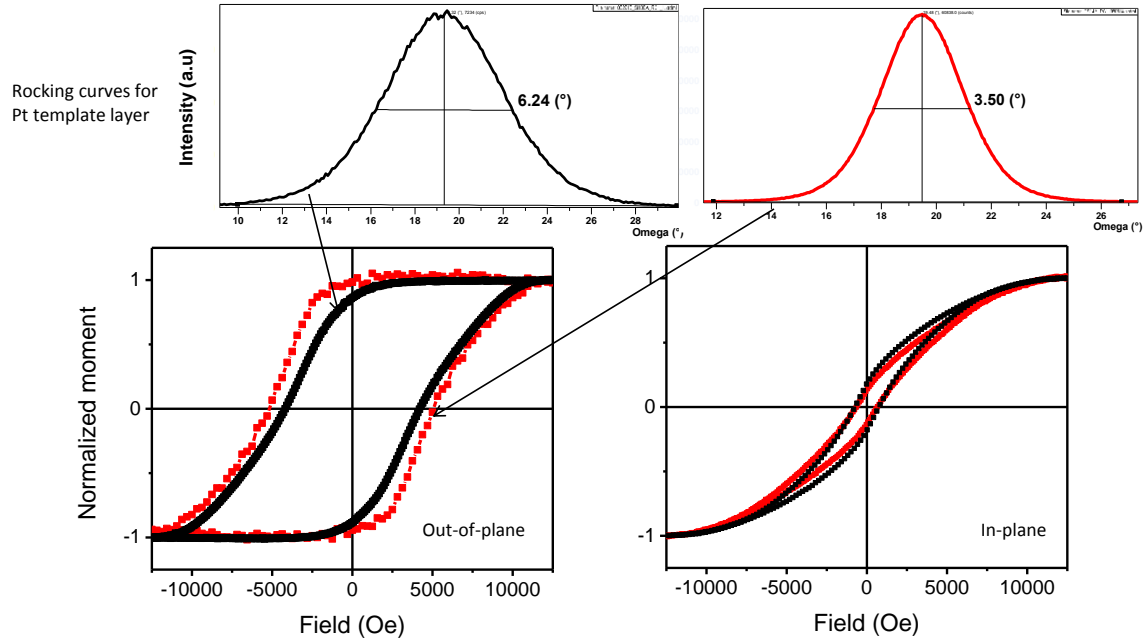


Figure 6-18: Out-of-plane and in-plane magnetic hysteresis loops illustrating the effect of Pt (111) rocking angle on templated media properties

Out-of-plane XRD of the samples after Ru deposition (blue) and after media deposition (red) onto the template is shown in Figure 6-19, along with the rocking curves of the various peaks. In the first case, we see that the Ru (00.2) peak ( $\sim 41.4^\circ$ ) manifests as a shoulder in the Pt (111) peak ( $\sim 39.6^\circ$ ) due to the low thickness of the Ru. The CoPt-SiO<sub>2</sub> peak and the Ru peak also nearly overlap, and thus on deposition of CoPt-SiO<sub>2</sub>, we see an increase in the peak around  $42.3^\circ$ , indicating (00.2) texture of the CoPt. In the rocking curves for the three peaks, we see that there is a slight worsening in the rocking angle as we go from the Pt (111) to the Ru (00.2) layers, while there is an improvement in the texture from the Ru to the CoPt (00.2) layer.

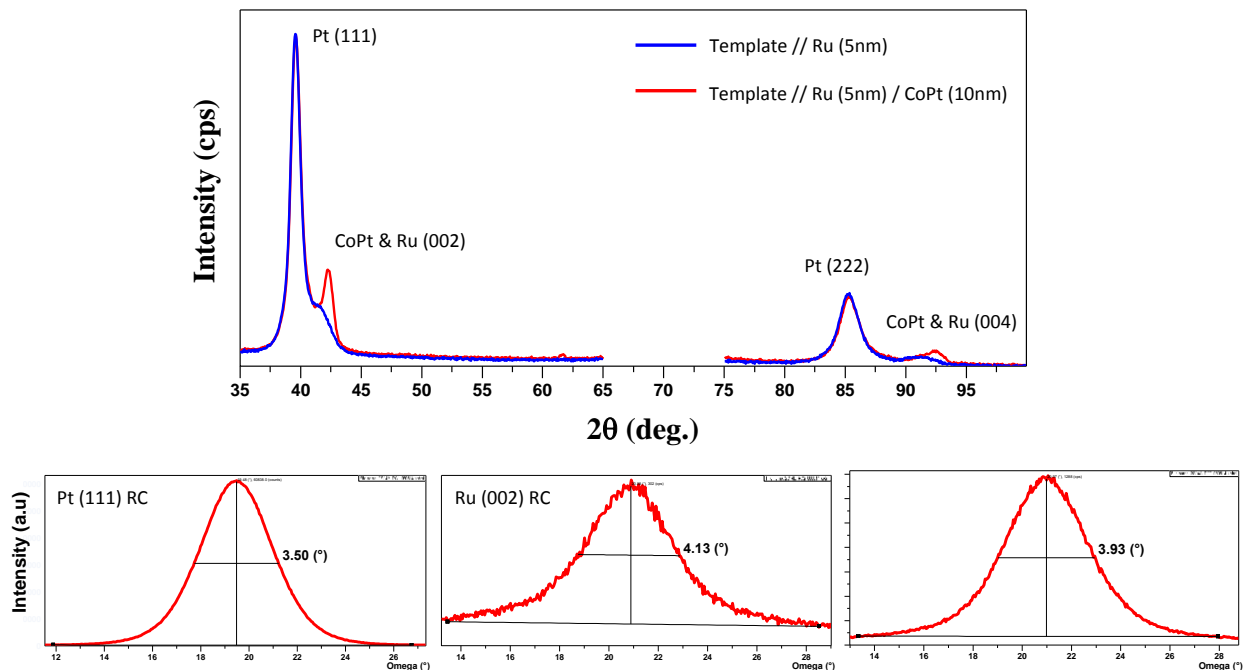


Figure 6-19: Out-of-plane XRD patterns for templated media before and after media deposition, and rocking curves for the Pt (111), Ru (00.2) and CoPt (00.2) peaks

The plane-view transmission electron micrograph for the templated magnetic media is shown in Figure 6-20, taken using a JEOL JEM-2000EX transmission electron microscope. From this bright field image, we observe the CoPt grains surrounded by the lighter-appearing amorphous SiO<sub>2</sub>. The average grain size of the CoPt grains is found to be 16.2 nm with a standard deviation of 11%. The grain size is thus defined by the center-to-center distance between the polymer spheres in the BCP pattern, which was earlier mentioned to be approximately 17 nm. The difference in these numbers is indicative of the thickness of the SiO<sub>2</sub> grain boundaries. The distribution in grain size is also approximately the same as the distribution in the center-to-center spacings in the polymer pattern. By improving the BCP patterning, these distributions can be further minimized, and this would translate to the magnetic media microstructure as a more uniform grain size. Figure 6-20(c) shows the microstructure of ‘untemplated’ media grown with the same sputtering conditions. Here, the

grain structure of the CoPt-SiO<sub>2</sub> is not quite well defined and the effect of the template on the media microstructure can be clearly discerned. Figure 6-21 shows the indexed plane-view electron diffraction pattern of the templated region. The presence of the (10.0), (11.0) and subsequent HCP CoPt reflections in the plane-view diffraction pattern confirms the perpendicular (00.2) texture of the CoPt grains.

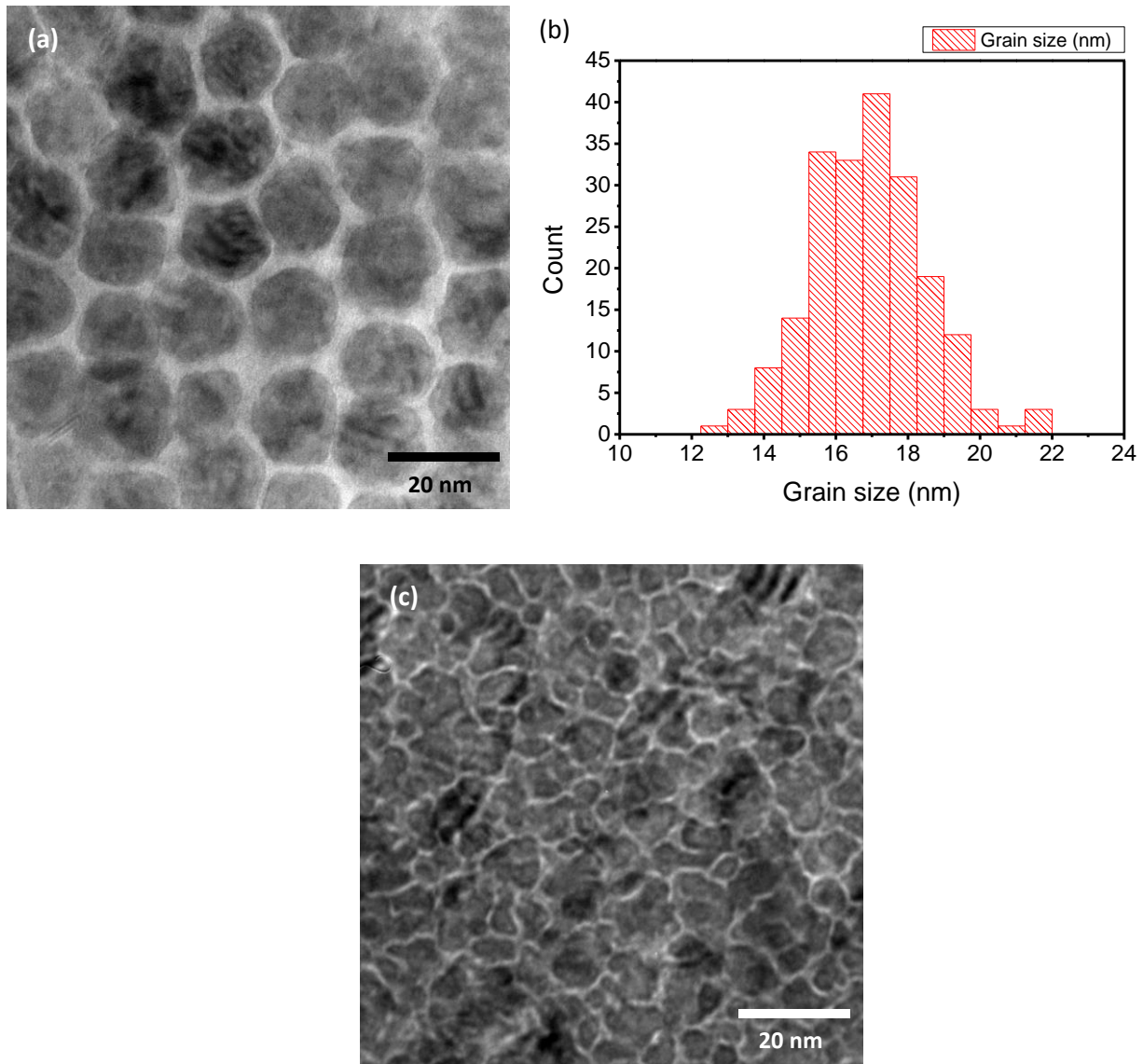


Figure 6-20: (a) Plane-view TEM micrograph of templated CoPt-SiO<sub>2</sub> media, (b) Grain size distribution and (c) TEM micrograph of 'untemplated' CoPt-SiO<sub>2</sub> media

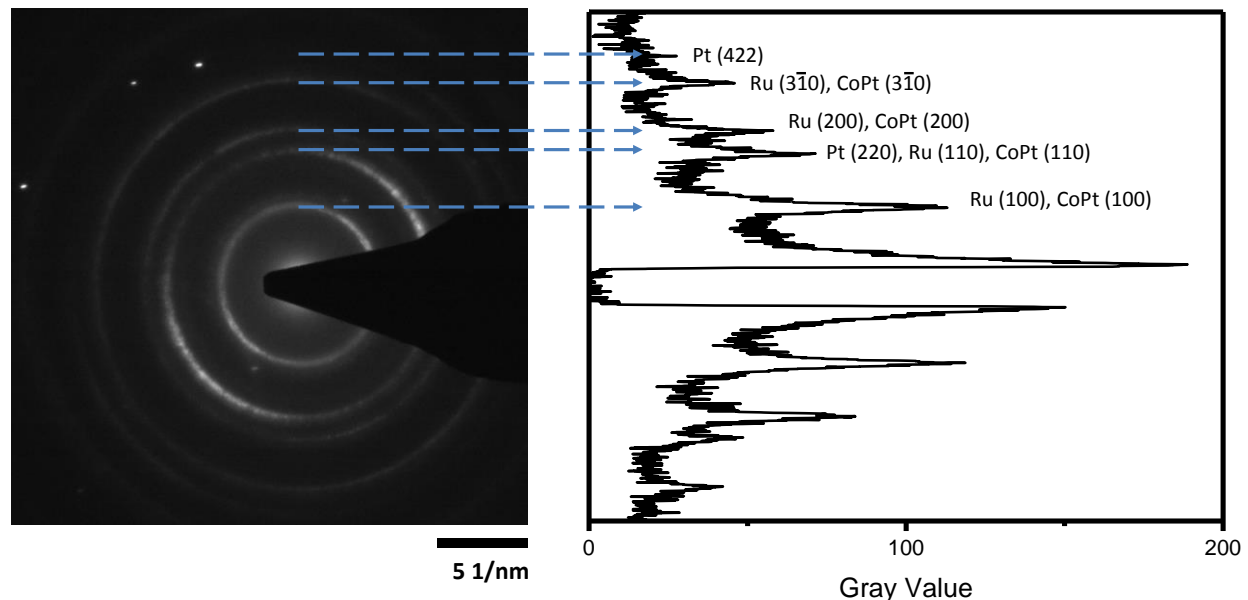


Figure 6-21: TEM diffraction pattern for the templated CoPt-SiO<sub>2</sub> media. Gray value plot shown is for a vertical line drawn through the center of the diffraction pattern

Scanning Transmission Electron Microscopy (STEM) was used to study the cross-section microstructure of the templated media in a Philips Tecnai F20 FEG TEM fitted with a high-angle annular dark field (HAADF) detector. The specimen was prepared using the FIB lift-out method as described in chapter 3. The specimen was first polished using a 30 kV focused Ga<sup>+</sup> beam at a current of 0.1 nA, and cleaned with a 10 kV ion beam at a current of 30 pA. The HAADF-STEM image is shown in Figure 6-22. In HAADF mode, the contrast observed is mostly due to atomic number or ‘Z’ contrast. Thus, as seen in the figure, Pt, which has the highest ‘Z’ among the materials in the sample, has the highest brightness. CoPt and Ru have similar contrast since the signal from Co and Pt gets averaged. SiO<sub>2</sub> appears the darkest, and it is evident from the image that it goes between the domes, while the CoPt grows on the top of the domes as defined by the

template. Further, the elemental distribution in one CoPt grain was mapped using Energy dispersive x-ray spectroscopy (EDS) using a FEI Titan 80-300 TEM. Drift-corrected EDS spectra were collected at each point with a beam dwell time of 2 seconds. By selecting suitable X-ray peaks for each element, maps were then generated, where the brightness at a point corresponds to that element's relative concentration at that point. In the maps, we see the Pt domes demarcated clearly, with a continuous layer of Ru on top. The CoPt grain is also clearly outlined, and we see that it has grown on top of the dome. We were unable to map the location of Si or O due to poor signal to noise ratio in the EDS spectra, but considering the contrast in the HAADF image as well as the bright field plane-view images, it is evident that the SiO<sub>2</sub> is in-between the CoPt grains, and in the trenches defined by the Pt domes.

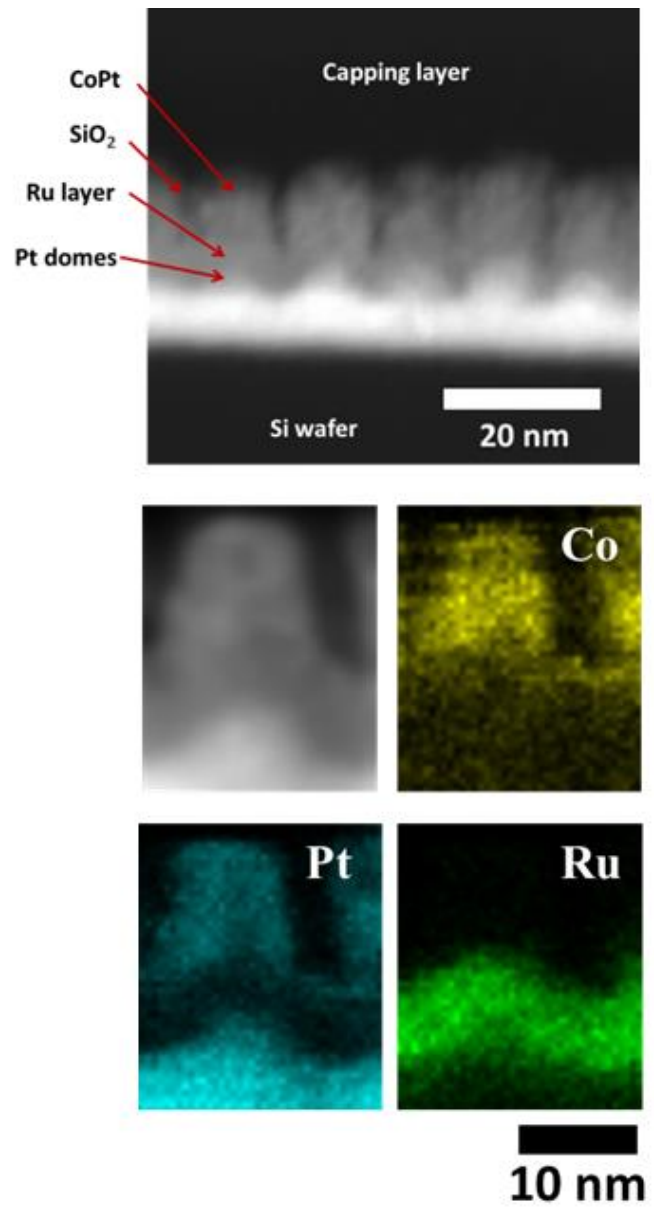


Figure 6-22: (a) Cross-section HAADF STEM micrograph of templated CoPt-SiO<sub>2</sub> media (b) High resolution EDS of one of the templated media grains

## 6.6. Conclusions

In this chapter, we discussed the magnetic properties of templated media fabricated using three different template layers, i.e. CoCrPt, Ru, and Pt. Here is a brief summary of the findings:

- The ion-milling step to fabricate the dome-morphology in CoCrPt resulted in isolated magnetic domes which exhibited low coercivity and low remnant magnetization, which in-turn acted as a magnetically soft layer after the sputtering of the media.
- A key consideration to take into account is the generation of a fresh underlayer surface prior to media sputtering, as was discussed in section 6.4 of this chapter. While Ru is a suitable template layer in terms of lattice matching with CoCrPt, the surface of the patterned Ru template needs to be sputter-etched prior to media deposition, and no suitable sputter-etching solution was available in our case.
- The use of Pt as the template layer helped solve this problem: Pt does not oxidize at room temperature, and any ion beam damage to the Pt surface is repaired, at least partially, by the Ru underlayer sputtered onto the template prior to media deposition.
- The templated media fabricated using Pt as the template layer had better magnetic properties as compared to the Ru template.
- Plane-view TEM imaging showed a regular CoPt-SiO<sub>2</sub> microstructure with grain positions defined by the template. An average grain size of 16.2 nm with a distribution of 11% was achieved.
- In cross-section TEM, we found that the Ru forms a conformal coating on the patterned Pt domes, and the CoPt grows on the Ru domes, with SiO<sub>2</sub> growing in the trenches.

In the next chapter, we discuss the application of the templated growth technique for the fabrication of Bit Patterned Media.

## CHAPTER 7

# Bit Patterned Media using Templated Growth

### 7.1. Introduction

In chapter 1, we discussed the additive and subtractive approaches for the fabrication of Bit Patterned Media (BPM). Here, we discuss a new additive approach for BPM fabrication using the templated growth process. While earlier studies using the additive approach have focused on the fabrication of high aspect ratio posts and minimization of trench material during the sputtering process[27], [31], [47]–[50], the templates in our case consist of the dome-morphology discussed previously and growth of magnetic material usually along with a suitable segregant. This project was done in collaboration with Seagate.

### 7.2. Experimental Details

For the fabrication of Bit Patterned Media, long range ordering of the magnetic grains/islands is essential. On the other hand, the center-to-center distance or pitch between these magnetic islands need not be sub-20 nm to begin with, although the process should be suitable for scaling to these sizes and further. The Pt (111) template layer in combination with the Ru (00.2) underlayer, as discussed in chapter 6, is suitable for the fabrication of CoPt based media.

A film stack of Ta (3nm)/Pt (30nm)/C (20nm) was sputtered onto glass disks using system #4, and sent to Seagate for nanoimprint lithography and pattern transfer. Figure 7-1 below shows the SEM images of the disks returned to CMU after processing at Seagate. The primary region of interest (Region A) consisted of a hexagonal array of am-C pillars, which were 20 nm in height and spaced by approximately 27 nm (center-to-center). Figure 7-1(b) shows a SEM micrograph of the long-range spatially ordered hexagonal array, with a higher-magnification image shown as inset. The bands of Region A were approximately 30  $\mu\text{m}$  in width, bounded by Regions B and C on either side. Region B consisted of a similar pattern, with 52 nm pitch, while Region C consisted of periodically spaced patterned mini-bands, each of which consisted of three lines of am-C pillars spaced by approximately 20 nm.

Further processing, including ion-milling and media deposition and characterization of the microstructure and magnetic properties were done here in CMU. The ion-milling, as in the earlier chapters, were performed using a Commonwealth Scientific ion mill. The sputtering of the Ru underlayer and the CoPt was done using the Z400#1 sputtering system. The parameters used for the various processes are specified in the relevant sections.

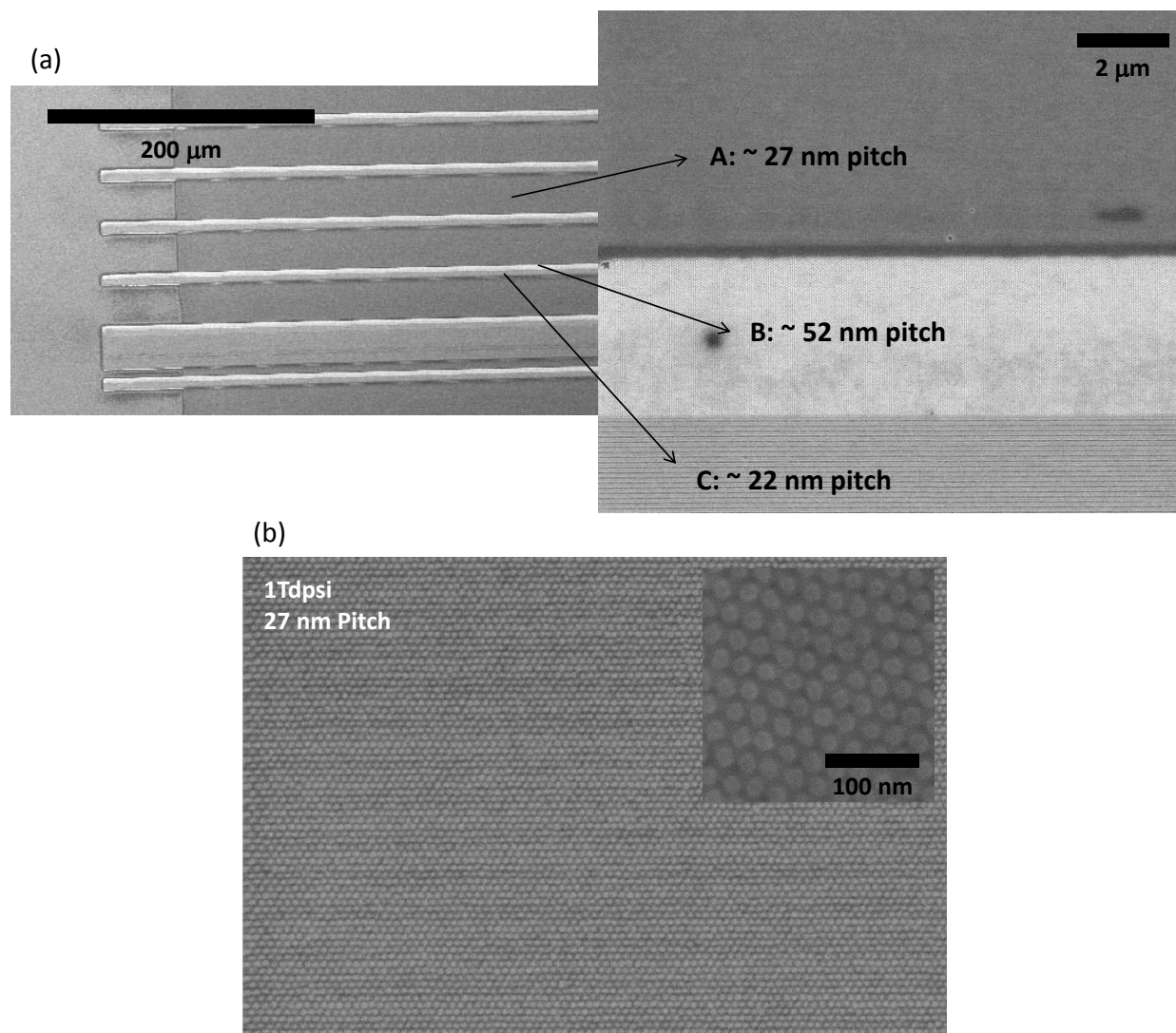


Figure 7-1: (a) SEM images of the patterned disk, labeling patterns with different pitch (b) Magnified images of 1 Tdpsi region (27 nm pitch)

### 7.3. Results and Discussion

Since the pitch of interest here (27 nm) is larger than the block copolymer pitch attempted before (17 nm), the ion-milling parameters, and the sputter deposition parameters have to be re-optimized. The disks obtained from Seagate were diced into 7x7 mm pieces and utilized for the process optimization. Figure 7-2 shows the summary of the various parameters which were varied

in the first set of experiments, the parameters in red being held constant and the parameters in green varied. The MOKE setup with a laser spot size of approximately 17  $\mu\text{m}$  was used so that the out-of-plane hysteresis loops of Region A could be studied. Regions B and C were too small for the magnetic properties to be measured in an isolated fashion. The MOKE results presented in this chapter were performed by Zhengkun Dai.

Figure 7-2 (b) and (c) show the summary of the measured magnetic properties. We see that all of the attempted processing parameters resulted in media with low coercivity (between 1500 Oe and 3500 Oe) and low remnant magnetization (approximately 0.7  $M_s$ ). Further, none of the processing parameters attempted resulted in significant changes in the magnetic properties. Two of these trends are showcased in Figure 7-2 (c) and (d). The first thing we note in both these figures is the low anisotropy for all of the media samples, as seen from the low loop squareness. In Figure 7-2 (c), we see that varying the ion-milling time of the Pt template layer between 30 to 50 seconds results in media properties which are nearly equivalent, with low coercivities of approximately 2000 Oe and low  $M_r$  of 0.67  $M_s$ . Since ion-milling time of the template should affect the dome-morphology, with higher ion-milling times resulting in lower aspect ratio domes, these results indicate that we are not in a region of parameter space where the dome-shape is critical. In Figure 7-2 (d), we picked 25° as the ion-milling angle, 30 seconds as the ion-milling time and varied the thickness of the Ru underlayer from 5-15 nms. The increase from 5 to 10 nms results in a marginal improvement in the media coercivity (from 2000 Oe to 3000 Oe), but further increase in thickness to 15 nm did not cause any improvement. Further, the squareness of the loop is still low ( $M_r/M_s \sim 0.74$ ), indicating to us that while increasing the Ru thickness could improve the magnetic properties, we are still not in the right region of parameter space.

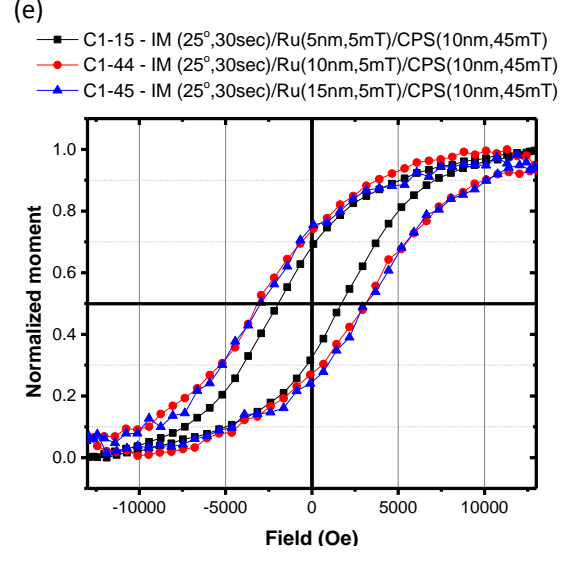
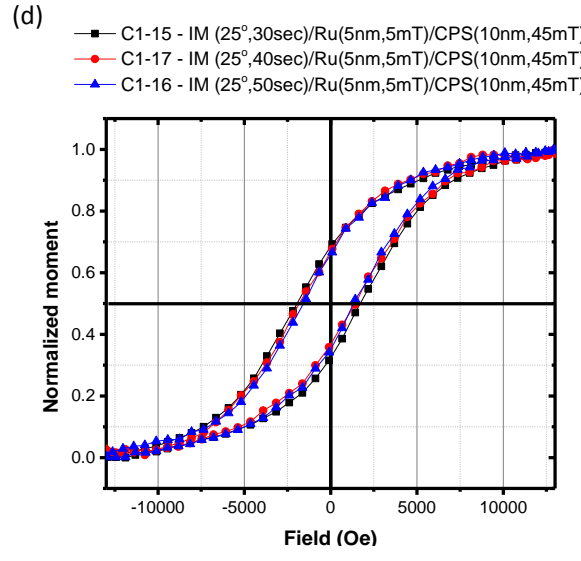
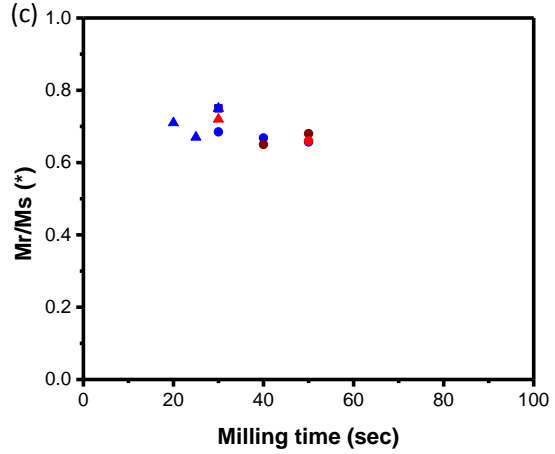
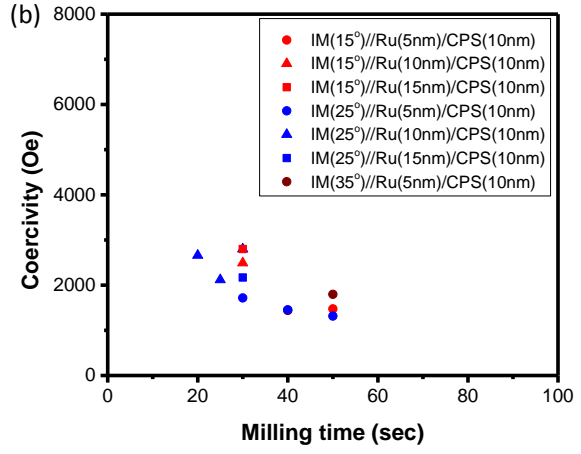
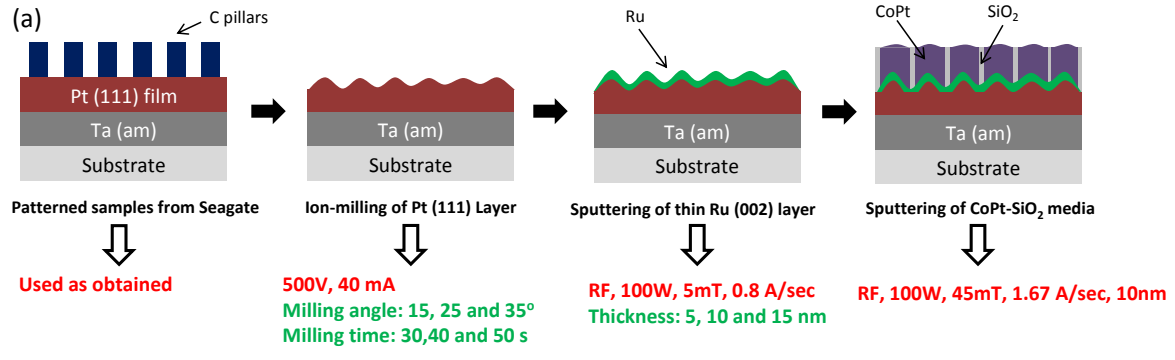


Figure 7-2: (a) Summary of varied and constant processing parameters (b) Coercivity vs ion-milling time for various samples (c)  $M_r/M_s$  vs ion-milling time for various samples (d) Effect of ion-milling time on the magnetic properties of templated media (e) Effect of Ru underlayer thickness on the magnetic properties of templated media

Given the low anisotropy in all of these samples, it is likely that the surface of the template after ion-milling (and prior to Ru and media deposition) is not Pt (111). As discussed in the previous chapter, Pt (111) surface has only a 2.5% lattice mismatch with a Ru (00.2) surface, and should thus result in good (00.2) orientation of the Ru and the subsequently sputtered media. However, if the amorphous carbon mask is not completely eroded at the end of the ion-milling process, the Ru will encounter an amorphous carbon surface, resulting in a somewhat random orientation of the Ru grains. Cross-section TEM using the Tecnai F20 microscope was used to confirm this. FIB liftout using the NovaLab 600 Dual-Beam FIB SEM was used to prepare a cross-section specimen from a Region A sample prepared with the following processing parameters: ion-milling - 25°, 30 sec, Ru layer - 100W RF, 5 nm, 5 mT and CoPt-SiO<sub>2</sub> layer - 100W RF, 10 nm, 45 mT.

The TEM results are shown in Figure 7-3. We see bright dome-like features spaced by approximately 27 nm in the lower-magnification bright-field TEM image (Figure 7-3(a)). Considering the higher diffraction contrast and hence the darker-appearing Pt underneath these domes, these are likely to be leftover amorphous carbon. This is confirmed in the HAADF image (Figure 7-3 (c)), wherein the regions with lower average atomic number or 'z' appear darker; we see that the domes composed of carbon ( $Z = 6$ ), appear darker than the Pt ( $Z = 78$ ) underneath and the Ru ( $Z = 44$ ) on top. The amorphous carbon is thus not completely eroded at the end of the ion-milling process. As seen in the high-resolution micrograph Figure 7-3 (b), this results in the growth of Ru with random orientation (compare the orientation of the Ru (00.2) lattice fringes with  $d \sim 0.214$  nm on top of the dome with the Pt (111) fringes with  $d \sim 0.225$  nm underneath the domes), which subsequently results in random orientation of the media sputtered later, explaining the poor magnetic properties discussed earlier. The lattice fringes seen within the am-C domes also match

with Ru (00.2), which can be explained by taking into consideration that the TEM specimen thickness is unlikely to be lesser than the width of the dome, and therefore the Ru (00.2) planes behind and in front of the am-C dome in the specimen contribute to the 2-D TEM image as well.

Another observation from the cross-section HAADF image is the presence of regions with dark contrast between the Ru grown on each dome. Considering that Ru is not co-sputtered with any oxide, this contrast can only be explained by attributing the contrast to the presence of voids between the Ru regions. While the self-shadowing effect during sputtering could result in such voids, it is surprising that this effect was found although the Ar pressure during sputtering is low, i.e. 5 mT. The presence of these voids indicate that the dome-morphology alone could be sufficient to create spatially isolated islands in the magnetic media sputtered on top, that a segregant may be unnecessary. This idea is discussed further towards the end of this chapter.

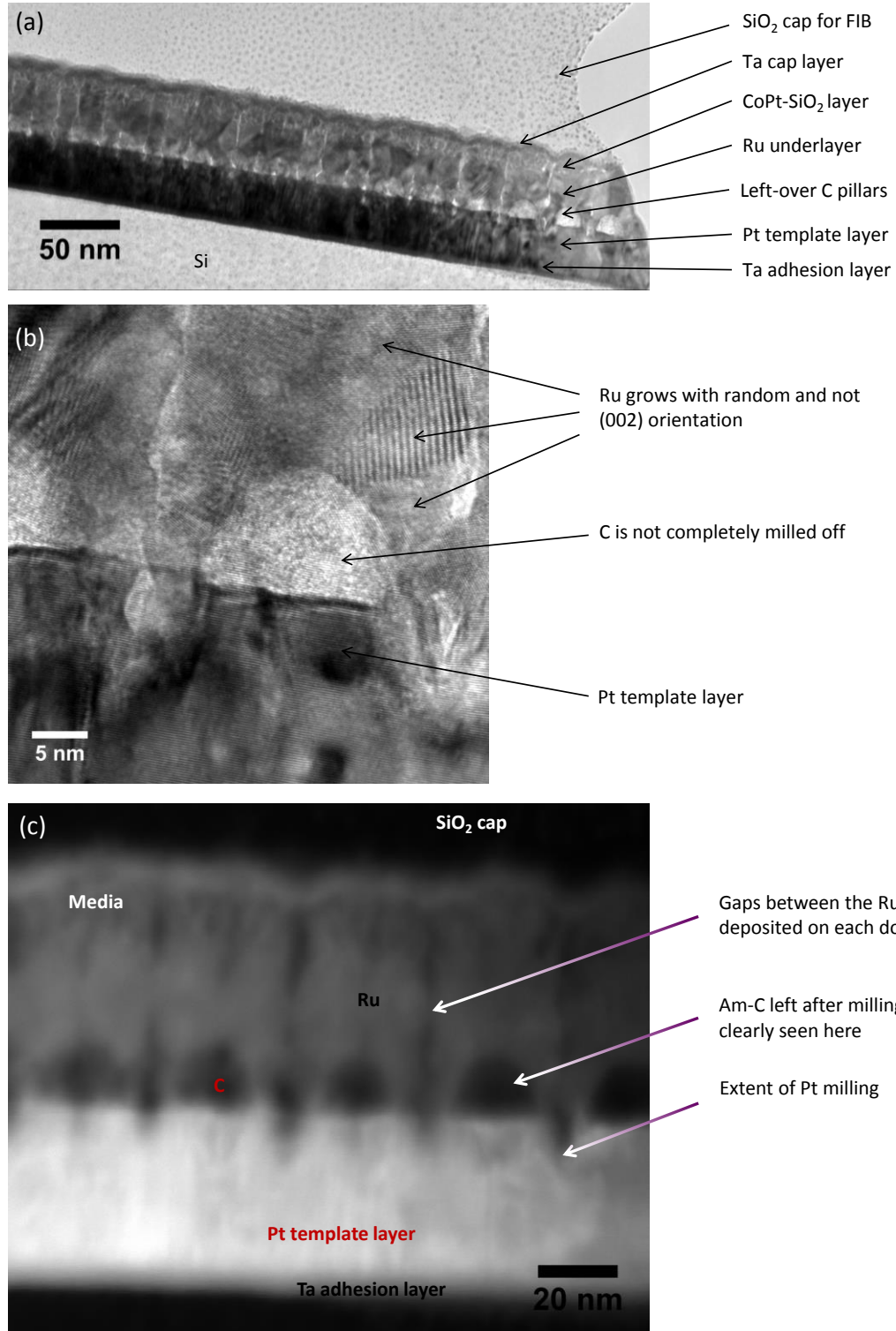


Figure 7-3: (a) Bright-field cross-section TEM micrograph of chosen sample (b) Magnified high-resolution cross-section TEM micrograph of Ru grown on one dome (c) High-Angle Annular Dark Field (HAADF) cross-section image

The HAADF image further gives us information regarding the depth to which the Pt has been milled, and the approximate amount of amorphous carbon remaining, as illustrated in Figure 7-4. The illustration of the sample before milling shows us that for the current mask structure, i.e., carbon pillars which are 20 nm tall and 20 nm in diameter, the ion-milling angle has to be less than  $9.9^\circ$  for the ion-beam to reach the Pt. If the ion-milling angle is greater than  $9.9^\circ$  (as illustrated by the  $25^\circ$  case in the schematic below), the ion-beam clearly does not reach the Pt underneath. We also see from the illustration to the right, that only approximately 50% of the carbon domes have been milled away, while nearly 10 nm ( $\sim 33\%$  of the Pt has been milled). Given that the milling rate for carbon is 5 times slower than Pt, we can estimate that the Pt will be completely milled through before the carbon is eroded away. Thus for this Pt thickness, the current carbon mask structure is unsuitable.

One solution for removing the carbon is to dry-etch the carbon after ion-milling using RIE, but the Pt template now has a flat top region since the area beneath the carbon has not been milled, and this may not be an effective template for our purpose. We thus need to estimate the height and width of the carbon pillars in such a way that the carbon is completely eroded away during the ion-milling process.

We thus modify (or 'pre-etch') the carbon pillars using an oxygen plasma in a Plasma Therm 790 RIE system. The pre-etching time has to be optimized in combination with the ion-milling angle and time in such way that the erosion of carbon is complete when we get the required dome morphology for the templated growth. In RIE, the high pressure of 50mT was chosen to increase the lateral etching component. Ion-milling angles of  $15^\circ$  and  $25^\circ$  and times of 30-50 seconds were attempted. The Ru and CoPt-SiO<sub>2</sub> sputtering conditions were held the same and the Z400#1

sputtering system was used as before. The RIE and sputtering conditions are summarized in Table 7-1.

Table 7-1: Summary of processing parameters for pre-etching and sputtering

RIE	Gas (O <sub>2</sub> ), Flow (20 sccm), Pressure (50mT), Time (varied from 30 to 60 sec), Power (20W)
Ru Deposition	Power (100W RF), Pressure (5mT Ar), Rate (4 nm/min), Thickness (~ 10 nm)
CoPt-SiO <sub>2</sub> Deposition	Power (100W RF), Pressure (45mT Ar), Rate (10 nm/min), Thickness (~ 10nm)

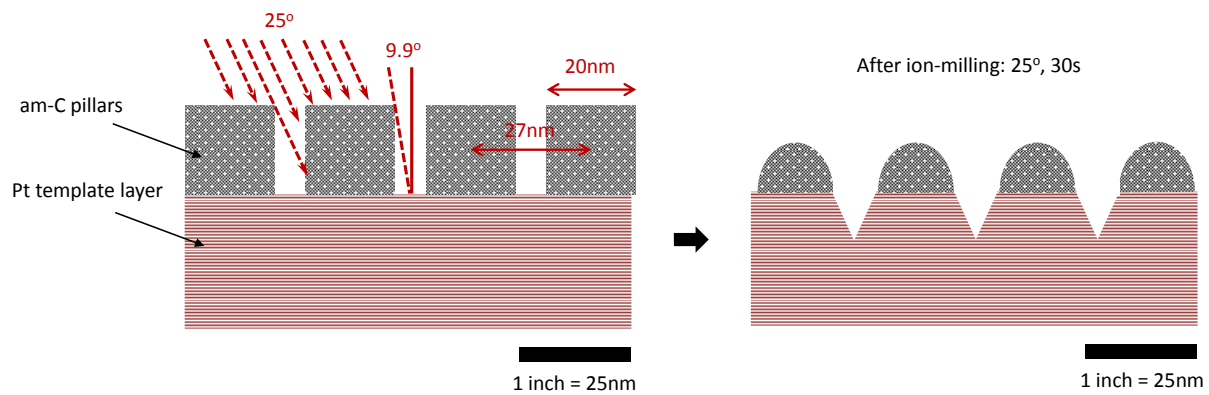


Figure 7-4: Schematic illustrating the am-C mask structure

The magnetic hysteresis loop results are presented in Figure 7-5. For the 30 seconds ‘pre-etch’ time, we see that there is not much improvement in the magnetic properties. However, the 60 seconds pre-etch time, in combination with 40 to 50 seconds of ion-milling at 15° results in magnetic media with good coercivity (~ 5 kOe).

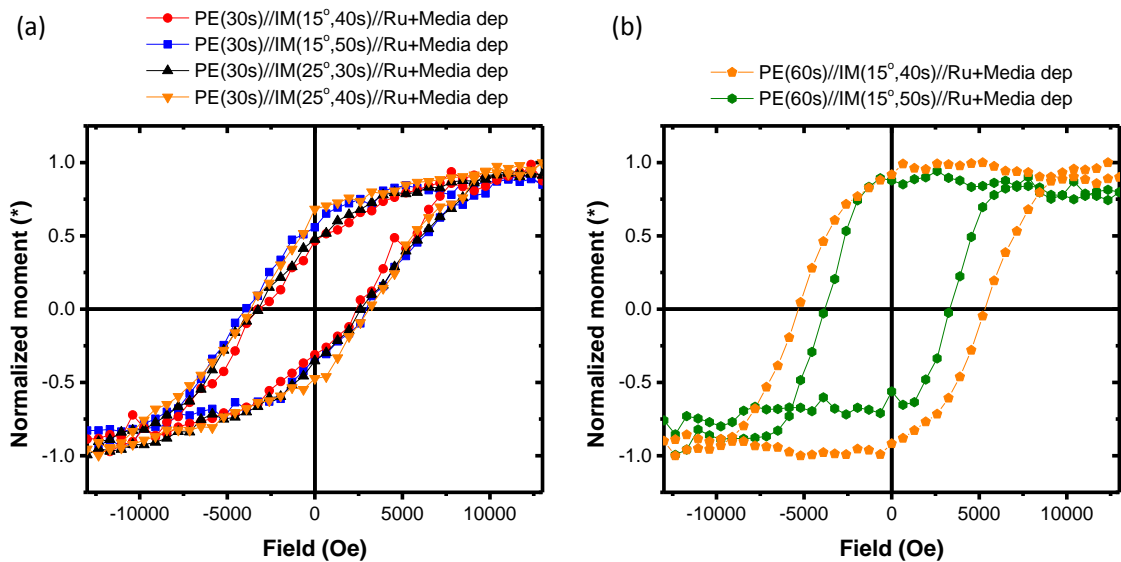


Figure 7-5: Effect of pre-etching for (a) 30 sec (b) 60 sec on the magnetic properties of subsequently grown templated media

We can then use regions of the sample which are not patterned with the dome-morphology to understand the effect of the template on the magnetic and structural properties of the media. The templated media has a much higher coercivity of around 5 kOe (see Figure 7-6 (b)) than the untemplated media ( $\sim 1$  kOe). The slope of the normalized hysteresis loop of the templated media is approximately  $3.6 \times 10^{-4}$ . The slope of a decoupled array of magnetic grains in a thin film is approximately  $\frac{1}{4\pi M_s}$ , which results in values of  $1.6 \times 10^{-4}$  (if  $M_s = 500$  emu/cc) and  $1.3 \times 10^{-4}$  (if  $M_s = 600$  emu/cc). The higher measured value of the slope for the templated media indicates that there is some degree of exchange coupling in the media. The slope for the untemplated media however, which has a sharp drop in magnetization once the nucleation field is reached, indicates that the untemplated media is completely exchange coupled.

The out-of-plane diffraction patterns for templated vs untemplated media are shown in Figure 7-6 (a). The x-ray beam spot size was reduced to 500x500  $\mu\text{m}$  and the beam was centered on the patterned and then on the unpatterned region so that a representative scan could be obtained. Since the templated region is partially masked by carbon unlike the untemplated region, the Pt (111) peak for the templated region is higher. On the other hand, the Ru and CoPt peaks are higher and better defined for the untemplated region, indicating that the untemplated media has better (00.2) texture. One possible explanation for this is that the curved dome morphology in the template results in worse (00.2) texture as compared to the flat untemplated region.

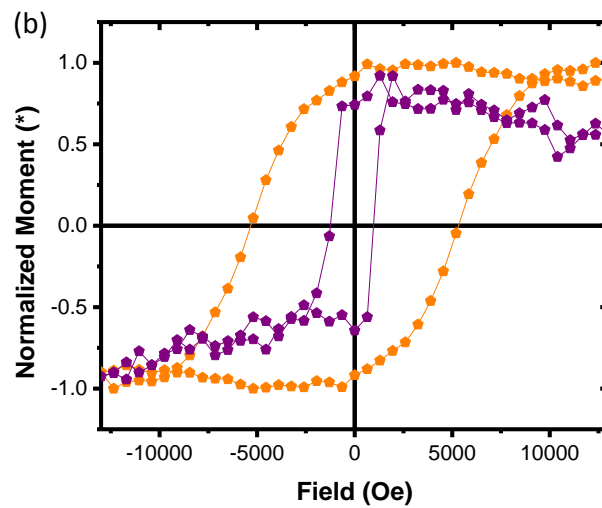
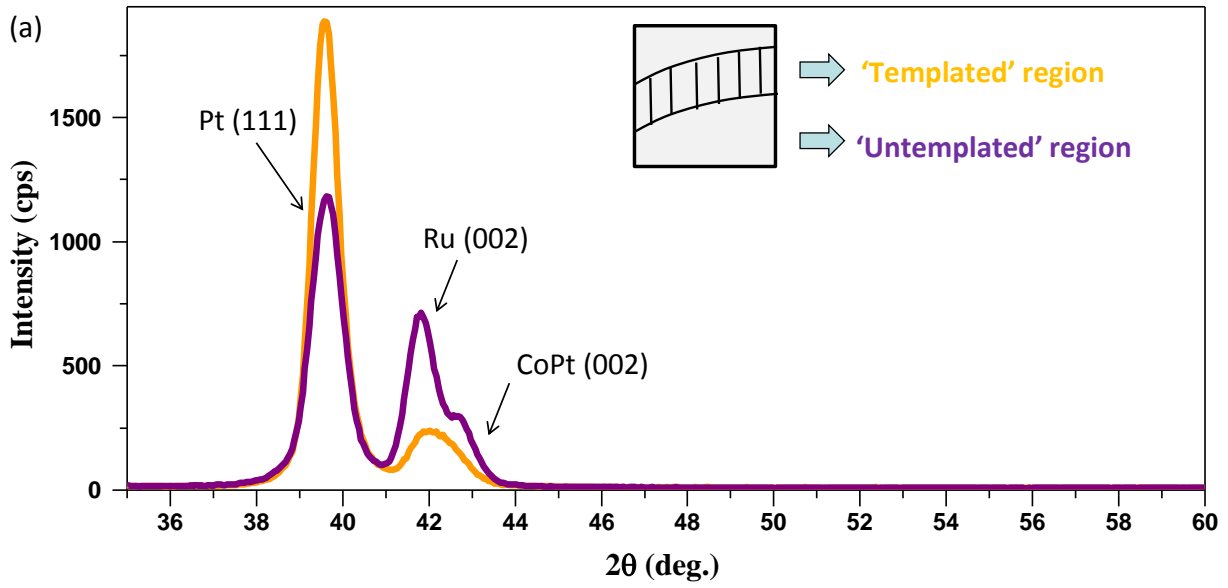


Figure 7-6: Comparing out-of-plane (a) XRD patterns and (b) M-H loops of templated and untemplated regions in the same sample

The plane-view microstructure of the templated sample is shown in Figure 7-7 below. The bright-field plane view TEM image from Region A shows a hexagonal array of CoPt grains surrounded by bright amorphous SiO<sub>2</sub>. The spacing between the grains is approximately 27 nm, as defined by the template. This microstructure in combination with the high coercivity in the out-

of-plane magnetic properties indicates that the templated growth technique is promising for the fabrication of Bit Patterned Media. One of the aspects that require further improvement here is the thickness and uniformity of the SiO<sub>2</sub> boundaries. The thin SiO<sub>2</sub> boundaries might cause a certain degree of exchange coupling between the adjacent grains, which could explain the higher value of slope obtained for the templated media. The indexed plane-view diffraction pattern indicates (00.2) out-of-plane texture as expected from the XRD pattern.

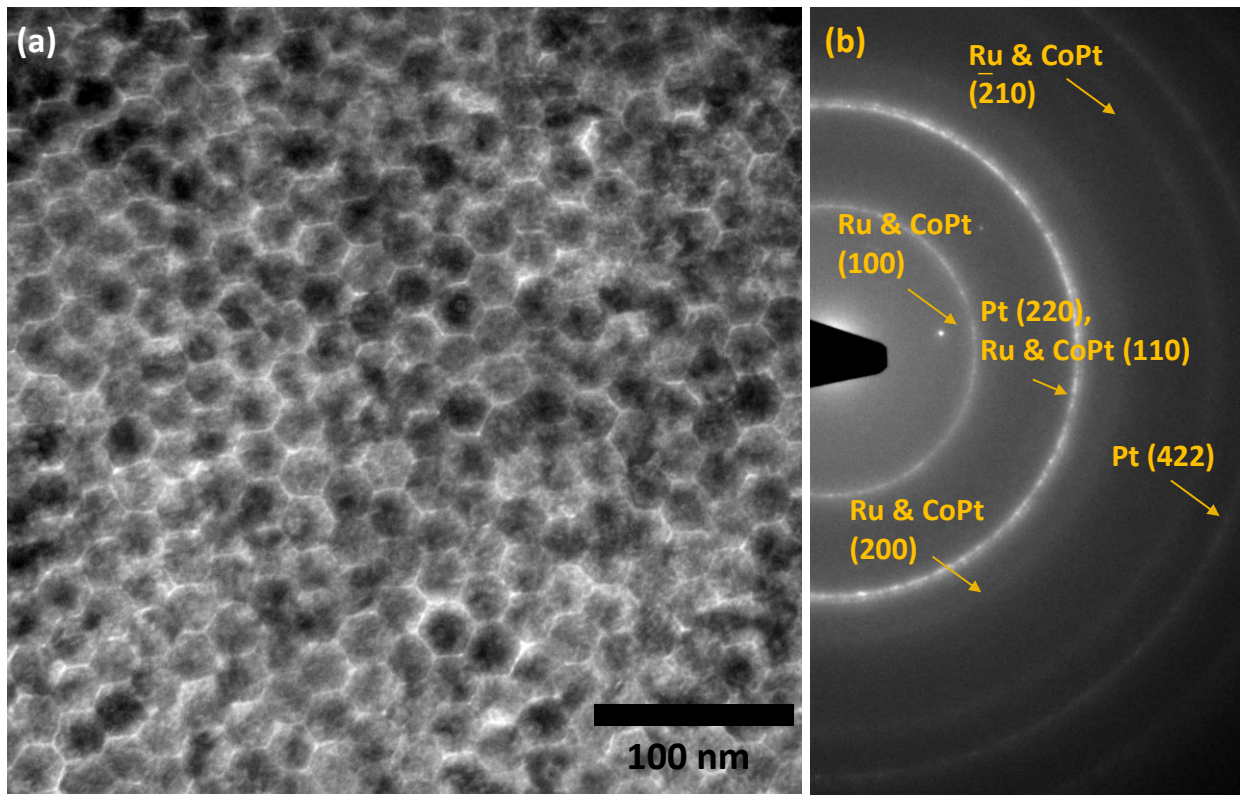


Figure 7-7: Plane-view TEM (a) Bright-field micrograph (b) Indexed diffraction pattern of templated BPM media S2 with  $H_c = 5000$  Oe

Figure 7-8 shows the plane-view TEM micrographs for Region B. The magnetic properties of this could not be measured since its width was lesser than the laser spot size of  $17 \mu\text{m}$  in our MOKE setup. Here we see that CoPt grains surrounded by SiO<sub>2</sub> are also present in the regions

between the domes. This is because unlike Region A, there is a large gap of approximately 25 nm between two domes in Region B.

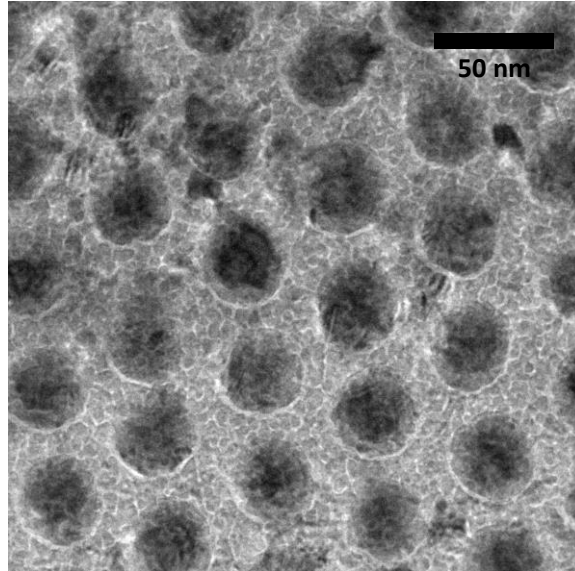


Figure 7-8: Plane-view bright field TEM micrograph for Region B from the templated BPM media S2

## 7.4. Conclusions

In this chapter, we discussed the mask structure design and process development for the fabrication of CoPt islands for Bit Patterned Media application. Samples with a well-ordered array of amorphous carbon pillars was fabricated by nanoimprint lithography by Seagate. Here at CMU, the height and width of the amorphous carbon pillars was optimized in combination with the ion-milling time for template fabrication. The effectiveness of the template was evaluated by studying the properties of the subsequently deposited CoPt-SiO<sub>2</sub> magnetic media. Media with a coercivity of approximately 5000 Oe was achieved. Plane-view TEM indicates that the magnetic media microstructure is guided by the template, and a regular array of CoPt grains spaced by approximately 27 nm and surrounded by amorphous SiO<sub>2</sub> was observed. The microstructure and

magnetic properties thus indicate that the templated growth technique is a promising approach for the fabrication of Bit Patterned Media.

# CHAPTER 8

## HAMR Media using Templated Growth

### 8.1. Introduction

In this chapter, we discuss the fabrication of templates for the guided growth of FePt based media. As discussed in chapter 1, FePt has an  $L1_0$  crystal structure, with the magnetic easy axis along the c-axis of its structure, which consists of alternate layers of Fe and Pt atoms. In order to enable the ordering, FePt is sputtered at an elevated temperature, of approximately 600°C. Thus, in this study, we have to address two questions: the first one is regarding the stability of the patterned dome morphology at the high temperatures necessary for FePt deposition and ordering. The second is whether the templated growth concept works at high temperature sputtering.

### 8.2. Results and Discussion

For this study, single crystal MgO (001) substrates (purchased from MTI Corp.) were used. Tungsten (W) and Platinum (Pt) films were tested as the template layers, and were grown on the MgO single crystal substrates. Figure 8-1 shows the crystal structure of the various materials involved. As we can see, W (along [110]), Pt (along [100]) have close lattice matching with FePt (along [100]), and are suitable conductive underlayers. Sputtering system #2 in the Nanofab facility, equipped with a substrate heater, was utilized for the FePt, Pt, MgO film depositions while the CVC sputtering system was used for W deposition.

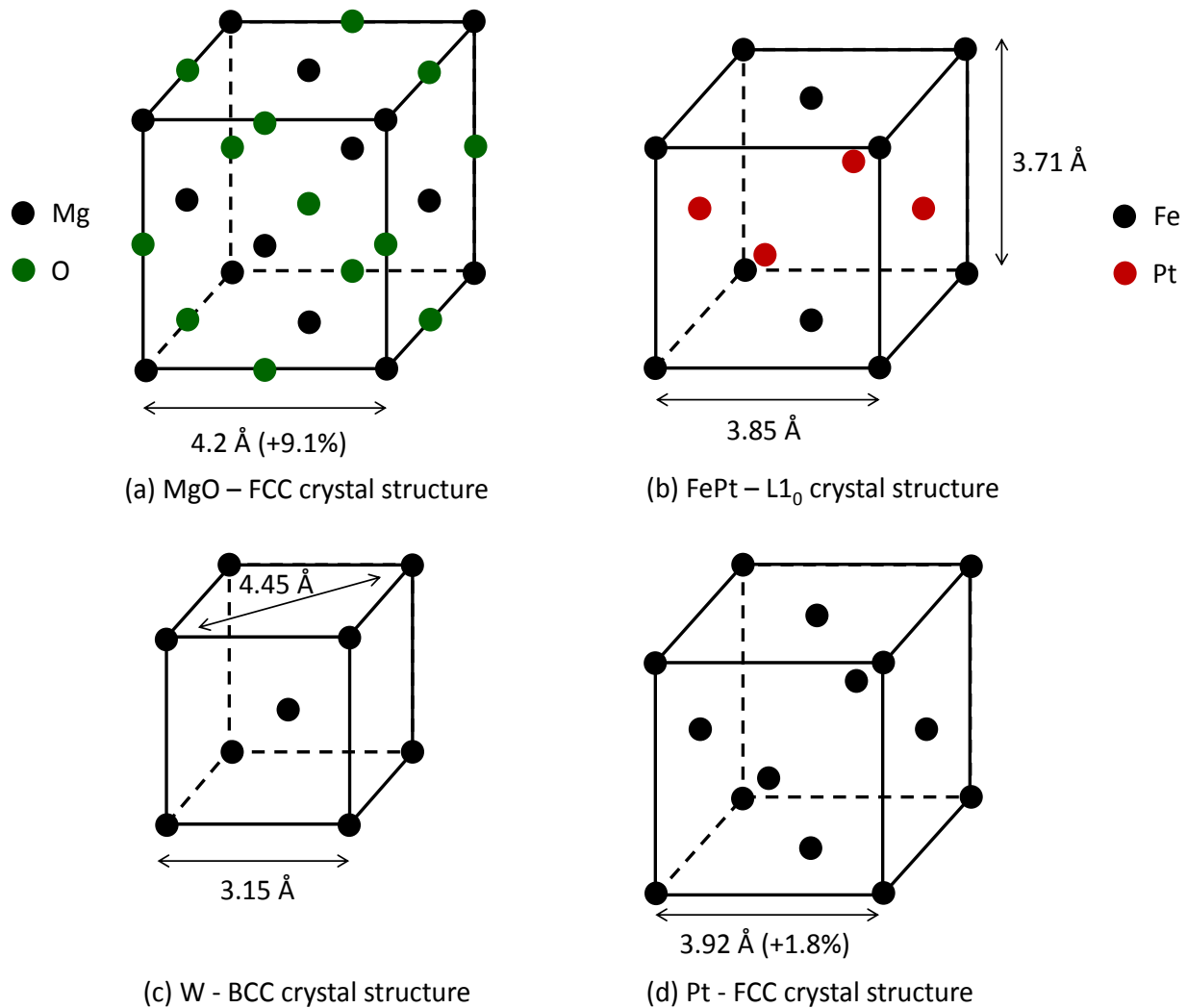


Figure 8-1: Crystal structures of (a) MgO (b) FePt (c) W (d) Pt

30 nms of both W and Pt films were deposited. Figure 8-2, below, shows the out-of-plane and in-plane diffraction patterns for the W film deposited on the MgO substrate. The W (002) peak at approximately  $58^\circ$  confirms the required (002) texture for the W film. Since an MgO single crystal substrate was used, the in-plane scans reveal the orientation relationship between the MgO and the W. When the MgO substrate was oriented such that the [100] direction was parallel to the x-ray beam direction, the W (110) peak is observed, and when the substrate is rotated  $45^\circ$  such that the

MgO [110] is parallel to the x-ray beam, the W (200) peak is observed. This indicates the following, expected orientation relationship for the W and the MgO:  $(002)_{\text{MgO}} \parallel (002)_{\text{W}}$ ,  $[100]_{\text{MgO}} \parallel [110]_{\text{W}}$ .

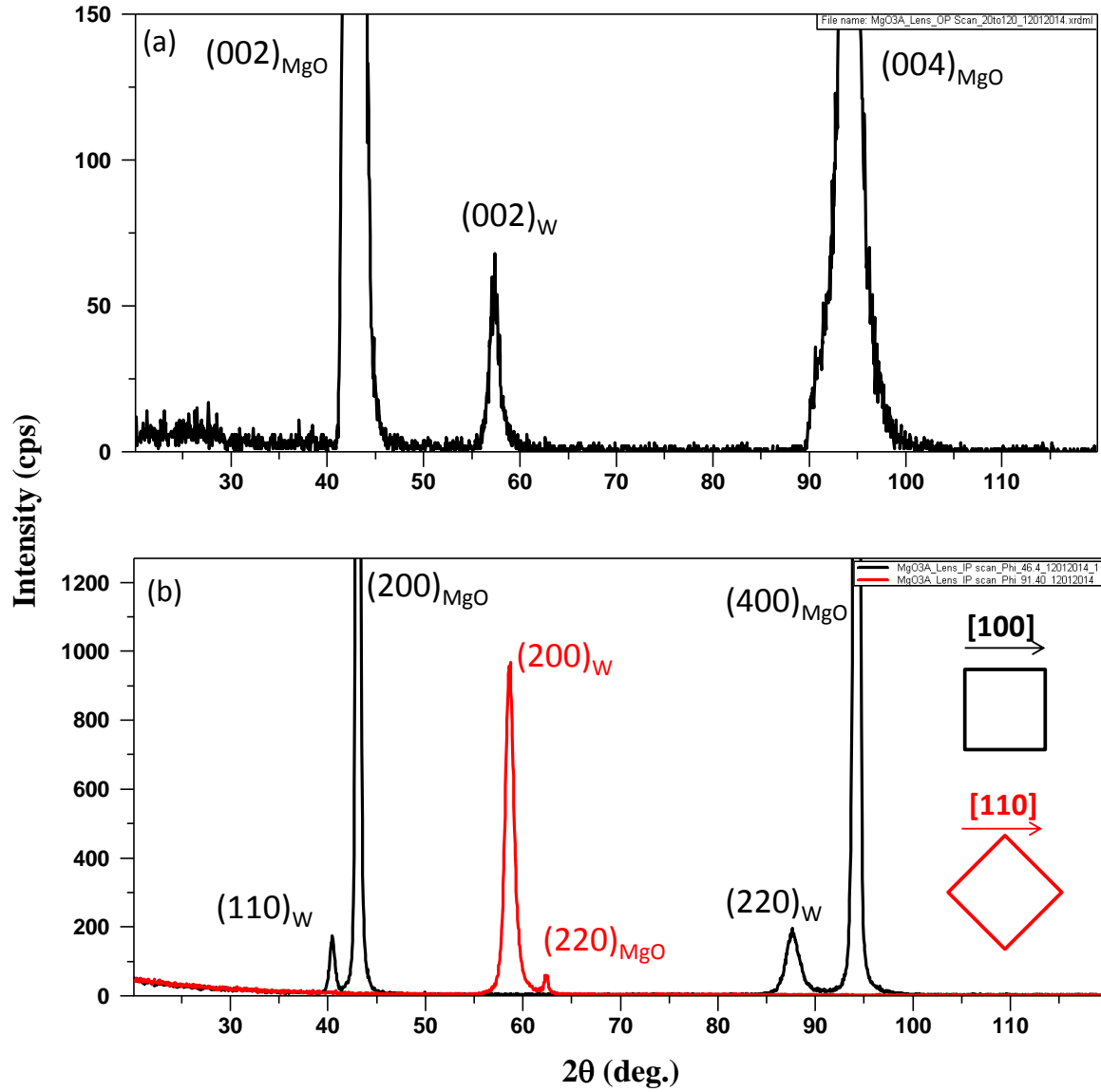


Figure 8-2: (a) Out-of-plane and (b) in-plane x-ray diffraction patterns for 30 nm W film on MgO

Similarly a 30 nm Pt film was sputtered onto an MgO single crystal substrate, at 425°C. The presence of the Pt (002) peak at 46° (see Figure 8-3) confirms the required texture. The high temperature was used since, at room temperature, Pt tends to grow with the FCC (111) texture[85]. A rocking angle of 0.5° was obtained for the Pt (002) peak. The in-plane XRD scans show the presence of the Pt (200) peak (when the beam direction is parallel to the MgO substrate [100]) and the Pt (220) peak (when the beam direction is parallel to the MgO substrate [110]) indicates the following orientation relationship for the Pt film on the MgO:  $(002)_{\text{MgO}} \parallel (002)_{\text{Pt}}$ ,  $[200]_{\text{MgO}} \parallel [200]_{\text{Pt}}$ .

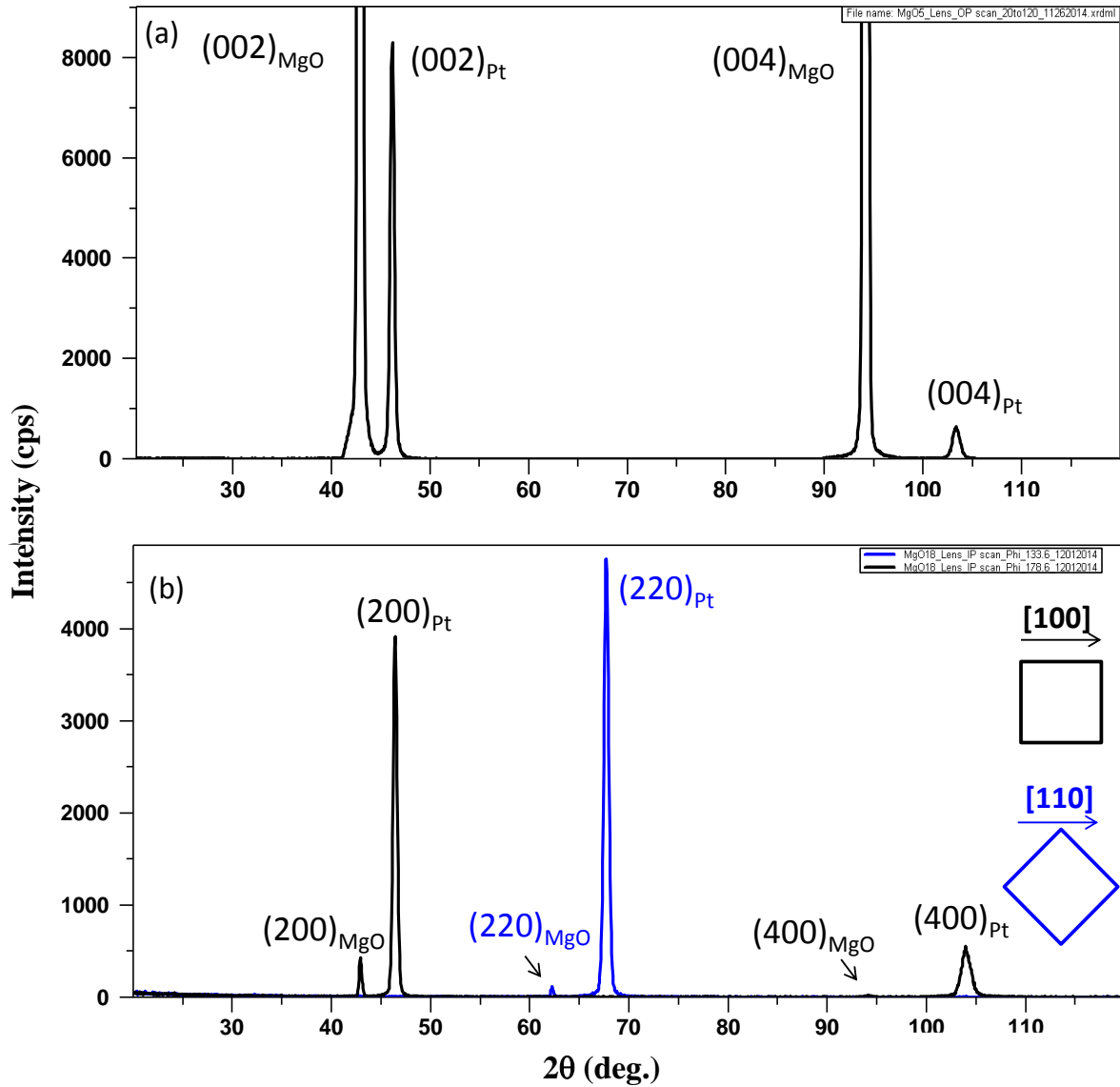


Figure 8-3: (a) Out-of-plane and (b) in-plane x-ray diffraction patterns for 30 nm Pt film on MgO

On these W and Pt films, 20 nm of amorphous carbon hard mask was sputtered, block copolymer PSD2 was spin coated, and thermally annealed at 130°C for 24 hours to facilitate micro-phase separation as discussed in chapter 5. After plasma etching into the amorphous carbon layer, ion-milling was done for 30 seconds at an angle of 12.5°. On heating at 600°C for 30 mins, we see

from the plane-view SEM micrographs shown in Figure 8-4 that the W film has delaminated (as seen from the low magnification image), and the dome-morphology that was patterned into the W is clearly flattened. A similar result was obtained for the Pt underlayer case, as seen from the SEM images in Figure 8-5. A template consisting of Pt or W is thus not suitable for templated HAMR media fabrication since the dome-morphology is not stable at the elevated temperatures required for well-ordered FePt. However, in both cases, it was found that if an MgO cap was sputtered on the template first prior to increasing the temperature, the dome-morphology was retained (see Figures 8-4 and 8-5).

In order to understand the observations described above, we need to consider the surface mobility and surface energy characteristics of the various materials involved. The mobility of these materials can be considered to be roughly proportional to their melting points. In such a case, W with a melting point of 3422°C should have the lowest mobility as compared to Pt (1768.3°C) and MgO (2852°C), and so the W domes should be the most likely to be stable at high temperatures, which is clearly not the case. The consideration of interfacial energies help us understand this phenomenon better. Pt (002) and W (002) are not the natural growth textures for these materials. When sputtered onto an amorphous substrate for example, Pt grows with FCC (111) texture, and W grows with the BCC (110) texture. Therefore, the Pt (002) and W (002) are higher energy surfaces and thus, when the temperature is raised, the dome-morphology flattens to minimize the surface area. When an additional constraint is imposed on these surfaces, in the form of an MgO cap, the atomic diffusion along the surface is hindered, and the dome-morphology is stabilized. For MgO, FCC (002) is the natural growth texture, and the surface is thus a low energy surface, which corresponds to relatively lower surface mobility and thus the dome morphology is retained.

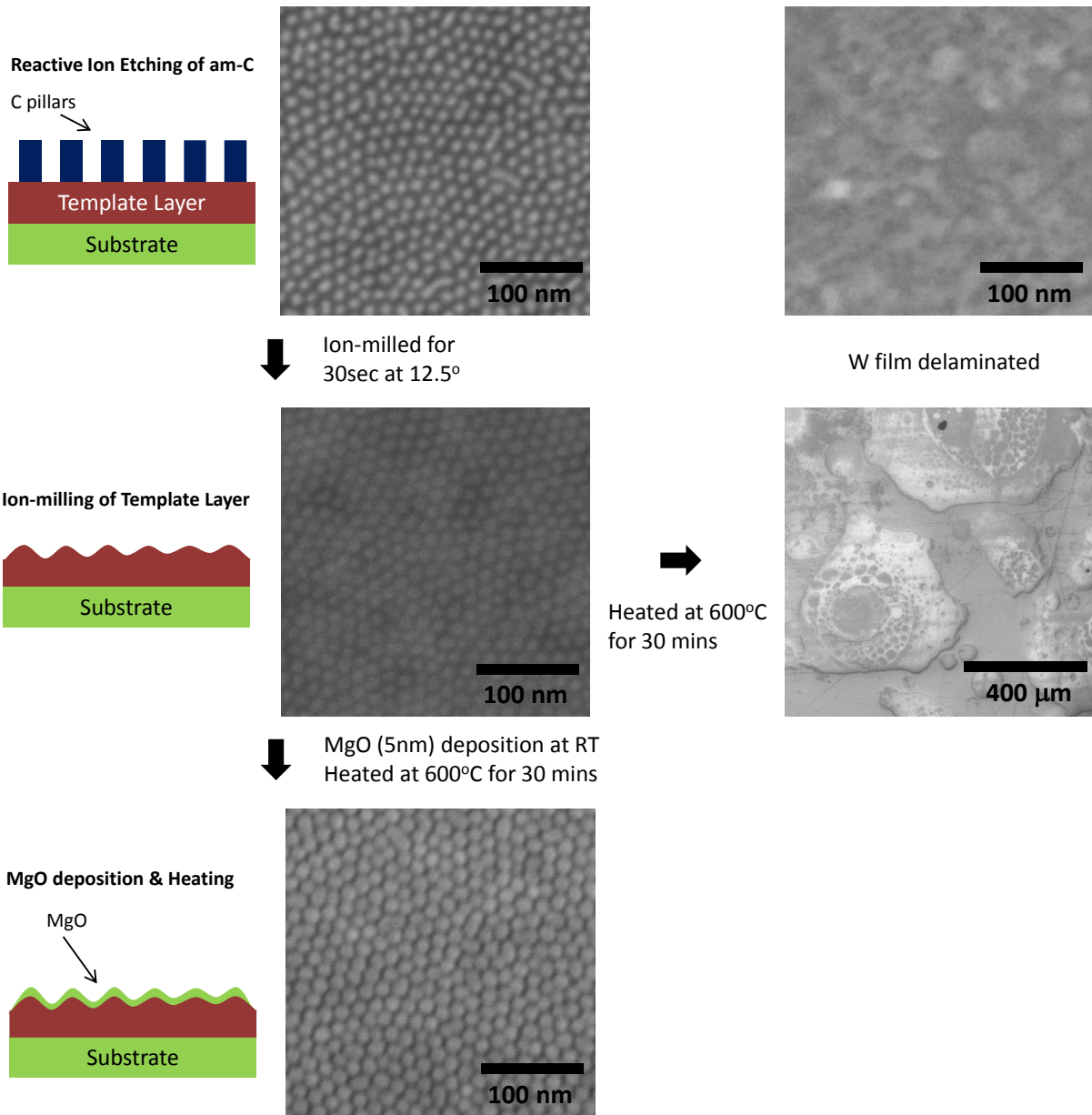


Figure 8-4: Process flow and example SEM images showing the various stages of patterning for W and effect of heating with/without MgO cap layer

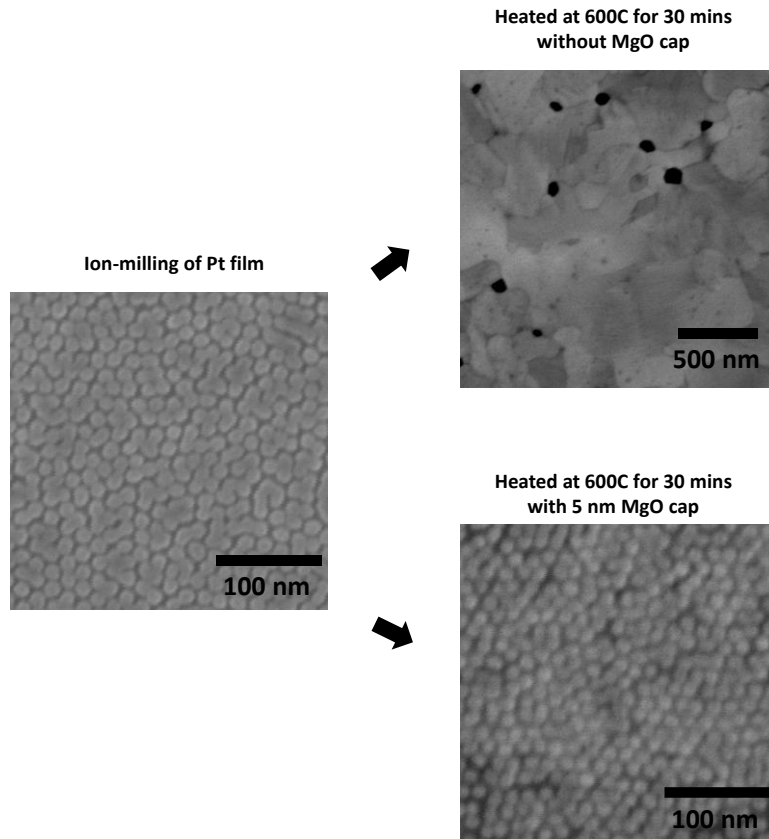


Figure 8-5: Effect of annealing on the dome-morphology patterned into Pt with and without the MgO cap layer

In order to evaluate whether the templated growth concept can be utilized for guiding FePt-SiO<sub>2</sub> magnetic media, we can thus simplify the process-flow to patterning the dome morphology into the MgO single crystal substrates. The other steps in the process flow are the same. After the ion-milling step, multilayers of FePt and SiO<sub>2</sub> were sputtered in an alternate manner at an elevated temperature of 590°C. The sputtering conditions are summarized in Table 8-1 below. The average oxide volume fraction was approximately 15 vol%.

Table 8-1: Summary of sputtering parameters for FePt-SiO<sub>2</sub> deposition

Sputtering FePt-SiO <sub>2</sub> at 590 °C	FePt (RF, 25W, 40mT, 0.09nm/sec) – 0.81 nm SiO <sub>2</sub> (RF, 50W, 40mT, 0.014 nm/sec) – 0.14 nm	} x 8
--	--	-------

The bright-field plane-view microstructure of FePt-SiO<sub>2</sub> templated media is shown in Figure 8-6(a). The FePt-SiO<sub>2</sub> microstructure is not as uniform as obtained in the previous chapters. This could be due to the coalescence of grains nucleating on adjacent domes. However, we see that the microstructure is quite different for the templated vs the untemplated case (shown in (b)). Further, the average spacing between the grains on the templated region is approximately 20 nm, as defined by the block copolymer pattern. This preliminary result indicates that the templated growth technique is promising for the fabrication of HAMR media. Further optimization using different segregants, and different volume fractions of the segregant is necessary to improve the media microstructure.

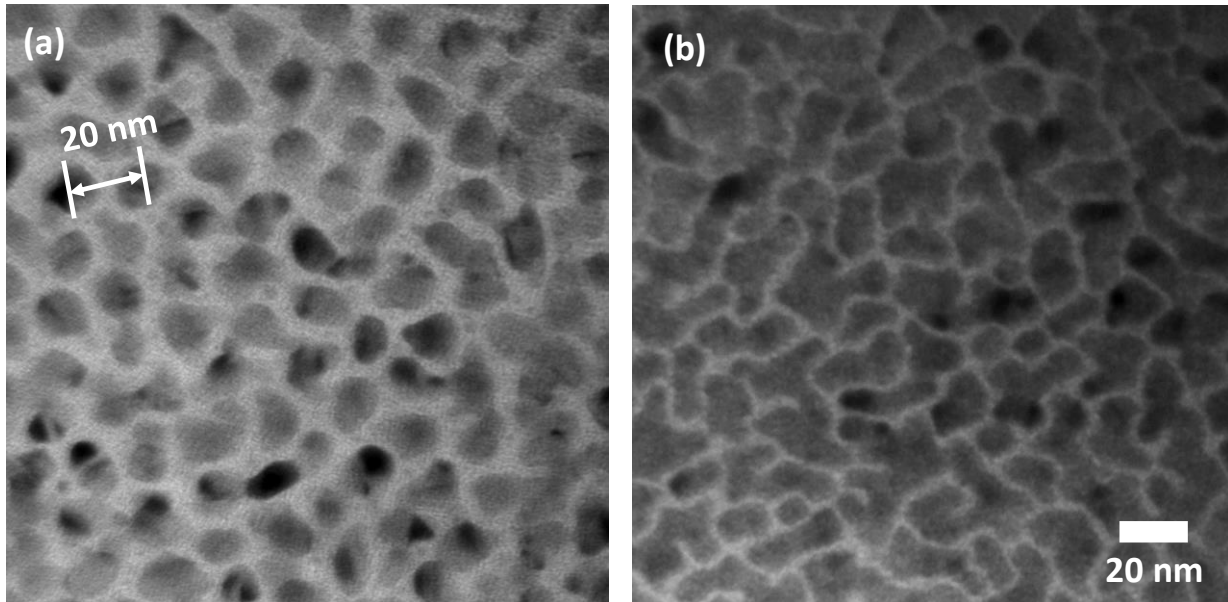


Figure 8-6: Bright field TEM micrographs of (a) templated FePt-SiO<sub>2</sub> media and (b) un-templated FePt-SiO<sub>2</sub> media

### 8.3. Conclusions

In this chapter, we discussed the experiments aimed at testing the templated growth technique for the fabrication of HAMR media. The dome morphology was patterned into two metallic underlayers, W and Pt using block copolymer PSD2, which had a pitch of 20 nm. On testing at high temperatures, we found that the dome-morphology was flattened. It was however retained if a thin MgO cap was deposited at room temperature prior to the heating. Preliminary microstructure results after FePt-SiO<sub>2</sub> media deposition onto MgO domes indicate that the templated growth could enable HAMR media microstructure control, but further optimization of the segregant type and volume fractions is required to verify this.

# CHAPTER 9

## Alternate Ideas for Templated Growth

### 9.1. Introduction

In this chapter, we discuss two other methodologies which were attempted for the fabrication of templates to control magnetic media microstructure. The pros and cons of these approaches are discussed and some preliminary results are presented.

### 9.2. Patterning Trenches into a ‘Segregant’ Film

The template design here comprised of a matrix of patterned segregant ( $\text{SiO}_2$ ), with wells where the underlayer (Ru) is exposed. Figure 9-1 shows a schematic of such a template. The basic idea here is that, when CoCrPt along with  $\text{SiO}_2$  is sputtered onto this, the  $\text{SiO}_2$  should preferentially grow on the  $\text{SiO}_2$  part of the template given enough mobility during sputtering, since such a configuration will minimize the interfacial area between CoCrPt and  $\text{SiO}_2$  and hence minimize the interfacial energy.

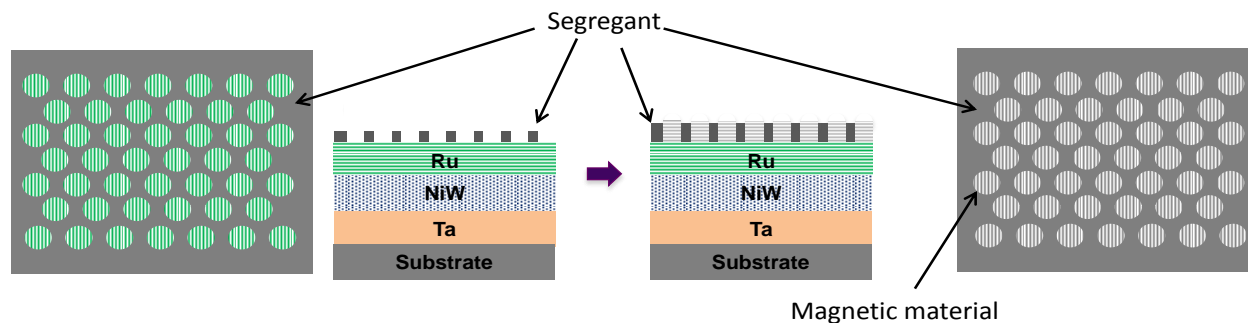


Figure 9-1: Schematic of alternate templated growth approach – I

The initial film stack was first sputtered using the Z400#1 sputtering system at room temperature, and it comprised of layers of Ta, NiW and Ru. The sputtering conditions and thicknesses for each layer are outlined in Table 9-1. Ta is used as an adhesion layer. NiW has a face-centered cubic (FCC) crystal structure, and grows with (111) crystallographic texture. A layer of Ru is subsequently sputtered onto the film stack. Ru has the hexagonal close packed (HCP) crystal structure, and is typically used as the underlayer to grow CoCrPt magnetic media as discussed in chapter 1. A thin SiO<sub>2</sub> (segregant) layer was then sputtered. The mask structure comprising of alternating layers of C (5 nm)/SiN<sub>x</sub> (4 nm)/C (20 nm) was sputtered using sputtering machine #4. PSD1 was then spin-coated onto the film stack, and solvent annealed using toluene to facilitate micro-phase separation. Pattern transfer was then accomplished using RIE to obtain am-C pillars, shown in Figure 9-2(a).

Table 9-1: Summary of sputtering conditions for various thin films

Layer	Machine	Power	Pressure	Rate	Thickness
Ta	Z400#1	100W (RF)	5mT Ar	3.8 nm/min	3 nm
NiW	Z400#1	90W (RF)	5mT Ar	6.3 nm/min	20 nm
Ru	Z400#1	100W (RF)	5mT Ar	4 nm/min	5 nm
SiO <sub>2</sub>	Z400#1	100W (RF)	5mT Ar	3.1 nm/min	5 nm
am-C	#4	150W (DC)	5mT Ar	2.2 nm/min	20/5 nm
SiN <sub>x</sub>	#4	300W (RF)	5mT (3.5 Ar/1.5 N <sub>2</sub> )	3.9 nm/min	4 nm
CoPt-SiO <sub>2</sub>	Z400#1	100W (RF)	2.5mT Ar	3.7 nm/min	15 nm

In order to create the template, we need to create a negative of this pattern. To accomplish this, we used hydrogen-silsesquioxane (HSQ), which is a commonly used negative e-beam resist and a spin-on-glass. The HSQ is dispensed onto the sample by spin-coating. Upon baking, the HSQ molecules cross-link, forming a network structure similar to SiO<sub>2</sub>[86], [87]. The thickness of the HSQ layer is much higher than the height of the fabricated pillars, resulting in a nearly planar surface, as shown by the SEM image in Figure 9-2(b). HSQ has been used for planarization in the semiconductor industry[88], and since it is spin coated from a solution, fills the gaps between the pillars as well. Since the properties of the baked HSQ are similar to SiO<sub>2</sub> it can be etched using a CF<sub>4</sub> plasma in RIE. This is done until the tops of the am-C pillars are exposed, as shown in Figure 9-2(c). Then, using an O<sub>2</sub> plasma which does not etch the HSQ, the C pillars were etched away, and thus a negative of the pattern was created, as seen from the plane-view scanning electron micrograph in Figure 9-2(d). This pattern can then be transferred into the underlying segregant layer using a CF<sub>4</sub> plasma.

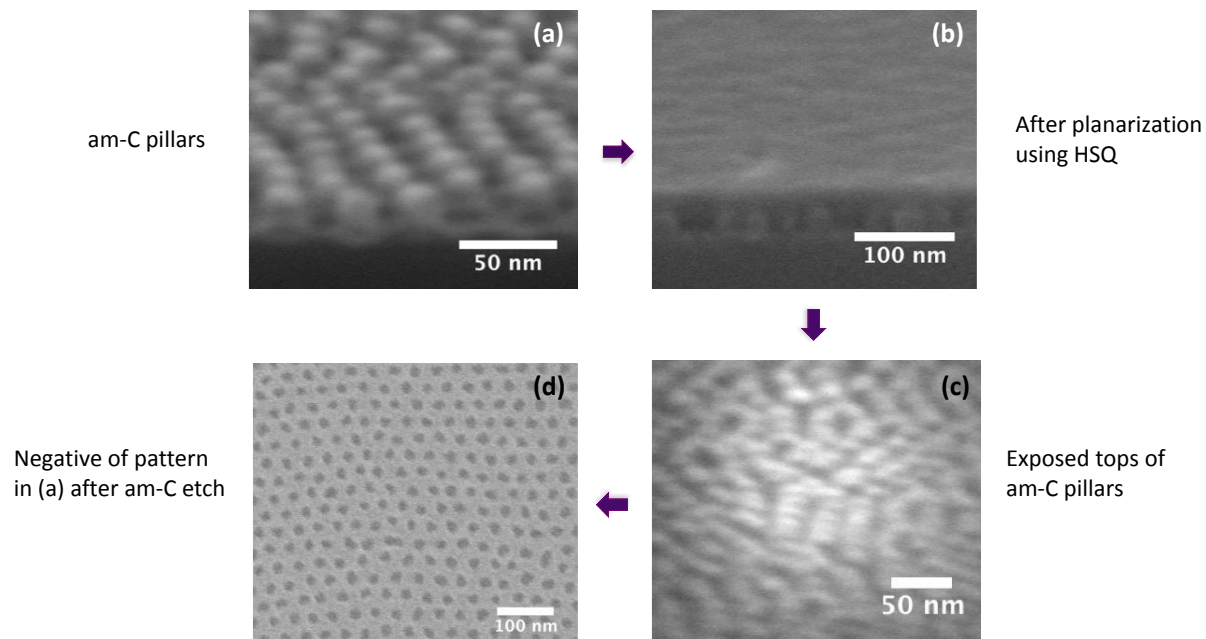


Figure 9-2: SEM micrographs (a) tilt-view image of am-C pillars after pattern transfer (b) after spin-coating HSQ (planarization) (c) etch-back to expose the tops of the am-C pillars and (d) after removal of am-C pillars in RIE

15 nms of CoPt-SiO<sub>2</sub> was then sputtered onto this template using a Co target modified with Pt and SiO<sub>2</sub> chips in the Z400#1 sputtering machine. Figure 9-3 shows the XRD patterns for the underlayer stack and templated media.

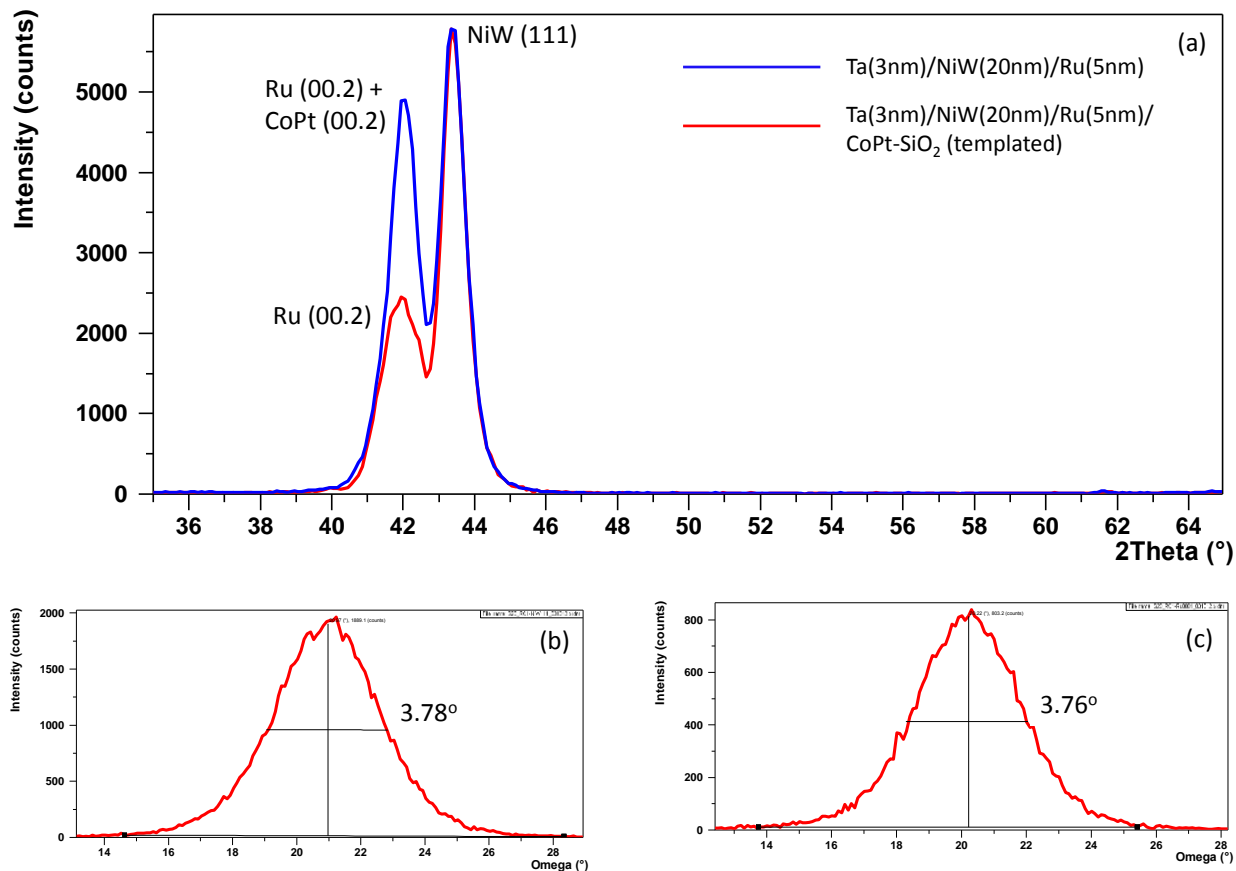


Figure 9-3: (a) Out-of-plane XRD pattern for underlayer stack (red) and templated media (blue); (b) Rocking curve for the Ru (00.2) peak and (c) Rocking curve for the NiW (111) peak

From the out-of-plane XRD pattern of the underlayer stack, we see the FCC (111) peak of the NiW, and the HCP (00.2) peak of the Ru. The purpose of the NiW layer here is to improve the texture of the Ru (00.2). NiW naturally grows with the (111) fiber texture with low rocking angle when sputtered onto Ta (which is amorphous). Further, the lattice mismatch between NiW and Ru in the close-packed plane (shown in Figure 9-4) is only 5.5%, which results in good epitaxial growth of Ru (00.2) on the NiW (111). The rocking curves of the NiW (111) and Ru (00.2) peaks shown in Figure 9-3(b) and (c), show that the distribution in c-axes for both layers are

approximately  $3.8^\circ$ , which is an acceptable value for the underlayer stack for growing magnetic media. When CoPt-SiO<sub>2</sub> is sputtered on the template, there is an increase in the intensity of the peak around  $2\theta = 42^\circ$  in the XRD pattern, which is due to contribution from the CoPt (00.2) peak, indicating that the templated media sample has good texture. It is difficult however, to determine the distribution of the c-axis of the CoPt by doing a rocking curve in this case due to overlap of the XRD peak with the Ru (00.2).

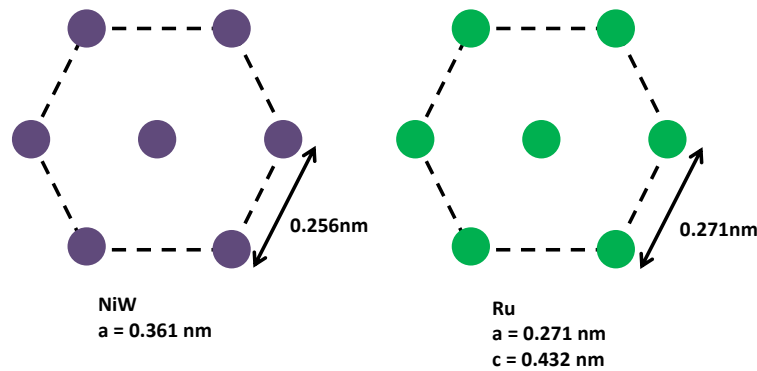


Figure 9-4: Figure depicting the lattice mismatch in the close-packed planes of NiW FCC (111) and Ru HCP (00.2)

Alternating Gradient Field Magnetometry (AGM) was then used to study the magnetic hysteresis behavior. A reference sample with the entire film stack (underlayers + magnetic media), with no block copolymer patterning was also sputtered, in order to compare the effect of the templating process. An overlay of the out-of-plane magnetic hysteresis loops for the templated and un-templated samples is shown in Figure 9-5. From these measurements, properties such as coercivity, remnant magnetization, nucleation field, and the shape of the loop in general gives us insights into the properties of the film. The reference sample has a low coercivity of about 250 Oe,

but the ratio of the remnant magnetization ( $M_r$ ) to saturation magnetization ( $M_s$ ) is 1. Also, as soon as the field reaches the nucleation field ( $H_n$ ), the magnetization drops sharply and switches to the opposite state. This sample has good texture, as indicated by  $M_r/M_s = 1$ , but there is a high degree of exchange coupling. In such a scenario, as soon as a domain with opposite magnetization nucleates, exchange coupling aids its propagation, and the entire film switches nearly at the nucleation field itself. In case of the templated sample however,  $M_r/M_s$  is low, and so is the coercivity. Thus although there was an increase in the (00.2) peak in the XRD pattern of the templated sample, which indicated well-textured CoPt, the magnetic properties show that there is either poor texture, or a high percentage of in-plane oriented grains of CoPt, resulting in a low  $M_r/M_s$  and a low coercivity. The in-plane magnetic hysteresis loops shown in Figure 9-5(b) also support our earlier conclusions. The anisotropy constant  $K_u$  is directly proportional to the saturation field in the in-plane loop. We see that the reference sample has a high saturation field of approximately 10 kOe, supporting our earlier conclusion that it has good (00.2) texture perpendicular to the plane of the film. On the other hand, high in-plane remanence, such as for our templated media sample indicate that a large percentage of the magnetic grains have in-plane orientation. The magnetic properties of the templated specimen are thus unsatisfactory.

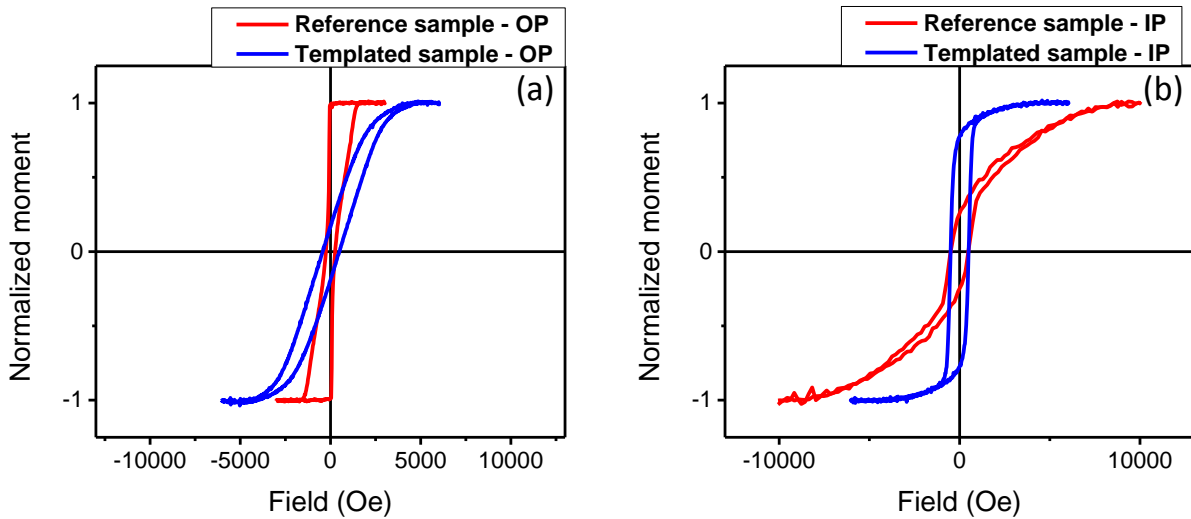


Figure 9-5: (a) Out-of-plane and (b) In-plane magnetic hysteresis loops of templated (blue) and untemplated (red) media samples

Plane-view TEM was then used to observe the microstructure. In the bright field images shown in Figure 9-6, we can observe a hexagonal array of lighter regions indicating the patterning from the block copolymer. The center-to-center spacings between these regions are about 33 nm, which is similar to the block copolymer pitch. Although the magnetic media microstructure is not clear, we observe squiggles of oxide in the microstructure. We can clearly see however, that the templating process we proposed, with the oxide growing on the oxide region of the template, and the magnetic media growing in the wells, doesn't seem to be working. There are a few possible reasons for this: one is that the oxide percentages in the target and in the template might need to be matched. The volume fraction of  $\text{SiO}_2$  in the media seems insufficient. Also, from the Thornton diagram[56], we see that such squiggles of oxide may result from too high a mobility for the sputtered atoms on the sample surface. However, for a template with a pitch of 33 nm, the sputtered  $\text{SiO}_2$  needs to diffuse approximately 10-15 nms if templated growth has to be achieved, and thus we need high mobility. One possible direction to continue is thus to first move to smaller pitch

block copolymers, and to try different sputtering conditions and different oxide volume fractions to see if templated growth is achievable.

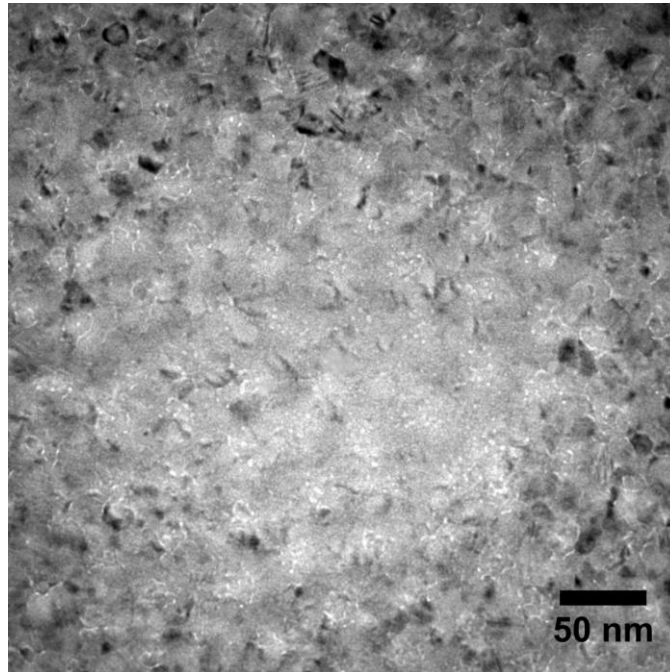


Figure 9-6: TEM micrographs of templated media using the initial approach

A similar approach was attempted with PSD2 (refer Table 4-1), with 20 nm pitch, to lower the surface diffusion length of  $\text{SiO}_2$  and CoPt in the templated growth process. Figure 9-7 shows the plane-view SEM images after pattern transfer to create am-C pillars, and then the pattern reversed using HSQ. At this scale, the process was difficult to reproduce. Variation of bias voltage during etching of 5%, or a few additional seconds of etching yielded different results.

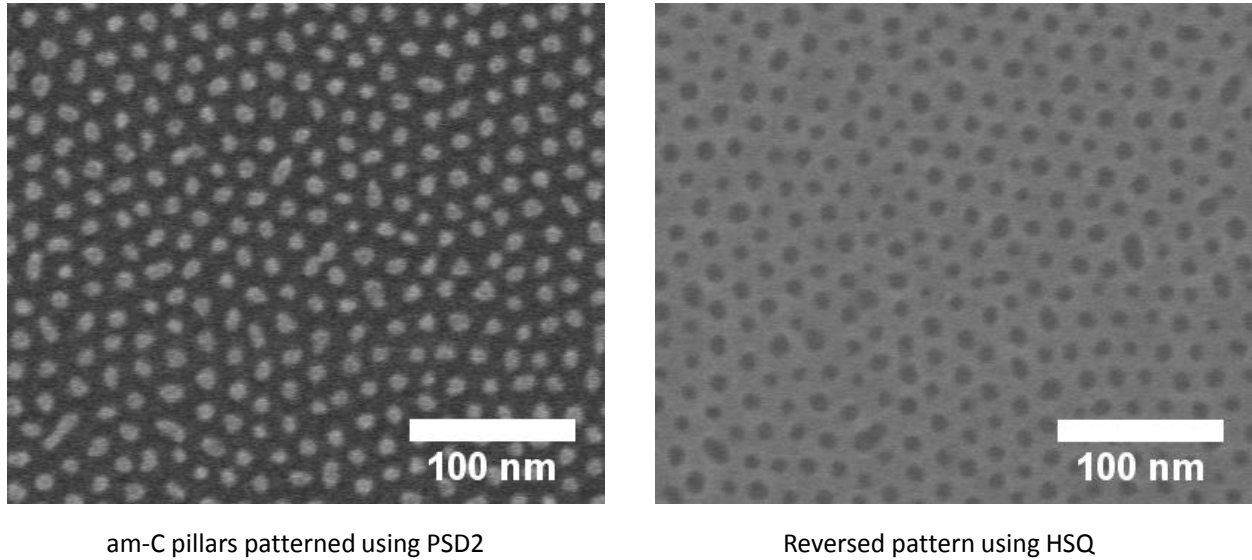


Figure 9-7: Plane-view SEM micrographs of am-C pillars patterned using HSQ, and after pattern reversal using HSQ process

Scalability to sub-20 nm pattern templates was difficult in this approach since the process windows for the etching, pattern reversal etc. were too narrow to enable this in a reproducible fashion. An additional challenge was the control of well volume fraction so that the templated media would have thin, uniform grain boundaries and a high fill-factor. It was thus not conclusive whether this approach would be useful for templating the growth of magnetic media, and a different approach was necessary.

### 9.3. High Aspect Ratio Posts as Templates

In this approach, we attempted to fabricate an array of high aspect ratio pillars/posts on the substrate and looked to achieve decoupled CoCrPt island growth on these pillars, as shown in the schematic below (Figure 9-8).

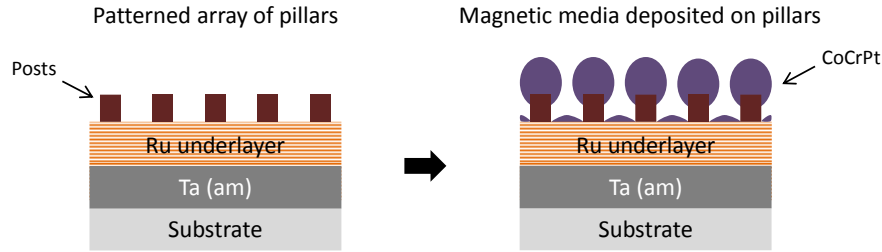


Figure 9-8: Schematic for alternate templated growth approach – II

The choice of material for the posts influence the type of magnetic materials that may be used. For example, the magnetic easy axis in case of CoCrPt alloys is defined by magneto-crystalline anisotropy (easy axis is along the HCP [001]). The posts would thus have to be fabricated with a material that results in (00.2) texture of the sputtered media. The other possibility is to use a non-magnetic material for the posts and use Co/Pd or Co/Ni multilayers, in which case the magnetic easy axis is due to surface anisotropy.

In this project, we worked with CoCrPt as the magnetic material, and we thus have to fabricate high aspect ratio pillars of CoCrPt or Ru, both of which will result in epitaxial growth of subsequently grown CoCrPt. The challenge in the template fabrication thus lies in the pattern transfer into a CoCrPt thin film using ion-milling. Am-C pillars patterned using block copolymer patterns as described earlier were used as the hard mask. The ion-milling process was evaluated systematically starting from a pattern with 33 nm pitch, moving then to 20 nm and subsequently to 17 nm.

The initial film stack consists of Ta(3nm)/Ru(25nm)/CoCrPt(10, 15nm) and 20 nm of C as the hard mask. The SIMS detector in the ion-mill was used to determine the etch rates of the respective materials (Table 5-4). An angle of 22.5° was maintained between the normal to the film plane and

the ion beam. Figure 9-9 shows example plane-view SEM images of am-C posts patterned using PSD1 (33 nm pitch) and after the ion-milling into CoCrPt. After ion-milling, the spatial isolation of the CoCrPt can be inferred by the increase in film coercivity as seen in Figure 9-10(a). This is due to the difference in mechanisms for magnetization reversal in the two samples. While the magnetization in the sheet film switches by domain wall motion, magnetization reversal in the isolated magnetic islands occurs by Stoner-Wohlfarth rotation, which requires a higher field. 40-80 seconds was found to be sufficient to isolate the CoCrPt pillars for the 10 nm case, while a milling time of around 70 seconds was necessary for the 15 nm case. In both cases, after around 90 seconds, the carbon mask is eroded away completely and the coercivity starts to reduce.

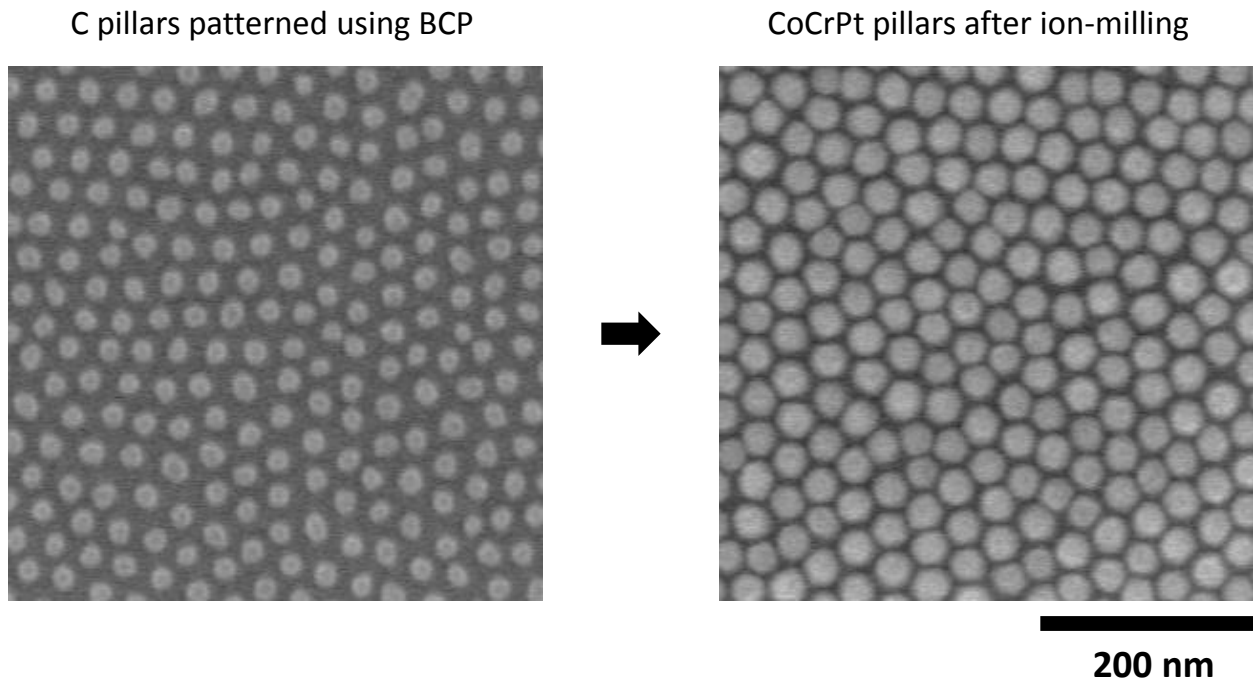


Figure 9-9: Plane-view SEM images of C pillars and after ion milling into CoCrPt

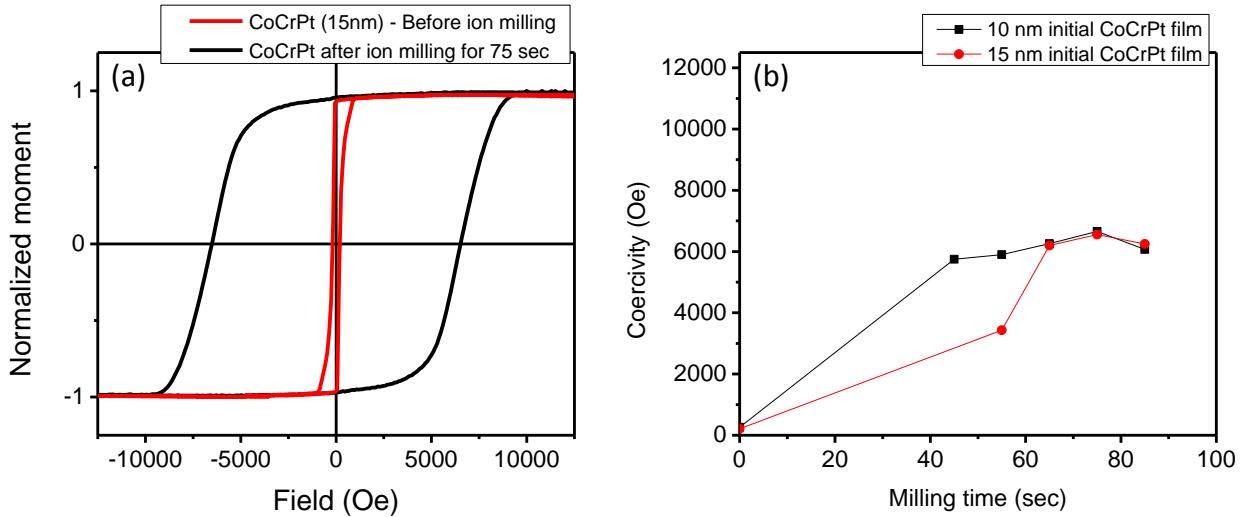


Figure 9-10: (a) M-H loop comparing a 15 nm CoCrPt film before (red) and after (black) patterning (b) Coercivity vs milling time for 10 and 15 nm CoCrPt films

We then moved onto patterning into a 10nm CoCrPt film using PSD2 (~ 20 nm pitch). Figure 9-11 summarizes the ion-milling results characterized using SEM and AGM. The ion-milling angle used here was  $22.5^\circ$ . The highest coercivity in this case is achieved for a milling time of 40 seconds. After 60 seconds, the entire magnetic material has been milled away, and thus a hysteresis loop is not obtained. The line with the negative slope seen in the figure is due to the diamagnetic contribution of the substrate and the sample holder; this is usually corrected for before the hysteresis loops are plotted. The erosion of the carbon hard mask is much faster in the 20 nm pitch case. This is due to the difference in the diameter of the carbon masks prior to milling. As the diameter decreases, an increase in the lateral etching contribution hastens the mask erosion. Also, the increase in coercivity for patterning using this block copolymer pattern (20 nm pitch) is not as dramatic as it was for the earlier case (33nm pitch). It is well known that the ion-milling technique is not ideal for pattern transfer into magnetic materials due to the creation of a damaged surface. As we go to smaller patterns, the fraction of the damaged surface becomes significant, affecting

the maximum coercivity that can be achieved. Reducing the ion-milling angle to  $12.5^\circ$  from  $22.5^\circ$  increased the coercivity from 1.8 kOe to 2.65 kOe, as shown in Figure 9-12.

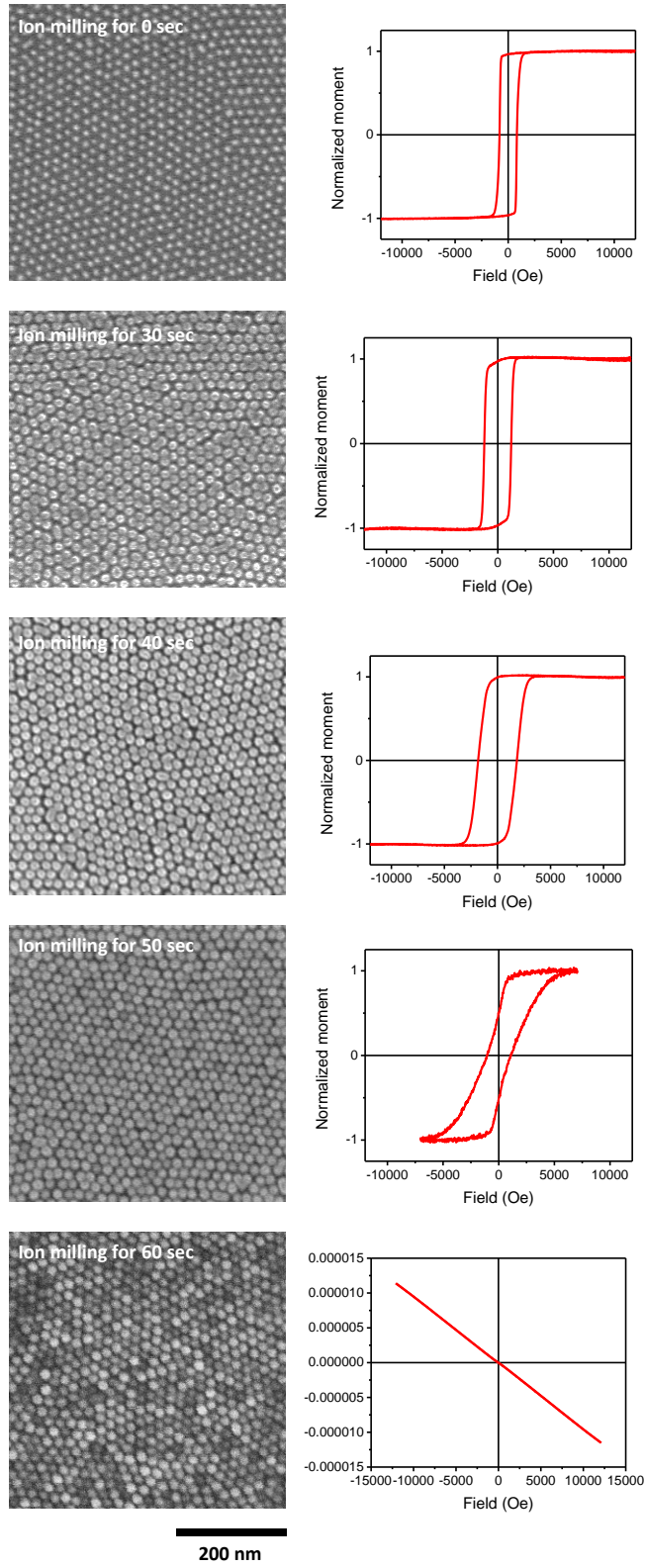


Figure 9-11: SEM and AGM results after patterning into a 10 nm CoCrPt film using PSD2

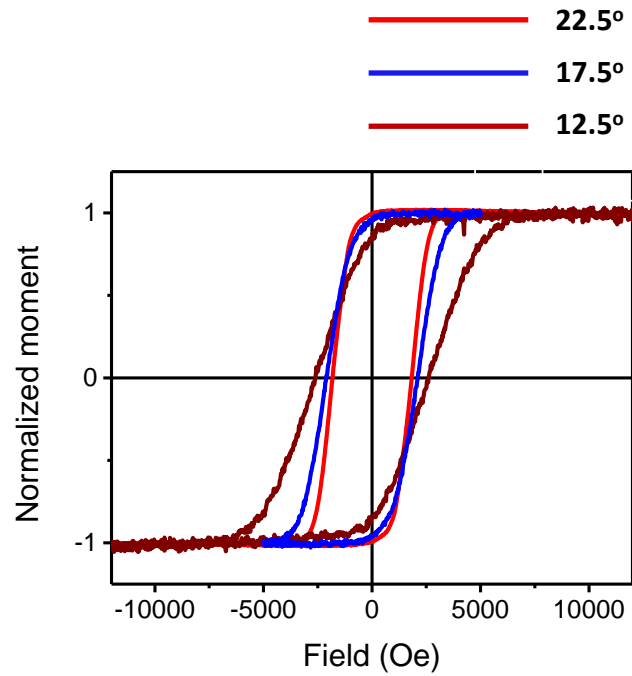


Figure 9-12: Effect of ion-milling angle on the coercivity of the patterned film

Cross-section TEM was used to study the morphology of the patterned CoCrPt pillars obtained using the 12.5° milling angle, and is shown in Figure 9-13.

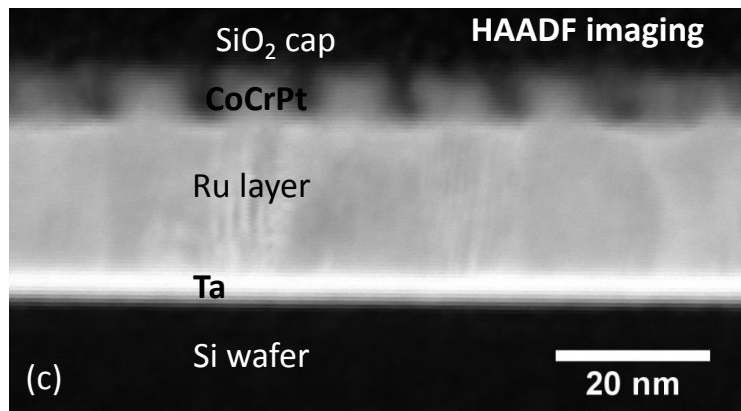
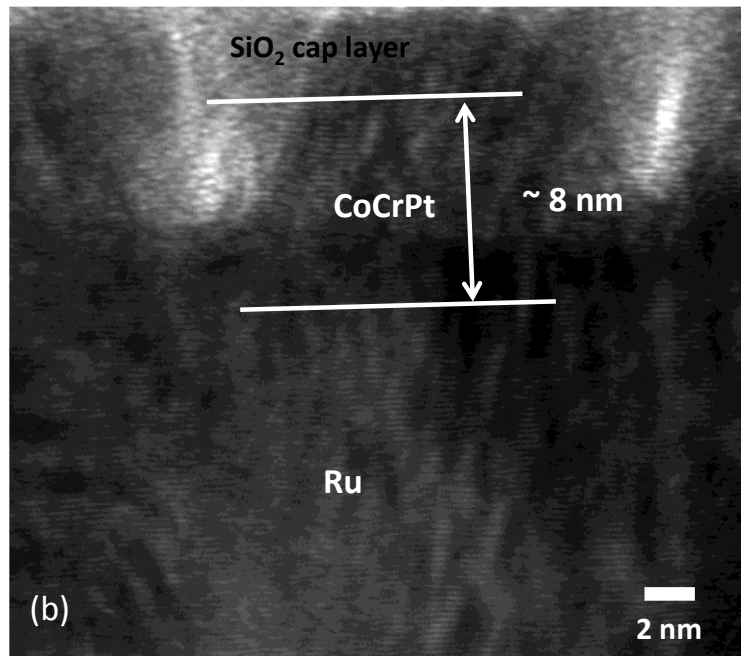
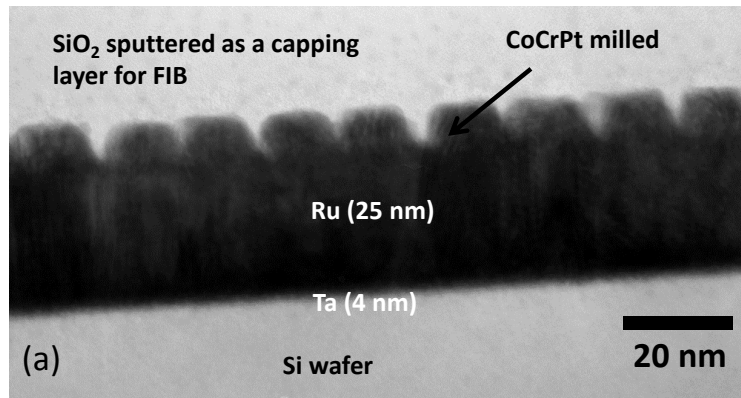


Figure 9-13: (a) Bright field cross-section TEM after ion-milling into 10nm of CoCrPt using PSD2 (b) High-resolution TEM image (c) HAADF image of the patterned pillars

As seen in (a) and (b), the pattern transfer results in nearly vertical side-walls. However, given the close lattice matching between the Ru and the CoCrPt, the boundary between the CoCrPt and the Ru is not discernible. The boundary is clearer in the HAADF-STEM image, where the contrast is due to 'Z'. However, the difference in contrast between the patterned region and the continuous film underneath could also be due to the reduced amount of material in the patterned region. Thus the completion of ion-milling through the CoCrPt layer is understood indirectly using the magnetic properties. It also appears that the carbon mask has eroded completely at this time, which explains why further milling rapidly degrades the magnetic properties. The aspect ratio that was achieved in this case was approximately 3:4 (height:width). As we try to fabricate patterns with smaller pitch, the achievable aspect ratio decreases further; this approach may thus also be difficult to scale down to sub-10nm dimensions. For example, using the same ion-milling conditions (12.5°, 500V, 40mA) for a pattern with 17 nm pitch results in 'domes' rather than 'pillars' as discussed in chapter 6 and as seen below in the cross-section TEM image.

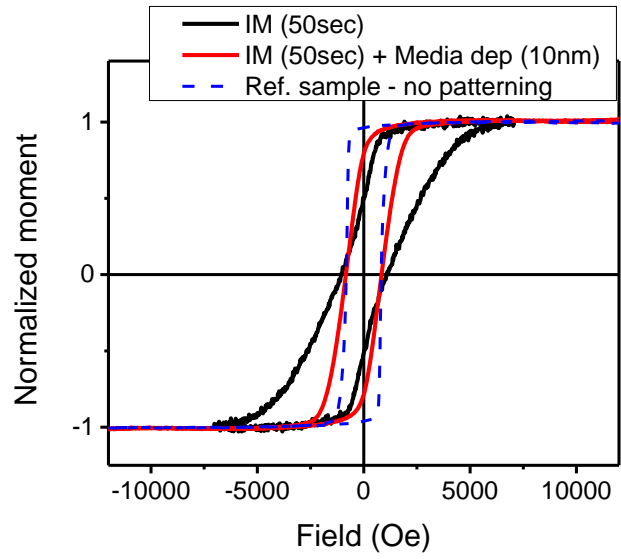
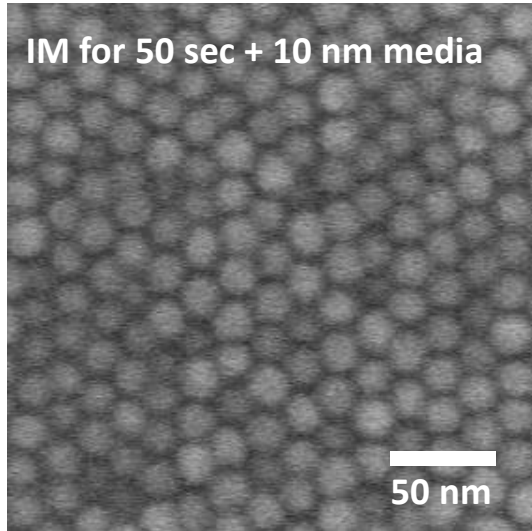
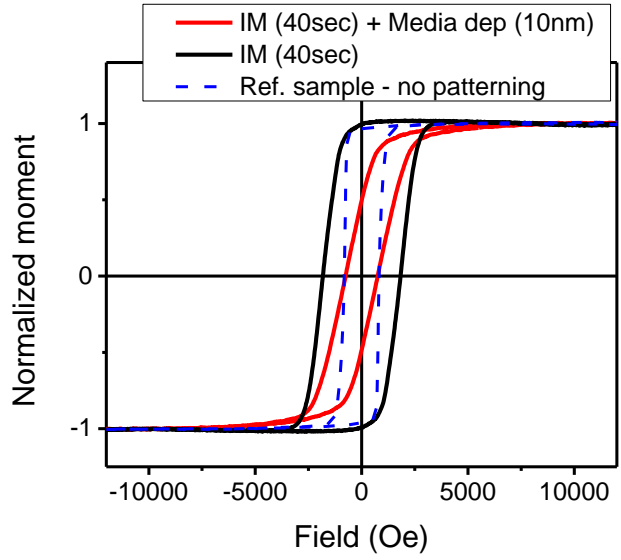
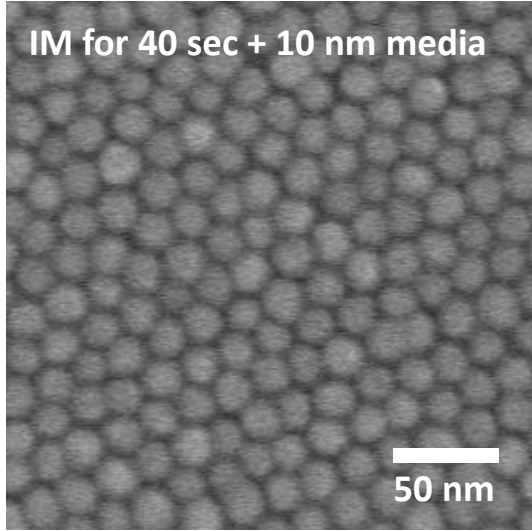


Figure 9-14: SEM images and M-H loops after media deposition on 10 nm tall CoCrPt posts patterned using PSD2

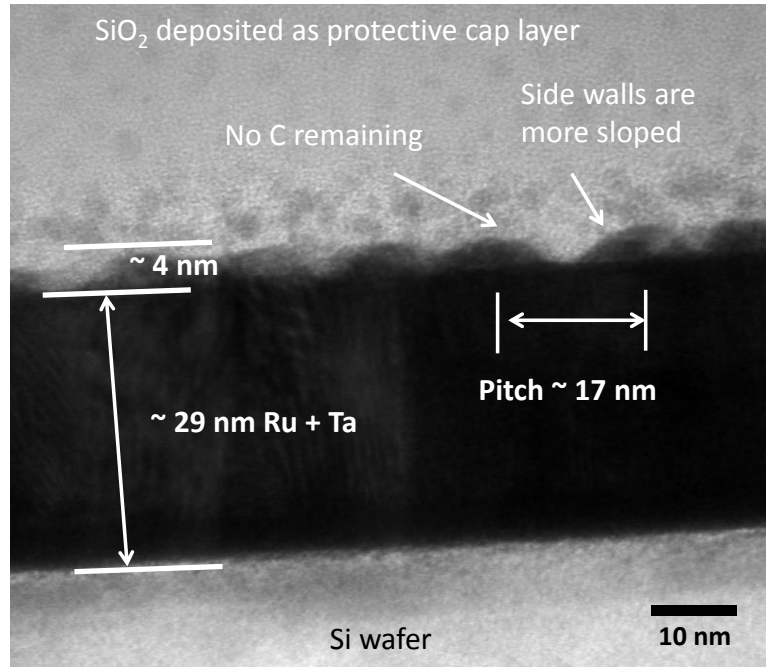


Figure 9-15: Cross-section TEM showing the morphology after pattern transfer into 5 nm of CoCrPt using PSD3

The fabrication of high aspect ratio pillars of CoCrPt is thus quite challenging for patterns with pitch below 20 nm. Figure 9-14 shows the magnetic properties and scanning electron micrographs after media deposition onto 10 nm tall CoCrPt posts patterned using PSD2. Although the SEM images seem to indicate isolated CoCrPt pillars after media deposition, the magnetic properties show a clear reduction in coercivity after the media deposition, indicating poorly textured and exchange coupled magnetic grains. Given that achieving a similar aspect ratio is difficult for smaller pitch, this approach is thus not viable for templated growth using CoCrPt. However, high-aspect ratio pillars can be fabricated in materials such as carbon, silicon, silicon nitride etc. using Reactive Ion Etching, which, as mentioned earlier might be suitable for fabricating isolated pillars using Co/Pt, Co/Ni multilayers etc.

## 9.4. Conclusions

In this chapter, we discussed two alternate approaches for fabricating templates for magnetic media microstructure control. In the first one, trenches exposing the underlayer were patterned into a segregant film. In the second, fabrication of high aspect ratio CoCrPt posts were attempted. In both cases, developing processes for sub-20 nm pitch proved quite challenging, and the effectiveness of the templated media approach could not be verified.

## CHAPTER 10

# Conclusions and Suggestions for Future Work

### 10.1. Summary

With the current magnetic recording technology (PMR) nearing its fundamental limits, better control of magnetic media microstructure is essential to scale the recording density to the maximum possible limit. Two of the key aspects here are the grain size and grain boundary thickness distributions. The microstructure control challenge becomes amplified in Heat Assisted Magnetic Recording (HAMR) due to the high temperature sputtering required to facilitate good  $L1_0$  ordering. There are also fabrication challenges to overcome for Bit Patterned Media, in order to overcome the limitations of the additive and subtractive approaches currently in use.

In this thesis, we've conceptualized and tested an approach for media microstructure control by fabricating a template onto which the media is sputtered. This template consists of an array of pre-patterned sites with a dome-morphology which influences the grain nucleation and growth characteristics of the media sputtered subsequently.

A hexagonal array of carbon (hard-mask) pillars were fabricated by two methods: in the first, the self-assembly of di-block copolymer poly(styrene-b-dimethyl siloxane) with polydimethyl siloxane volume fractions around 17% was used to pattern a hexagonal array of polydimethyl siloxane spheres in a polystyrene matrix. An  $O_2$  plasma in a Reactive Ion Etching system was used

to selectively etch the polystyrene and subsequently the amorphous carbon mask leaving behind an array of carbon pillars. In the second, a combination of nanoimprint lithography and reactive ion etching was used to create a spatially long range ordered array of pillars by our collaborators at Seagate. With these carbon pillars as the hard mask, a dome morphology was patterned into a suitable material in order to fabricate the template.

For the fabrication of current PMR media based on CoPt, we tested three template layers: a CoCrPt alloy with HCP (00.2) texture, Ru with HCP (00.2) texture and Pt with FCC (111) texture. The use of CoCrPt resulted in a template which caused a magnetically soft region in the media sputtered subsequently due to the ion-beam damage caused during the ion milling process. Ru is a suitable template layer in terms of lattice matching with CoPt, but no suitable solution was found for the sputter-etching process to generate a fresh Ru surface prior to media deposition. Pt however, is a material that does not oxidize at room temperature. A template fabricated using Pt, with a thin layer of Ru sputtered prior to media deposition was found to be the best choice for the template layer. A layer of Ru is sputtered onto the Pt template prior to media deposition for two reasons: it enables the correct HCP (00.2) texture for CoPt, and it rectifies some of the beam damage in the Pt template so that the CoPt is being deposited on a less-damaged surface.

Using the Pt-based template, a uniform CoPt-SiO<sub>2</sub> media microstructure with a grain size of 16.2 nm and a grain size distribution of ~ 11% was achieved using a block copolymer with a pitch of 17 nm. We thus see that the grain size is determined by the pitch of the block copolymer pattern, and that by generating a template with a low pitch distribution, magnetic media with low grain size distribution can be fabricated.

Cross-section STEM indicates that the CoPt grows on top of the patterned domes while SiO<sub>2</sub> goes into the trenches. During the sputtering process, when CoPt and SiO<sub>2</sub> species from the target reach the template and impinge on the Ru, the surface mobility of the species is determined by the sputtering conditions and the interactions of the species with the template. While CoPt and Ru have a similar crystal structures with an epitaxial relationship, SiO<sub>2</sub> is immiscible with both CoPt and Ru. SiO<sub>2</sub>-Ru interface is thus higher energy and the SiO<sub>2</sub> will consequentially have a higher surface mobility. The CoPt thus ‘sticks’ on top of the dome while the SiO<sub>2</sub> is pushed to the trenches. The other aspect to take into consideration is the shadowing effect during sputtering. As discussed by Bales and Zangwill in this paper[89], sputtering on substrates with a certain topography under a sputtering condition that causes a high degree of shadowing may cause columnar growth of the film sputtered subsequently. It is likely that a combination of these effects discussed above facilitates the templated growth process.

By using a long-range spatially ordered array of carbon pillars as the hard mask for template fabrication, we can also apply the templated growth technique for the fabrication of bit patterned media. In each case, the mask structure, i.e. the height and width of the carbon pillars has to be optimized in combination with ion-milling to achieve the right dome-morphology for the template, in order to facilitate the required microstructure of the media. A long range array of patterned amorphous carbon pillars were fabricated using nanoimprint lithography at Seagate. After the optimization of the mask structure, templated media with 27 nm pitch and long range positional ordering of the CoPt grains, along with good magnetic properties was achieved.

FePt based HAMR media is typically sputtered at elevated temperatures to enable good L1<sub>0</sub> ordering. In order to evaluate the templated growth approach for HAMR media fabrication, we tested the stability of the dome-morphology in (002) textured Tungsten and Platinum thin films on

heating at 600°C for 30 mins, and found that the dome-morphology flattens out. However, on sputtering an MgO cap at room temperature before raising the temperature, the morphology of the template was retained. Preliminary microstructure results of FePt-SiO<sub>2</sub> on the template shows a clear difference as compared to the un-templated microstructure, but further optimization is necessary to utilize this approach for HAMR media fabrication.

## **10.2. Suggestions for Future Work**

### **a. Perpendicular Magnetic Recording Media**

Current PMR media has an average CoPt grain size of approximately 8 nm. While the templated growth technique described in this thesis is a promising approach for the minimization of grain size and grain boundary thickness distributions, we need to be able to fabricate templates where the center-to-center distance between the domes is sub-10nm. Achieving such feature sizes using self-assembling block copolymers still remains a challenge. The smallest feature sizes achieved here was 12 nm pitch, using a poly (styrene-b-dimethyl siloxane) block copolymer with a molecular weight of 8 kg/mol. The process windows for this block copolymer, such as the thickness variation tolerance and bias variation during pattern transfer was insufficient for us to develop reproducible recipes. Research on new block copolymers with larger values of the Flory-Huggins parameter (enabling phase segregation even at smaller degree of polymerizations required for smaller feature sizes, see Section 4.2), and new techniques for pattern transfer for a wider variety of block copolymers are both necessary for achieving sub-10 nm features. Other self-assembling materials such as nanoparticles can also be explored for this purpose.

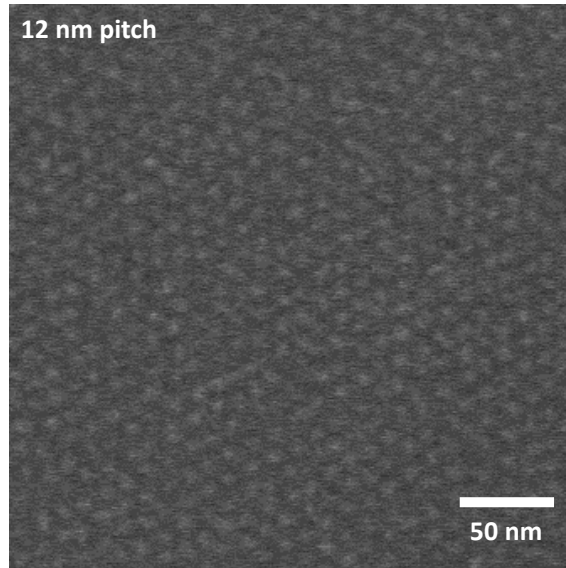


Figure 10-1: SEM micrograph showing self-assembled block copolymer pattern with 12 nm pitch

While the fabrication of sub-10 nm self-assembled patterns is challenging, the fabrication of the template and the guided magnetic media microstructure should be scaleable. One of the advantages of the template here is that the ion-milling requirements are not stringent, since a dome-morphology with a relatively low aspect ratio is sufficient. Further, during the CoPt-SiO<sub>2</sub> sputtering process, if the feature size is less, the SiO<sub>2</sub> needs to diffuse a shorter distance to reach the trenches.

#### **b. Bit Patterned Media**

In the case of Bit Patterned Media using templated growth, the two key things requiring further improvement are the crystallographic texture of the magnetic media, and the uniformity of the grain boundaries. We discussed in chapter 7 that the un-templated region had better crystallographic texture than the templated region. This may be due to the sputtering of the Ru underlayer and the media on a curved surface. A study impact of this surface curvature on the

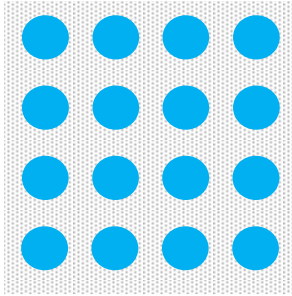
texture of the subsequently sputtered materials will be of great use. The variation in the grain boundary thickness in the templated media discussed in chapter 7 is likely due to the variation in dome-morphology patterned into the template. Better control of the various etching processes for the mask structure fabrication and ion-milling needs to be developed to improve this aspect.

**c. Heat Assisted Magnetic Recording Media (HAMR)**

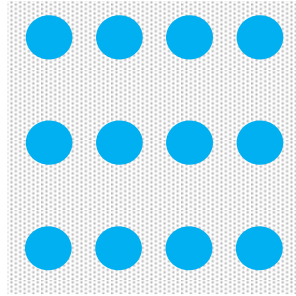
In order to establish whether the templated growth technique can facilitate uniform HAMR media microstructures, further optimization of the segregant type and segregant volume fraction, apart from the sputtering conditions is necessary. Further, since the microstructure scaling requirements of Heat Assisted Magnetic Recording media are similar to those of current perpendicular magnetic media, work regarding the fabrication of sub-10 nm self-assembled nanostructures will be applicable here as well.

**d. Exploring Different Material Combinations and Nanostructures**

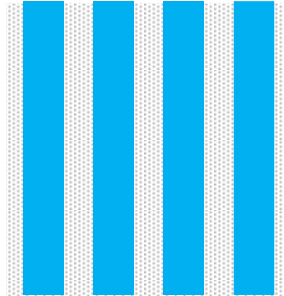
The templated growth approach could be explored for various other combinations of materials, exploiting differences in surface mobilities between the sputtered species on the template layer. Further, in combination with electron beam lithography to pattern different nanostructures as shown in Figure 10-2, the applicability of templated growth for the fabrication of square lattices, aperiodic structures and nanowires could be explored.



Square Lattice



Aperiodic Structures



Nanowires

Figure 10-2: Examples of different nanostructures to be explored using templated growth

## References

- [1] “What is big data?” [Online]. Available: <http://www-01.ibm.com/software/data/bigdata/what-is-big-data.html>.
- [2] T. Rausch, E. Gage, and J. Dykes, “Heat Assisted Magnetic Recording,” in *Ultrafast Magnetism I*, 2015, pp. 200–202.
- [3] S. Z. Wu, “Magnetic Recording,” in *IEEE Magnetism Summer School*, 2013.
- [4] B. M. H. Kryder, E. C. Gage, T. W. McDaniel, W. A. Challener, R. E. Rottmayer, G. Ju, Y. Hsia, and M. F. Erden, “Heat Assisted Magnetic Recording,” *Proc. IEEE*, vol. 96, no. 11, pp. 1810–1835, 2008.
- [5] J.-G. Z. J.-G. Zhu, X. Z. X. Zhu, and Y. T. Y. Tang, “Microwave Assisted Magnetic Recording,” *IEEE Trans. Magn.*, vol. 44, no. 1, pp. 125–131, 2008.
- [6] B. D. Terris, “Fabrication challenges for patterned recording media,” *J. Magn. Magn. Mater.*, vol. 321, no. 6, pp. 512–517, Mar. 2009.
- [7] HGST Research, “HGST Research.” [Online]. Available: <http://www.hitachigst.com/hdd/research/storage/pm/index.html>.
- [8] J.-G. Zhu, V. Sokalski, Y. Wang, and D. E. Laughlin, “Noise Mechanisms in Small Grain Size Perpendicular Thin Film Media,” *IEEE Trans. Magn.*, vol. 47, no. 1, pp. 74–80, Jan. 2011.
- [9] M. H. Kryder and R. W. Gustafson, “High-density perpendicular recording—advances, issues, and extensibility,” *J. Magn. Magn. Mater.*, vol. 287, pp. 449–458, Feb. 2005.
- [10] S. Iwasaki and K. Ouchi, “Co-Cr recording films with perpendicular magnetic anisotropy,” *IEEE Trans. Magn.*, vol. M, no. MAG-14, pp. 849–851, 1978.
- [11] S. N. Piramanayagam, “Perpendicular recording media for hard disk drives,” *J. Appl. Phys.*, vol. 102, no. 1, p. 011301, 2007.

- [12] T. Shimatsu, H. Sato, T. Oikawa, Y. Inaba, O. Kitakami, S. Okamoto, H. Aoi, H. Muraoka, and Y. Nakamura, "High Perpendicular Magnetic Anisotropy of CoPtCr/Ru Films for Granular-Type Perpendicular Media," *IEEE Trans. Magn.*, vol. 40, no. 4, pp. 2483–2485, Jul. 2004.
- [13] S. Oikawa, a. Takeo, T. Hikosaka, and Y. Tanaka, "High performance CoPtCrO single layered perpendicular media with no recording demagnetization," *IEEE Trans. Magn.*, vol. 36, no. 5, pp. 2393–2395, 2000.
- [14] N. Inaba and M. Futamoto, "Effects of Pt and Ta addition on compositional microstructure of CoCr-alloy thin film media," *J. Appl. Phys.*, vol. 87, no. 9, p. 6863, 2000.
- [15] T. Oikawa, M. Nakamura, H. Uwazumi, T. Shimatsu, H. Muraoka, and Y. Nakamura, "Microstructure and magnetic properties of CoPtCr-SiO/sub 2/ perpendicular recording media," *IEEE Trans. Magn.*, vol. 38, no. 5, pp. 1976–1978, Sep. 2002.
- [16] V. Sokalski, D. E. Laughlin, and J.-G. Zhu, "Experimental modeling of intergranular exchange coupling for perpendicular thin film media," *Appl. Phys. Lett.*, vol. 95, no. 10, p. 102507, 2009.
- [17] H. Muraoka, Y. Sonobe, K. Miura, a. M. Goodman, and Y. Nakamura, "Analysis on magnetization transition of CGC perpendicular media," *IEEE Trans. Magn.*, vol. 38, no. 4, pp. 1632–1636, Jul. 2002.
- [18] Y. Sonobe, D. Weller, Y. Ikeda, K. Takano, M. E. Schabes, G. Zeltzer, H. Do, B. K. Yen, and M. E. Best, "Coupled granular/continuous medium for thermally stable perpendicular magnetic recording," *J. Magn. Magn. Mater.*, vol. 235, no. 1–3, pp. 424–428, Oct. 2001.
- [19] D. Suess, T. Schrefl, S. Fähler, M. Kirschner, G. Hrkac, F. Dorfbauer, and J. Fidler, "Exchange spring media for perpendicular recording," *Appl. Phys. Lett.*, vol. 87, pp. 67–69, 2005.
- [20] J. G. Zhu and Y. Wang, "SNR enhancement in segmented perpendicular media," *IEEE Trans. Magn.*, vol. 47, no. 10, pp. 4066–4072, 2011.
- [21] H. N. Bertram, *Theory of Magnetic Recording*. Cambridge University Press, 1994.
- [22] D. Weller and a. Moser, "Thermal effect limits in ultrahigh-density magnetic recording," *IEEE Trans. Magn.*, vol. 35, no. 6, pp. 4423–4439, 1999.
- [23] E. C. Stoner and E. P. Wohlfarth, "A mechanism of magnetic hysteresis in heteresis in heterogeneous alloys," *Phil. Trans. Roy.Soc.*, vol. A-240, no. 4, pp. 599–642, 1948.
- [24] D. Guarisco and H. Nguy, "High linear density in perpendicular recording," *J. Appl. Phys.*, vol. 93, no. 10, p. 6745, 2003.

- [25] D. Weller, O. Mosendz, G. Parker, S. Pisana, and T. S. Santos, "10 FePtX-Y media for heat-assisted magnetic recording," *Phys. Status Solidi*, vol. 210, no. 7, pp. 1245–1260, Jul. 2013.
- [26] X. Yang, S. Xiao, W. Wu, Y. Xu, K. Mountfield, R. Rottmayer, K. Lee, D. Kuo, and D. Weller, "Challenges in 1 Terabit/in.<sup>2</sup> dot patterning using electron beam lithography for bit-patterned media," *J. Vac. Sci. Technol. B Microelectron. Nanom. Struct.*, vol. 25, no. 6, p. 2202, 2007.
- [27] B. D. Terris and T. Thomson, "Nanofabricated and self-assembled magnetic structures as data storage media," *J. Phys. D. Appl. Phys.*, vol. 38, no. 12, pp. R199–R222, 2005.
- [28] X. Yang, Y. Xu, C. Seiler, L. Wan, and S. Xiao, "Toward 1 Tbit/in.<sup>2</sup> nanoimprint lithography for magnetic bit-patterned media: Opportunities and challenges," *J. Vac. Sci. Technol. B Microelectron. Nanom. Struct.*, vol. 26, no. 6, p. 2604, 2008.
- [29] X. Yang, S. Xiao, W. Wu, Y. Xu, K. Mountfield, R. Rottmayer, K. Lee, D. Kuo, and D. Weller, "Challenges in 1 Terabit/in.<sup>2</sup> dot patterning using electron beam lithography for bit-patterned media," *J. Vac. Sci. Technol. B Microelectron. Nanom. Struct.*, vol. 25, no. 6, p. 2202, 2007.
- [30] B. D. Terris, T. Thomson, and G. Hu, "Patterned media for future magnetic data storage," *Microsyst. Technol.*, vol. 13, no. 2, pp. 189–196, 2007.
- [31] E. a. Dobisz, Z. Z. Bandić, T. W. Wu, and T. Albrecht, "Patterned media: Nanofabrication challenges of future disk drives," *Proc. IEEE*, vol. 96, no. 11, pp. 1836–1846, 2008.
- [32] M. T. Moneck and J. Zhu, "Advanced Pattern Generation and Etching Techniques for Bit-Patterned Media," in *Dekker Encyclopedia of Nanoscience and Nanotechnology*, Second ed., 2013, pp. 1–23.
- [33] G. Zangari and D. N. Lambeth, "Porous Aluminum Oxide Templates For Nanometer-sized Cobalt Arrays - Magnetics, IEEE Transactions on," *IEEE Trans. Magn.*, vol. 3, no. 5, pp. 3010–3012, 1997.
- [34] R. M. Metzger, V. V. Konovalov, G. Zangari, M. Benakli, and W. D. Doyle, "Magnetic nanowires in hexagonally ordered pores of alumina," *IEEE Trans. Magn.*, vol. 36, no. 1, pp. 30–35, 2000.
- [35] J. M. García, a. Asenjo, J. Velázquez, D. García, M. Vázquez, P. Aranda, and E. Ruiz-Hitzky, "Magnetic behavior of an array of cobalt nanowires," *J. Appl. Phys.*, vol. 85, no. 8, p. 5480, 1999.
- [36] S. Sun, M. C.B., D. Weller, L. Folks, and A. Moser, "Monodisperse FePt Nanoparticles and Ferromagnetic FePt Nanocrystal Superlattices," *Science (80-. )*, vol. 287, no. 5460, pp. 1989–1992, Mar. 2000.

- [37] T. Wen, R. A. Booth, and S. A. Majetich, "Ten-nanometer dense hole arrays generated by nanoparticle lithography.," *Nano Lett.*, vol. 12, no. 11, pp. 5873–8, Nov. 2012.
- [38] S. Park, D. H. Lee, J. Xu, B. Kim, S. W. Hong, U. Jeong, T. Xu, and T. P. Russell, "Macroscoping 10 Terabit-Per-Square-Inch Arrays from Block Copolymers with Lateral Order," *Science (80-. )*, vol. 323, no. February, pp. 1030–1033, 2009.
- [39] S. Krishnamoorthy, C. Hinderling, and H. Heinzelmann, "Nanoscale patterning with block copolymers," *Mater. Today*, vol. 9, no. 9, pp. 40–47, 2006.
- [40] Y. S. Jung and C. a Ross, "Orientation-controlled self-assembled nanolithography using a polystyrene-polydimethylsiloxane block copolymer.," *Nano Lett.*, vol. 7, no. 7, pp. 2046–50, Jul. 2007.
- [41] M. P. Stoykovich and P. F. Nealey, "Block copolymers and conventional lithography," *Mater. Today*, vol. 9, no. 9, pp. 20–29, 2006.
- [42] F. S. Bates and G. H. Fredrickson, "Block Copolymers—Designer Soft Materials," *Phys. Today*, vol. 52, no. 2, p. 32, 1999.
- [43] S. B. Darling, "Directing the self-assembly of block copolymers," *Prog. Polym. Sci.*, vol. 32, no. 10, pp. 1152–1204, Oct. 2007.
- [44] T. R. Albrecht, D. Bedau, E. Dobisz, H. Gao, M. Grobis, O. Hellwig, D. Kercher, J. Lille, E. Marinero, K. Patel, R. Ruiz, M. E. Schabes, L. Wan, and D. Weller, "Bit Patterned Media at 1 Tdot / sq. in. and Beyond," *IEEE Trans. Magn.*, vol. 49, no. 2, pp. 773–778, 2013.
- [45] O. Hellwig, J. K. Bosworth, E. Dobisz, D. Kercher, T. Hauet, G. Zeltzer, J. D. Risner-Jamtgaard, D. Yaney, and R. Ruiz, "Bit patterned media based on block copolymer directed assembly with narrow magnetic switching field distribution," *Appl. Phys. Lett.*, vol. 96, no. 5, p. 052511, 2010.
- [46] O. Hellwig, a. Moser, E. Dobisz, Z. Z. Bandic, H. Yang, D. S. Kercher, J. D. Risner-Jamtgaard, D. Yaney, and E. E. Fullerton, "Suppression of magnetic trench material in bit patterned media fabricated by blanket deposition onto prepatterned substrates," *Appl. Phys. Lett.*, vol. 93, no. 19, p. 192501, 2008.
- [47] J. K. W. Yang, Y. Chen, T. Huang, H. Duan, N. Thiyagarajah, H. K. Hui, S. H. Leong, and V. Ng, "Fabrication and characterization of bit-patterned media beyond 1.5 Tbit/in(2).," *Nanotechnology*, vol. 22, no. 38, p. 385301, 2011.
- [48] O. Hellwig, T. Hauet, T. Thomson, E. Dobisz, J. D. Risner-Jamtgaard, D. Yaney, B. D. Terris, and E. E. Fullerton, "Coercivity tuning in Co/Pd multilayer based bit patterned media," *Appl. Phys. Lett.*, vol. 95, no. 23, pp. 2–4, 2009.

- [49] J. M. Shaw, W. H. Rippard, S. E. Russek, T. Reith, and C. M. Falco, "Origins of switching field distributions in perpendicular magnetic nanodot arrays," *J. Appl. Phys.*, vol. 101, no. 2, pp. 1–5, 2007.
- [50] T. Thomson, G. Hu, and B. D. Terris, "Intrinsic distribution of magnetic anisotropy in thin films probed by patterned nanostructures," *Phys. Rev. Lett.*, vol. 96, no. 25, pp. 1–4, 2006.
- [51] H. Wang, M. T. Rahman, H. Zhao, Y. Isowaki, Y. Kamata, A. Kikitsu, and J.-P. Wang, "Fabrication of FePt type exchange coupled composite bit patterned media by block copolymer lithography," *J. Appl. Phys.*, vol. 109, no. 7, p. 07B754, 2011.
- [52] K. Naito, H. Hieda, M. Sakurai, Y. Kamata, and K. Asakawa, "2.5-Inch Disk Patterned Media Prepared By an Artificially Assisted Self-Assembling Method," *IEEE Trans. Magn.*, vol. 38, no. 5, pp. 1949–1951, Sep. 2002.
- [53] M. T. Moneck and J. Zhu, "Advanced Pattern Generation and Etching Techniques for Bit-Patterned Media," in *Dekker Encyclopedia of Nanoscience and Nanotechnology*, Second Edi., 2013.
- [54] J. Z. Shi, S. N. Piramanayagam, C. S. Mah, H. B. Zhao, J. M. Zhao, Y. S. Kay, and C. K. Pock, "Influence of dual-Ru intermediate layers on magnetic properties and recording performance of CoCrPt–SiO<sub>2</sub> perpendicular recording media," *Appl. Phys. Lett.*, vol. 87, no. 22, p. 222503, 2005.
- [55] S. H. Park, S. O. Kim, T. D. Lee, H. S. Oh, Y. S. Kim, N. Y. Park, and D. H. Hong, "Effect of top Ru deposition pressure on magnetic and microstructural properties of CoCrPt–SiO<sub>2</sub> media in two-step Ru layer," *J. Appl. Phys.*, vol. 99, no. 8, p. 08E701, 2006.
- [56] J. A. Thornton, "High rate thick film growth," *Annu. Rev. Mater. Sci.*, vol. 7, pp. 239–260, 1977.
- [57] R. Messier, "Revised structure zone model for thin film physical structure," *J. Vac. Sci. Technol. A Vacuum, Surfaces, Film.*, vol. 2, no. 2, pp. 500–503, 1984.
- [58] T. Wang, V. Mehta, Y. Ikeda, H. Do, K. Takano, S. Florez, B. D. Terris, B. Wu, C. Graves, M. Shu, R. Rick, A. Scherz, J. Stöhr, and O. Hellwig, "Magnetic design evolution in perpendicular magnetic recording media as revealed by resonant small angle x-ray scattering," *Appl. Phys. Lett.*, vol. 103, no. 11, p. 112403, 2013.
- [59] J. Goldstein, D. E. Newbury, D. C. Joy, C. E. Lyman, P. Echlin, E. Lifshin, L. Sawyer, and J. R. Michael, *Scanning Electron Microscopy and X-Ray Microanalysis*, Third Edit. 2003.
- [60] M. De Graef, *Introduction to conventional transmission electron microscopy*. Cambridge University Press, 2003.

- [61] D. . Williams and C. . Carter, *Transmission Electron Microscopy: A Textbook for Materials Science*, 2nd Editio. New York: Springer, 2009.
- [62] B. D. Cullity and S. . Stock, *Elements of X-Ray Diffraction*, Third Edit. Prentice Hall, 2001.
- [63] B. D. Cullity and C. D. Graham, *Introduction to magnetic materials*, Second. Wiley, 2009.
- [64] M. Li and C. K. Ober, “Block copolymer patterns and templates,” *Mater. Today*, vol. 9, no. 9, pp. 30–39, 2006.
- [65] X. Gu, I. Gunkel, and T. P. Russell, “Pattern transfer using block copolymers Pattern transfer using block copolymers,” *Philos. Trans. R. Soc. A*, vol. 371, no. 20120306, 2013.
- [66] R. a. Segalman, “Patterning with block copolymer thin films,” *Mater. Sci. Eng. R Reports*, vol. 48, no. 6, pp. 191–226, Feb. 2005.
- [67] J. N. L. Albert and T. H. Epps III, “Self-assembly of block copolymer thin films,” *Mater. Today*, vol. 13, no. 6, pp. 24–33, Jun. 2010.
- [68] I. W. Hamley, “Ordering in thin films of block copolymers: Fundamentals to potential applications,” *Prog. Polym. Sci.*, vol. 34, no. 11, pp. 1161–1210, Nov. 2009.
- [69] G. R. Strobl, *The physics of polymers: concepts for understanding their structures and behavior*. Springer, 2007.
- [70] F. S. Bates and G. H. Fredrickson, “Block copolymer thermodynamics: theory and experiment.,” *Annu. Rev. Phys. Chem.*, vol. 41, pp. 525–57, Jan. 1990.
- [71] M. W. Matsen and F. S. Bates, “Unifying Weak- and Strong-Segregation Block Copolymer Theories,” *Macromolecules*, vol. 29, no. 4, pp. 1091–1098, Jan. 1996.
- [72] C. R. Iacovella, “softmatter: Phase Diagram,” *Materials Digital Library Pathway*, 2006. [Online]. Available: [http://matdl.org/matdlwiki/index.php/softmatter:Phase\\_Diagram](http://matdl.org/matdlwiki/index.php/softmatter:Phase_Diagram).
- [73] T. Nose, “Coexistence curves of polystyrene/ poly(dimethylsiloxane) blends,” *Polymer (Guildf)*, vol. 36, no. 11, pp. 2243–2248, 1995.
- [74] T. P. Russell, R. P. Hjelm, and P. A. Seeger, “Temperature Dependence of the Interaction Parameter of Polystyrene and Poly (methyl methacrylate),” *Macromolecules*, vol. 23, pp. 890–893, 1990.
- [75] H. B. Eitouni, N. P. Balsara, J. A. Pople, and M. A. Hempenius, “Thermodynamic Interactions in Organometallic Block Copolymers :,” *Macromolecules*, vol. 35, pp. 7765–7772, 2002.

- [76] C. a. Ross, Y. S. Jung, V. P. Chuang, F. Ilievski, J. K. W. Yang, I. Bitá, E. L. Thomas, H. I. Smith, K. K. Berggren, G. J. Vancso, and J. Y. Cheng, "Si-containing block copolymers for self-assembled nanolithography," *J. Vac. Sci. Technol. B Microelectron. Nanom. Struct.*, vol. 26, no. 6, p. 2489, 2008.
- [77] M. J. Madou, *Fundamentals of Microfabrication and Nanotechnology*, Third Edit. 2011.
- [78] J. Zhang, X. Yu, P. Yang, J. Peng, C. Luo, W. Huang, and Y. Han, "Microphase Separation of Block Copolymer Thin Films," *Macromol. Rapid Commun.*, vol. 31, pp. 591–608, 2010.
- [79] C. Sinturel, M. Vayer, M. Morris, and M. a. Hillmyer, "Solvent Vapor Annealing of Block Polymer Thin Films," *Macromolecules*, vol. 46, no. 14, pp. 5399–5415, Jul. 2013.
- [80] K. W. Gotrik, A. F. Hannon, J. G. Son, B. Keller, A. Alexander-Katz, and C. a. Ross, "Morphology control in block copolymer films using mixed solvent vapors," *ACS Nano*, vol. 6, no. 9, pp. 8052–8059, 2012.
- [81] J. G. Son, A. F. Hannon, K. W. Gotrik, A. Alexander-Katz, and C. A. Ross, "Hierarchical nanostructures by sequential self-assembly of styrene-dimethylsiloxane block copolymers of different periods.," *Adv. Mater.*, vol. 23, no. 5, pp. 634–9, Feb. 2011.
- [82] J. Brandrup, E. H. Immergut, E. A. Grulke, A. Abe, and D. R. Bloch, *Polymer Handbook*, 4th ed. John Wiley & Sons, 2005.
- [83] S. A. Campbell, *Fabrication Engineering at the Micro and Nano scale*, Fourth Edi. 2012.
- [84] "FactSage." [Online]. Available: <http://www.factsage.com/>.
- [85] B. M. Lairson, M. R. Visokay, R. Sinclair, S. Hagstrom, and B. M. Clemens, "Epitaxial Pt(001), Pt(110), and Pt(111) films on MgO(001), MgO(110), MgO(111), and Al<sub>2</sub>O<sub>3</sub>(0001)," *Appl. Phys. Lett.*, vol. 61, no. 12, p. 1390, 1992.
- [86] S. Choi, M. J. Word, V. Kumar, and I. Adesida, "Comparative study of thermally cured and electron-beam-exposed hydrogen silsesquioxane resists," *J. Vac. Sci. Technol. B Microelectron. Nanom. Struct.*, vol. 26, no. 5, p. 1654, 2008.
- [87] C.-C. Yang and W.-C. Chen, "The structures and properties of hydrogen silsesquioxane (HSQ) films produced by thermal curing," *J. Mater. Chem.*, vol. 12, no. 4, pp. 1138–1141, Mar. 2002.
- [88] K. Nakamatsu, M. Okada, and S. Matsui, "Fabrication of High-Aspect Si Structures by Deep Reactive Ion Etching Using Hydrogen Silsesquioxane Masks Replicated by Room Temperature Nanoimprinting," *Jpn. J. Appl. Phys.*, vol. 47, no. 11, pp. 8619–8621, Nov. 2008.

- [89] G. Bales and A. Zangwill, "Growth Dynamics of Sputter Deposition," *Phys. Rev. Lett.*, vol. 22, no. 4, p. 350, 1989.